UNIVERSITÀ DEGLI STUDI DI PADOVA

Dipartimento di Fisica e Astronomia "Galileo Galilei"

Master Degree in Physics

Final Dissertation

Iron oxide-based nanostructured films for water splitting

Thesis supervisor

Prof. Chiara Maurizio

Candidate

Pietro Tasso

Academic Year 2022/2023

Contents

Abstract

Meeting the escalating energy demands of the 21st century requires sustainable solutions, urging a shift from finite fossil fuels to scalable and renewable sources. Solar energy, a promising contender, demands efficient storage methods due to its intermittent nature. To address this issue, ongoing research is focused on converting sunlight into chemical energy, specifically hydrogen production through water splitting — the reduction of water to H_2 and its oxidation to O_2. The study presented in this thesis falls within the research scope of photoelectrochemical water splitting, where the reaction is assisted by the application of an external potential and illumination from a light source simulating sunlight. It particularly focuses on the solid-state photoanode where the oxidation semi-reaction occurs, utilizing a hematite-based electrode. For this purpose, hematite (or iron oxide III) attracted interest almost four decades ago thanks to its favourable attributes, such as a suitable bandgap, stability, abundance, cost-effectiveness, and very low toxicity. Nevertheless, its efficiency is hampered by poor optoelectronic features, necessitating research to improve conductivity and charge dynamics, such as controlling the physical composition and morphology in a way that is not yet fully understood. The thesis explores the preparation and characterization of hematite nanostructured films, achieved through the physical vapour deposition of iron on FTO (Fluorin-doped Tin oxide) substrates, followed by thermal treatment in an oxidizing atmosphere. This less common synthesis method provides full control of the formation of Fe oxide, together with the possibility of inducing the formation of iron-oxide nanowhiskers for an increased anode-water interface. Various characterization techniques are employed to conduct the study. Surface sample morphology is studied using Atomic Force Microscopy (AFM) and Scanning Electron Microscopy (SEM), while the composition and crystalline structure are investigated through Raman spectroscopy and Grazing Incidence X-Ray Diffraction (GIXRD). The analysis of optical properties is conducted through absorbance measurements, and finally, the study regarding the ability for water splitting is carried out via photoelectrochemical (PEC) measurements, including current-to-voltage, impedance under dark and illuminated conditions (EIS), and Controlled Intensity Modulated Photocurrent Spectroscopy (CIMPS) technique. Employing this range of experimental techniques reveals that low Fe thickness deposited and higher annealing temperatures contribute to augmented photocurrent values, attributed to the improvement of charge transport, enhanced crystalline order, and potential Sn diffusion from the substrate. Additionally, the research delves into the impedance response of the nanostructured films, unveiling promising correlations with photocurrent performance. The employed equivalent circuit, delineating charge transfer processes with characteristic times, provides insights into the physical processes at the interface between the photoanode and the electrolyte solution. The findings underscore the substantial impact of synthesis parameters on photocurrent performance and suggest a route for the fabrication of Fe-based nanostructured photoanodes with improved efficiency..

Introduction

One of the central challenges of the 21st century is ensuring an adequate energy supply to meet the desired living standards of the world's population. Fossil fuels make up approximately 81% of the world's average power consumption, which is currently 20 TW [1] and is estimated to increase up to 30 TW by 2050 [2]. At the current consumption rate, coal reserves are projected to provide energy for a span of 150 to 400 years, while oil is expected to last for 40 to 80 years, and natural gas for approximately 60 to 160 years [3]. Therefore, any technology designed for sustainable energy harvesting, conversion, and storage must be scalable to the terawatt (TW) level to have a meaningful global impact. Solar energy stands out as the most suitable contender to address the "TW challenge". However, sunlight is intermittent, which implies that schemes and devices to store and release the harvested energy in an efficient way are needed.
To address this issue, the ongoing research is focused on sunlight conversion into chemical energy, specifically hydrogen production through water splitting. It has the potential to form the cornerstone of a sustainable hydrogen-based energy economy, given the Earth's abundant water resources and the fact that the only byproduct of hydrogen consumption in a fuel cell is, again, water. Many pathways exist for the conversion of water and sunlight into hydrogen: photoelectrochemical water splitting (PEC cells), coupled photovoltaic – electrolysis systems, photobiological methods, and so on [3].
The first approach employed in this study uses solid-state electrodes in a manner similar to conventional electrolyzers. If the material is electrically polarized, it can transfer electric charges into water, initiating the water splitting reaction. Solar light assists the process by generating charges through photogeneration. In this setup, water oxidation (or oxygen evolution reaction, OER) and reduction (hydrogen evolution reaction, HER) occur at two distinct solid/liquid interfaces, respectively, at the anode and cathode sites. This approach offers several advantages. Firstly, hydrogen and oxygen are generated at separate electrodes, mitigating significant safety concerns and facilitating their efficient separation without incurring a substantial energy penalty post-separation. Lastly, a photoelectrochemical water splitting device can be constructed exclusively from inorganic materials, providing a level of chemical robustness and durability that is challenging to obtain with organic or biological systems [3].
Most of the current research is focused on determining the optimal choice for a semiconductor photoanode capable of light absorption. The critical material requirements for achieving high-efficiency photoelectrochemical (PEC) water splitting include:

- bandgap size that allows for broad light absorption
- quasi-Fermi energy levels spanning the water reduction and oxidation potentials, respectively, for electrons and holes
- efficient conversion of photogenerated charges into H_2 and O_2
- stability in working condition
- abundance, no toxicity and low cost.

While no semiconductor material meeting these opposing demands has been discovered, metal oxide materials, especially hematite, show promise. Indeed, Fe_2O_3 (or iron(III) oxide or hematite) has a very favourable $\sim$2.0 eV bandgap, which results in a theoretical absorption of 40% of solar radiation [4], with a potential to convert 15% of the sun's energy into hydrogen [5]. It also shows good

photoelectrochemical stability in a pH range from 3 to 14 [6], it represents the fourth most abundant element in the earth's crust [7], it is not toxic and exhibits a remarkably low cost [3].
Although the OER match is satisfied, by considering that the upper edge of the valence band is located approximately 0.7 eV below the OER potential [8], however, UV photoelectron spectroscopy shows that the lower edge of the conduction band is positioned 0.1–0.2 eV lower than the HER potential [9]. As a result, even in the case of heavily n-doped hematite, where the quasi-Fermi level for electrons is situated just beneath the bottom of the conduction band, achieving complete water splitting using hematite as the sole photo-absorber is not possible without an external bias [2]. In addition, hematite's efficiency is limited by its poor optoelectronic features. Iron(III) oxide is characterized by an indirect bandgap, necessitating phonon participation in the photoexcitation process. As a consequence, the absorption length in hematite is relatively long, for example, 118 nm at a photon wavelength of 550 nm [10], requiring relatively thick films. Charge transport occurs through polaron hopping, and hematite is considered as an insulator [11]. Observations from femtosecond laser spectroscopy studies on excited states in hematite nanoparticles, thin films, and single crystals reveal an ultra-fast dynamic, where hot electrons reach thermal equilibrium within 300 fs and recombine within 3 ps [12] [13]. Due to the brief lifespan and the low charge carrier mobility [2], the diffusion length for holes, responsible of the Oxygen Evolution Reaction (OER), is typically estimated to fall within the range of 1.5 to 5 nm [14]. Lastly, OER demands the involvement of four holes for each O_2 molecule produced, leading to a complete cycle that can extend for several seconds on hematite [2]. Even though the processes at solid/liquid interface are a current subject of debate, a number of works have highlighted the central role of surface states in the kinetic operation in water splitting conditions with a strong influence on PEC efficiency [15] [16].
In order to face these challenges and intrinsic limitations, research efforts are focused on increasing conductivity by raising the ionized donor concentration through doping and enhancing charge dynamics by controlling electrode morphology [3]. This strategy is adopted by the DFA Nanostructures Group Research, where this work is assigned and involves specifically Sn doping and nanowires structure. This particular morphology allows for an increase in the surface reaction sites and overcomes several trade-offs: large film thickness and short hole diffusion length, high doping levels and space charge layer reduction.
The study presented in this thesis concerns the preparation and characterization of hematite nanostructured films deposited on FTO (F:SnO_2, fluorine-doped tin oxide). The preparation of the sample was realizable by means of sputtering deposition and thermal annealing, instead of the most common hydrothermal synthesis, in order to have better parameter control and more resistance structure [17]. The main focus is the investigation by different experimental techniques of the key parameters to obtain an acceptable photocurrent value (0.2 mA/cm^2 under 100 mW/cm^2 illumination and at standard reference potential, i.e. 1.23 V vs RHE [18]), and the study of the processes involved through impedance spectroscopy. The thesis work is structured into five chapters:

Chapter 1 Basic principles of water splitting and some fundamental concepts about photoelectrochemical cells are given.

Chapter 2 Sample preparation and experimental setup are described. Specifically, magnetron sputtering and characterization techniques are illustrated: X-Ray Diffraction (XRD), Scanning electron Microscopy (SEM), Raman and UV-Vis spectroscopy, Atomic Force Microscopy (AFM), Photo-ElectroChemical (PEC), Electrochemical Impedance Spectroscopy (EIS) and Controlled Intensity Modulated Photocurrent Spectroscopy (CIMPS) techniques. The research directions are also outlined, along with a list of samples under examination.

Chapter 3 After a brief discussion on nanowire growth, the crystalline structure, optical properties and morphology of the samples under study are presented.

Chapter 4 The experimental results of PEC and impedance measurements are described, along with an explanation of the analysis method based on the equivalent circuit (EC). The results of CIMPS measurements of the sample, which shows the greater photocurrent, are presented.

Chapter 5 Conclusions, ongoing studies, and future perspectives will be discussed.

Chapter 1

Water splitting and photoanodes

In this chapter, some fundamental concepts of photoelectrochemistry are explained. These concepts include the water splitting reaction, the photoelectrochemical cell, and the interface between the electrode and the solution. Finally, the photoelectrochemical (PEC) cell is illustrated under both dark and illuminated conditions.

1.1 Water splitting

The water splitting reaction consists of two half-reactions: the Oxygen Evolution Reaction (OER) and the Hydrogen Evolution Reaction (HER). The reduction half-reaction involves a two-electron transfer, while the oxidation of water to form oxygen requires a four-electron transfer. The thermodynamic potential required for water splitting is 1.23 V vs RHE, where RHE stands for Reversible Hydrogen Electrode. It is a reference electrode suitable for electrochemical processes because its measured potential does change with the pH, so it can be directly used in the electrolyte. In the case of acidity, water splitting reaction is commonly carried out with a proton exchange membrane (PEM), offering the advantages of high energy efficiency and rapid hydrogen production. However, the use of acidic environments restricts the choice of electrocatalysts for the hydrogen evolution reaction (HER) and oxygen evolution reaction (OER) to precious metals and metal oxides, consequently increasing the overall cost of PEM systems. In contrast, when performed in alkaline conditions, water electrolysis opens the door to a broader array of electrocatalyst materials, many of which are readily available in nature. In the context of an alkaline solution, the Hydrogen Evolution Reaction (HER) has been theoretically elucidated by Volmer and Heyrowsky [19]. Conversely, there remains some uncertainty about the actual molecular reaction mechanisms of the Oxygen Evolution Reaction (OER), which, however is characterized by a sluggish kinetics. The principal challenge in facilitating the OER lies in the development of catalysts that operate with the lowest feasible overpotential. Presently, state-of-the-art materials primarily comprise noble metals, such as Ir or Ru and their corresponding oxides. However, their prohibitive cost and limited availability impose constraints on their broad applicability [20]. In recent years, the scientific community has redirected its focus towards transition metal oxides derived from naturally abundant resources. These materials, characterized by their cost-effectiveness and ready availability, also demonstrate exceptional resistance to corrosion. Moreover, they possess multivalent oxidation states ($M^{+2/+3/+4}$), which serve as active sites in the OER process.

1.2 PEC cell

The PEC cell is the device where the water splitting reaction takes place, thanks to electrostatic energy and light. One possible schematic of it is illustrated in Fig. 1.1, where the cathode (or counter electrode, CE) is made of metal, and the anode (or working electrode, WE) is composed of a semiconductor. The latter is the key component of the device: when it is electrically polarized and illuminated, the (photo)-generated electrons and holes separate and reach the back contact and the solution, respectively. At

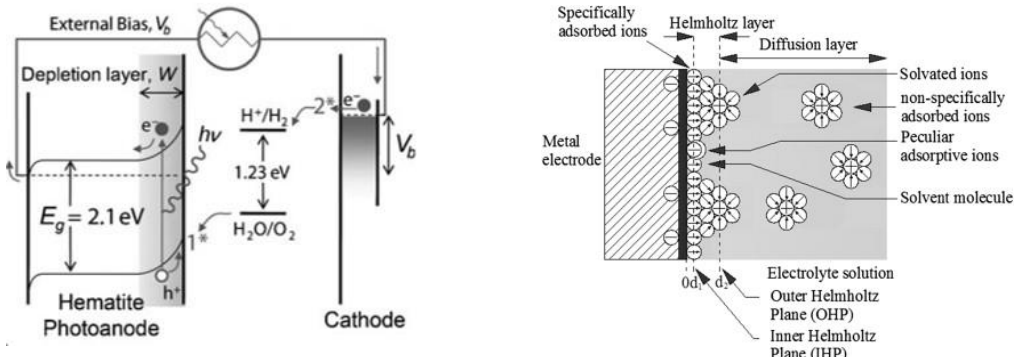

Figure 1.1: PEC cell simplified diagram [2] (left) and electrode/solution interface scheme [21] (right).

the cathode, the reduction reaction occurs, resulting in the production of H_2, while at the anode, the oxidation reaction takes place, leading to the production of O_2.

When a metal electrode is placed in an electrolyte solution, it typically results in the establishment of an equilibrium difference between the metal and the solution. This equilibrium state is obtained as the remaining electrons within the metal actively participate in generating a layer of ions, bearing an opposite charge to that of the cations present in the solution at the interface. The combination of positive charges from cations in the solution and negative charges from electrons within the metal electrode gives rise to what is known as the electrical double layer. Water molecules, due to their polar nature, are attracted to the metal electrode, contributing to the establishment of a potential difference. These molecules constitute the initial adsorbed layer on the metal's surface. Hydrated cations, which are drawn toward the metal surface, encounter limitations in their proximity due to the presence of H_2O molecules on the metal surface. When electrostatic interactions come into play, ions from the solution phase approach the electrode only as far as their solvation sheath permits. The array of these ions on the surface is thus shielded from direct contact with the electrode by a layer of solvent molecules. The line running through the centre of these solvated cations at their closest approach is known as the *outer Helmholtz plane* (OHP). Instead, the locus of the electrical centres of the layer, closest to the electrode, constituted of solvent and adsorbed ions, is called the *inner Helmholtz plane* (IHP). This situation is depicted in Fig. 1.1(right). Lastly, the non-specifically adsorbed ions are dispersed in a region referred to as the diffusion layer, and the thickness of this layer is determined by the ionic concentration in the electrolyte. The region between IHP and OHP, called *Helmholtz layer*, has a width of about a few Å and gives rise to a potential drop V_H, which depends on the charge accumulated. It can be treated as a capacitor C_H and has a typical value of 10-20 $\mu F/cm^2$ [3]. The benefit of measuring the semiconductor's potential in relation to a reference electrode is that the measured potential difference remains independent of the current flowing through the cell. In contrast, the potential difference between the semiconductor and the metal counter electrode relies on V_H at the metal electrode, which varies unpredictably with the current.

The Helmholtz layer is also built on the other side of the PEC cell at the semiconductor(SC) electrolyte interface. In this particular scenario, the adsorbed ions are found within the Helmholtz layer, as explained earlier, whereas the charges on the SC's surface result from electrons (or holes) trapped in surface states or H^+ or OH^- ions that are continuously adsorbed and desorbed. The energy levels of these surface states lie below the conduction band minimum, and as a result, free electrons from the bulk material occupy these levels. The ionized donors, from which the free electrons originated, naturally remain within the bulk, where they create a positive space charge. This situation leads to the development of an electric field, and the transfer of charge from the bulk to the surface persists until the potential barrier becomes too significant for bulk electrons to overcome. A dynamic equilibrium is therefore reached, giving rise to what is known as the *space charge region*(SCR). In Fig. 1.2 the

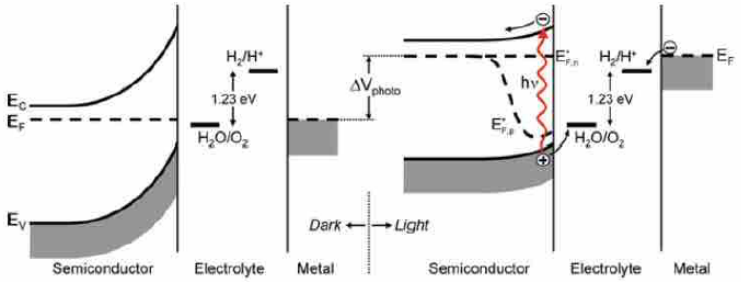

Figure 1.2: Energy band diagram of semiconductor in contact with an electrolyte in dark condition (left) and under illumination and applied voltage bias (right) [3]

consequent band bending is shown. Considering a PEC cell in operation, particularly when an applied potential is present, the behaviour of the SCR and Helmholtz layer can be described as two capacitances in series, with their equivalent capacitance being:

$$\frac{1}{C} = \frac{1}{C_H} + \frac{1}{C_{SCR}} \tag{1.1}$$

If the solution is highly concentrated (>0.1 M), it is correct to consider $C_H >> C_{SCR}$ and neglect the second term in Eq. (1.1), with the direct consequence that changes in the applied potential will affect the SCR. Conversely, under illumination conditions and applied potential, SC/electrolyte energy band diagram changes as shown in Fig. 1.2(right). The photon, if its energy is greater than the SC energy gap, creates an electron-hole pair and leads to a reduced band bending and an increase of Fermi level by the so-called *internal photovoltage* ΔV_{photo}. Since the situation is not at the equilibrium, the Fermi level splits into two *quasi-Fermi levels*, respectively $E^*_{F,n}$ for e^- and $E^*_{F,p}$ for h^+. They are linked to concentrations of carriers in SC (n,p respectively), and in the case of a n-type material, the additional carriers created by illumination Δn and Δp have a different effect. The first one is negligible respect to equilibrium dark concentration, instead p $\approx \Delta$p. Therefore $E^*_{F,n}$ still remains horizontal and $E^*_{F,p}$ starts for bulk Fermi level and drops down toward the surface, facilitating the hole transfer from valence band and oxidation reaction. A photocurrent is created and can be linked to incident photon flux by equation:

$$j = j_0 + e\Phi\left(\frac{1 - e^{-\alpha W}}{1 + \alpha L_p}\right) \tag{1.2}$$

where j_0 is the saturation current density, Φ is the incident light flux, α is the absorption coefficient, W is the SCR width, and L_p is the hole diffusion length. This expression is derived from the Gartner model, which assumes no recombination in SCR and interface [3].

Chapter 2

Experimental methods

In this chapter, experimental methods are presented. In particular, the nanostructured thin films under the scope of the thesis were synthesized through physical vapour deposition and subsequent thermal treatments. The surface morphology was studied using Atomic Force Microscopy (AFM) and Scanning Electron Microscopy (SEM), while the composition and crystalline structure were investigated through Raman spectroscopy and Grazing Incidence X-Ray Diffraction (GIXRD). The analysis of optical properties was conducted through absorbance measurements, and finally, the study regarding the ability for water splitting was carried out via photoelectrochemical (PEC) measurements, including current-to-voltage, impedance under dark and illuminated conditions (EIS), and Controlled Intensity Modulated Photocurrent Spectroscopy (CIMPS) technique. The experimental conditions and a list of the samples under study are provided.

2.1 Physical vapour deposition

The deposition of thin films via physical vapour deposition allows for the use of a plasma, typically Argon (Ar), to erode a target and deposit the atoms produced in the erosion process onto a substrate positioned at a suitable distance. Magnetron sputtering, used in this work, pertains to this category of deposition method and uses magnetic configuration to confine the plasma near the surface of the target material. Its atoms or molecules are expelled as a result of the momentum transfer caused by the impact of highly energetic plasma particles. The expelled material can then be directly deposited onto substrates [23]. To effectively utilize sputtering as a coating method, several criteria must be satisfied. Firstly, generating ions with sufficient energy is necessary to eject atoms from the target material. Additionally, the ejected atoms must have the freedom to move towards the target surface with minimal hindrance. Therefore, sputter coating is conducted in a vacuum environment, requiring low pressures to maintain high ion energies and reduce atom-gas collisions after ejection from the target. One crucial aspect for maximizing the efficiency of the deposition process is to optimize the sputtering yield. The sputtering yield represents the ratio of atoms sputtered to the number of high-energy incident particles. This ratio depends on the mass of the bombarding particle, the chemical bonding of the target atoms, and the energy transferred during collisions. The sputtering yield is also sensitive to the angle of incidence of the bombarding particle. For off-normal bombardment, the ratio initially increases to a maximum but then rapidly decreases when most of the bombarding particles are reflected from the surface. Additionally, there is a threshold energy below which sputtering does not occur, regardless of the bombarding flux. Conversely, when the kinetic energy of ions is too high, they lose much of their energy far below the surface, making the ejection of a target ion more challenging. Consequently, the sputtering yield progressively decreases [26]. When sputtering is induced by bombarding the target with energetic ions alone, the deposition rates are typically too low for practical purposes. The time required for a deposition would be excessively long. This led to the development of magnetron sputtering, where one or more magnets are placed near the target holder to create a strong magnetic field that deflects electrons and keeps them close to the target in a closed path, as shown in Fig. 2.1 (left). This containment of the plasma near the target increases its density,

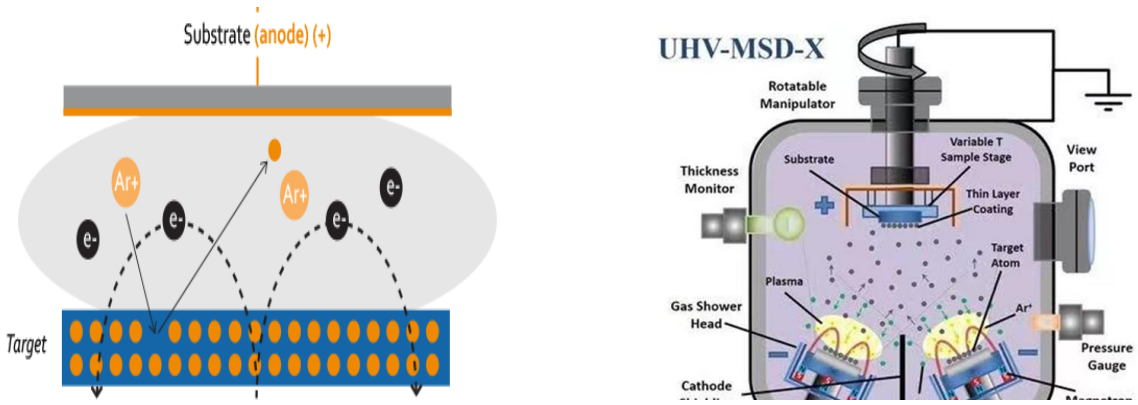

Figure 2.1: Principles of magnetron sputtering, where Ar plasma erodes a target and allows it to deposit its expelled atoms onto a substrate [25](left). A schematic view of a magnetron sputtering setup similar to what is used in this work [27](right).

accelerates the sputtering process, and, consequently, improves deposition rates. The configuration of the electrical field inside the chamber depends on the target material. For the deposition of a conductive material, a simple direct current (DC) setup can be employed. In this setup, the sample holder is grounded, and the target is maintained at a fixed negative potential. However, when working with insulating or semiconductor materials, this configuration is inefficient. Since no current can flow through the target, ionized bombarding atoms cause a charge buildup on its surface. To address this issue, a solution is to use radiofrequency (RF). In an RF setup, an alternating current at high frequency is employed to impact the target with both positive and negative ions alternately, thereby preventing charge accumulation. The magnetron sputtering setup used to synthesize the samples in this study is illustrated in Fig. 2.1(right). It consists of a cylindrical vacuum chamber. Initial vacuum conditions are achieved with a rotary pump, and a turbomolecular pump is used to attain the high vacuum level (approximately 10^{-6} mbar) necessary to remove gases like oxygen or water vapour from the chamber, which could adversely affect the deposition quality. A feedback system, connected to a pressure gauge, maintains a constant pressure set in the range of 10^{-2} to 10^{-3} mbar once argon (Ar) is introduced into the chamber. On one side of the chamber, there is the sample holder, which can continuously rotate during deposition to ensure uniform film deposition. Multiple substrates can be placed on the sample holder, enabling the synthesis of multiple samples under the same conditions. On the other side of the chamber, three target holders (referred to as torches), each equipped with a shutter, are positioned. The sample holder, acting as the anode is grounded, while the torches, functioning as cathodes, are connected to their own individual DC or RF power supplies. This setup allows the simultaneous deposition of up to three different materials in a single sputtering session. The shutters also serve the important function of pre-sputtering the target, which removes potential surface layers of oxide or contaminants before the actual deposition process. This can be achieved by keeping the shutter closed while igniting the plasma near the target. All torches can be tilted at different angles toward the sample holder, and the sample holder itself can be adjusted to be closer or farther from the torches. The setup is additionally furnished with a water cooling system to manage the heat within the chamber and its components. Thermal stress remains a concern for the target, as it has the potential to cause damage and potential contamination from atoms sputtered by the target holder. The use of iron as a target involves the presence of magnetic fields during the process due to its ferromagnetic nature. It is important to monitor and optimize these magnetic fields to ensure a uniform and controlled deposition of the thin film.

2.2 Grazing Incidence X-ray Diffraction

X-ray diffraction analysis (XRD) is a non-invasive method employed for determining the crystallographic arrangement of a material. It works by exposing a material to incident X-rays and subsequently gauging the intensities and scattering angles of the X-rays emitted from the material. The

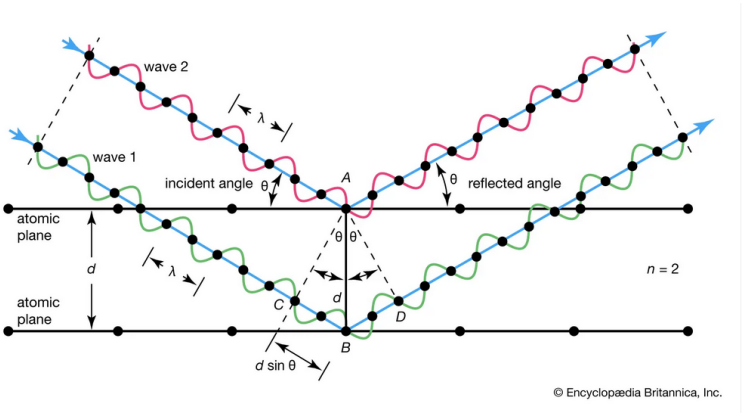

Figure 2.2: Principle of X-Ray diffraction and Bragg's law

working principle is based on the Bragg law depicted in Fig. 2.2:

$$n\lambda = 2d\sin\omega \tag{2.1}$$

where n is an integer number, λ is the incident X-ray wavelength, d is the lattice plane spacing and ω is the angle of incidence of X-rays with respect to the crystal planes. An XRD measurement is conducted using a diffractometer, and its most prevalent configuration is the Bragg-Brentano setup (Fig. 2.3 (a)), where the emission and detection points are positioned on the goniometer circle. At the same time, the specimen resides at its centre. A single $(\omega - 2\theta)$ scan is generally conducted with the sample held stationary while moving the source and detector, where 2θ refers to the detection angle. Another configuration employed in this study is Grazing Incident X-Ray Diffraction (GIXRD), which

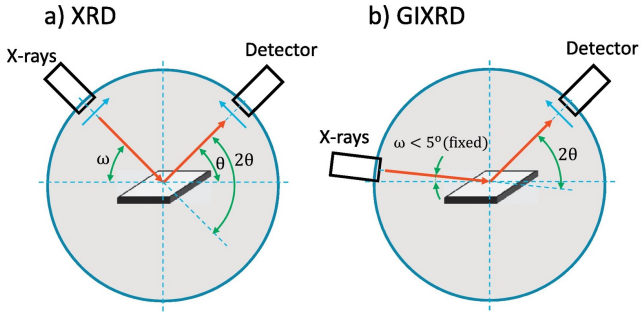

Figure 2.3: A schematic view of Bragg bentano (a) and GIXRD (b) configuration [28].

is particularly well-suited for characterizing thin films. It consists of performing a 2θ scan with a fixed grazing angle of incidence. In this way, it is possible to avoid intense signals from the substrate and get stronger signals from the film itself. The fixed angle is generally chosen to be slightly above the critical angle for the total reflection of the film material (about 0.3°for Fe_2O_3 and $Cu_K\alpha$ radiation, which has λ= 1.54 Å).

The diffractometer is composed of an X-ray source emitting monochromatic radiation consisting of an anode target and a filament cathode. In the latter, an electric current flows, leading to the emission of electrons through the thermionic effect. These electrons are subsequently accelerated towards the anode due to an applied potential. X-rays are emitted from the tube through a beryllium window, with beam divergence controlled by the use of slits. If necessary, a mirror can be used to focus and concentrate the X-ray beam. The crystalline sample is placed on a sample holder, and the goniometer allows precise rotation of the sample around various axes, enabling the desired orientation with respect to the incident beam. A parallel plate collimator reduces the beam divergence, ensuring that only parallel X-rays strike the sample. The detector, often based on advanced technologies like silicon detectors, detects the X-rays scattered by the sample. This component is mounted on an angular scanning system to acquire diffraction data at different 2θ angles. The entire system is controlled by dedicated software that manages the goniometer's movement and records detector data. In this

work, the diffractometer used is Philips X'Pert Pro, provided by a Cu anode; so, the radiation used was $Cu_K\alpha$ with an E = 8.040 keV. The incident angle ω is chosen to be 1°or 3°, with a consequent penetration depth for $Cu_K\alpha$ radiation of 153, 470 nm respectively. A voltage of V=40 kV was applied, with a current of I=40 mA passing through the filament cathode. To minimize divergence, a vertical slit of (1/8°) was employed. Furthermore, all measurements were conducted with the use of a parallel plate collimator (PPC) to enhance control over the X-ray beam's divergence. The sample holder is usually made of plexiglass.

2.3 Atomic Force Microscopy

First invented by G. Binnig in 1986 [31], Atomic Force Microscopy (AFM) is a highly sensitive technique capable of visualizing and measuring the surfaces of various solid materials with exceptional resolution and atomic-scale accuracy. Unlike other microscopy methods, such as optical or electron microscopy, AFM does not create images by focusing light or electrons onto the surface. Instead, it employs a sharp probe to detect the sample's surface topography, constructing a topographical map of the surface's height. To create this map, it relies on the interaction force between a probe positioned at the nanoscale distance from the sample. Subsequently, the data collected from an AFM must be analyzed to generate a meaningful image. Despite its apparent complexity, this instrument allows for the acquisition of two- or three-dimensional images detailing the sample's topography. Additionally, it can provide quantitative information regarding the height, length, width, or volume of features within the image. The principal components of an Atomic Force Microscope (AFM) include the following elements:

Probe Typically, the probe consists of a sharp tip affixed to a flexible cantilever spring. This arrangement permits the analysis of the interaction between the tip and the sample by monitoring the motion of the cantilever.

Deflection sensing device A device is essential to sense and quantify the deflection of the cantilever when it interacts with the sample.

Feedback system The feedback system is employed to continuously monitor and control the deflection of the cantilever during measurements.

Scanning system Mechanical scanning system, often using piezoelectric materials, facilitates the movement of the sample relative to the tip in a raster pattern. Corrections to the sample's positioning are made based on input from the feedback system.

Display system A display system is included to transform the measured data into visual images.

Commonly used materials for AFM probes include silicon nitride (Si_3N_4), silicon (Si), or other materials with low thermal expansion coefficients. It is important to note that the sharpness and consistency of manufactured probes are critical factors affecting the quality of AFM results. Additionally, while sharper probes can enhance image resolution, the production of probes with a reproducible tip radius below 10 nm at a reasonable cost remains a significant challenge [35]. The detection of cantilever bending can be accomplished using various methods. In the early AFM devices, such as the one introduced by Binnig, tunnelling tips were employed above the conductive surface of the cantilever. While this method is highly sensitive, subsequent systems often adopt simpler optical techniques, such as interferometry or light beam deflection. These optical methods do not necessitate the tip to be conductive. Among the optical techniques, interferometric methods offer higher sensitivity but are also more intricate compared to the "beam-bounce method" used in this work. The beam-bounce method takes advantage of the reflection of an optical beam emitted by a laser source from the mirrored surface on the backside of the cantilever onto a position-sensitive photodetector. In this configuration, depicted in Fig. 2.4, the tilt of the cantilever resulting from its interaction with the sample can be quantified by observing changes in the position of the beam on the photodetector [36]. Following the Lennard-Jones (L-J) potential, attractive interactions are characterized as Van der Waals forces that decay with distance, represented by a term of d^{-6}, while repulsive interactions are modelled using a

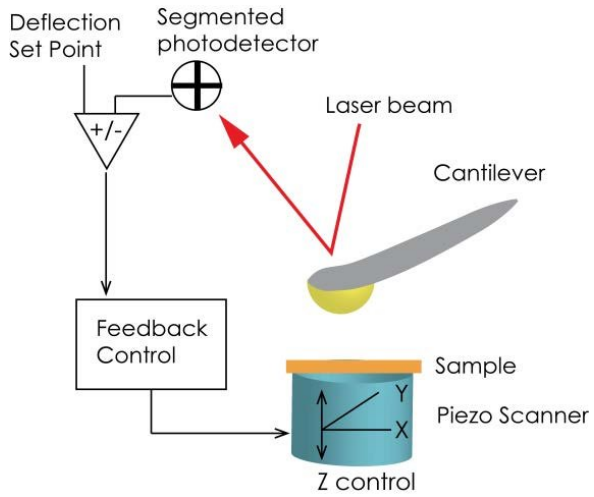

Figure 2.4: A schematic view of an Atomic Force Microscope in beam-bounce detection mode [32].

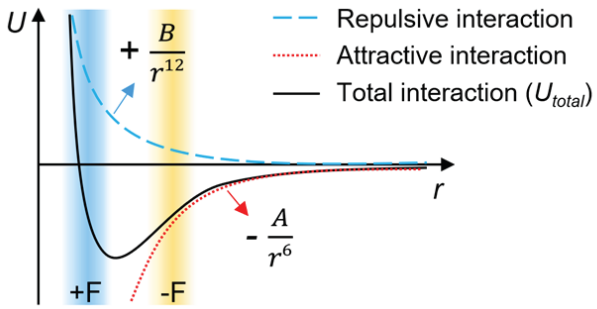

Figure 2.5: Plot depicting the interaction U between the AFM tip and the surface as a function of their separation distance r. The blue curve represents a purely repulsive interaction, while the red curve represents a purely attractive interaction. The black curve is a combination of long-range attractive and short-range repulsive interaction forces called the Lennard-Jones Potential. It shows approximate regions for the contact mode (blue rectangle) and non-contact mode (yellow rectangle). [34].

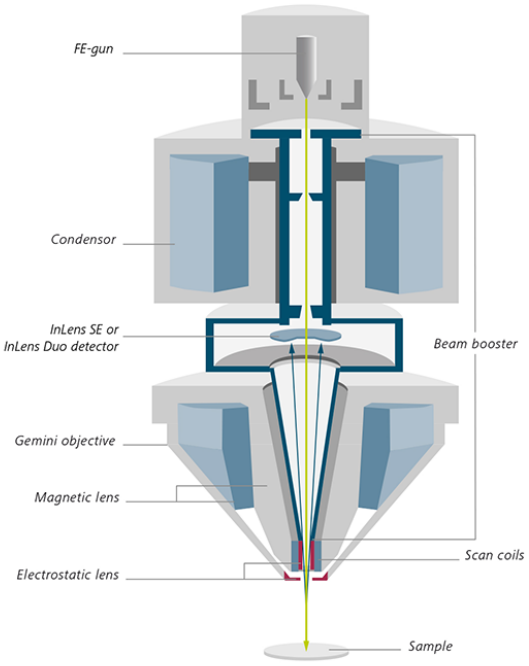

Figure 2.6: A schematic view of a Zeiss Sigma HD FE-SEM [29].

power-law approach and decay more rapidly with a term of d^{-12}. The L-J potential curve, illustrated in Fig. 2.5, can be divided into two distinct regions: a short-distance and a long-distance region. In the short-distance region, repulsive interactions predominate, whereas in the long-distance region, attractive forces become significant. This differentiation in the curve allows for the categorization of AFM operating modes into three types: contact mode, non-contact mode, and tapping mode (or semi-contact mode), determined by the tip-sample distance [33]. In contact mode, the tip remains in continuous contact with the sample surface during the scanning, and the measured parameter is the deflection of the cantilever, providing insights into the sample's morphology. In non-contact mode, the tip oscillates at its resonance frequency and hovers near the sample without direct physical contact. The tip-sample distance maintained either in constant height mode (z distance) or constant force mode, is regulated via a feedback loop process. This feedback mechanism can be based on the tip's oscillation amplitude or frequency, with a common set value typically defined as 75% of the oscillation amplitude at the resonance frequency. Variations from the initial set value and the displacement from it are recorded to collect morphological data. In semi-contact mode, the tip oscillates similarly to the contact mode but makes slight intermittent contact with the sample surface, experiencing both attractive and repulsive interactions. In this study, an NT-MDT Solver Pro AFM was employed, equipped with a Si probe having a curvature radius of 10 nm and a tip height in the range of 14-16 µm. All measurements were carried out in semi-contact mode. The data collected underwent analysis using Gwyddion software, enabling the application of geometric operations to level the data.

2.4 Scanning Electron Microscopy

Scanning Electron Microscopy (SEM) is an imaging method that enables the acquisition of nanoscale to microscale details regarding the morphology (size and shape) and composition of a given specimen. It involves directing a focused beam of high-energy electrons at the sample, resulting in the emission of secondary electrons, backscattered electrons, Auger electrons, and X-rays through elastic and inelastic scattering. These emissions are detected by a detector, thus creating a high-resolution 3D image of the sample under examination. A schematic diagram of the instrument is depicted in Fig. 2.6. The electron beam is created using an electron source (such as thermionic, Schottky, or field-emission cathode), to which a high negative voltage is applied, and then it is accelerated to an energy typically ranging from

0.1 to 30 keV. A tungsten filament with a sharp end is commonly used for this purpose. The beam is then shaped by a system of openings, electrostatic or magnetic lenses, and electromagnetic coils, which progressively reduce the beam's diameter and adjust its path to focus it precisely on the sample placed on a stage in a grid pattern. This allows for the scanning of a large area of the sample. The smaller the beam diameter, the higher the spatial resolution achieved. All the components of this setup are enclosed within a vacuum chamber with pressure levels below 10^{-6} mbar. This vacuum environment is necessary to minimize undesired electron scattering caused by traces of gas, which could disrupt the path of the electrons, decrease beam intensity, and increase noise. SEM enables both qualitative and quantitative analyses, applicable to a wide range of materials. However, insulating specimens need to be coated with a conductive layer or carbon tape to mitigate the accumulation of surface electrical charge resulting from electron impacts [30]. The image formation relies on a Cathode Ray Tube (CRT). Electrons strike a scintillator, generating radiation that is then captured by a photomultiplier. This captured radiation is converted into an electrical signal that influences the intensity of a point on the CRT [20]. All the images in this study were acquired utilizing a Zeiss Sigma HD Field Emission Scanning Electron Microscope (FE-SEM). The instrument features a tungsten (W) tip that emits electrons when subjected to a current of $10^{-6} A/cm^2$. Furthermore, it is equipped with three detectors for secondary electrons (SEs), backscattered electrons, and X-rays. Only the images of secondary electrons (SEs) were employed in this study.

2.5 Raman spectroscopy

Raman spectroscopy is a spectroscopic technique based on the Raman effect that provides a characteristic spectrum of specific vibrations in a molecule and allows for obtaining information about the composition and, often, the crystalline structure of a material. The Raman effect is a phenomenon of inelastic light scattering that interacts with the molecules of a gas, liquid, or solid, exciting them to a higher energy level. Upon returning to a lower vibrational level, the molecules emit a photon with a certain frequency. In particular, by directing a laser onto a sample, a smaller percentage of light (1 photon in 10 million) undergoes inelastic scattering: the beam is scattered with a frequency higher or lower than the original, and the difference in frequency between the incident and scattered rays is called the "Raman shift". If the energy level of the scattered photon is higher than the incident photon, the Raman-Stokes phenomenon occurs; if it is lower, it is referred to as Raman Anti-Stokes. Since the frequencies shift are specific to both the molecule and the types of bonds within it, identifying these absorbed frequencies enables to determine the molecules present in the sample. The instrument used to detect this effect is a Raman spectrometer system, depicted in Fig. 2.7, which comprises three key components: a high-intensity solid-state laser, a sample interface and a spectrometer. The

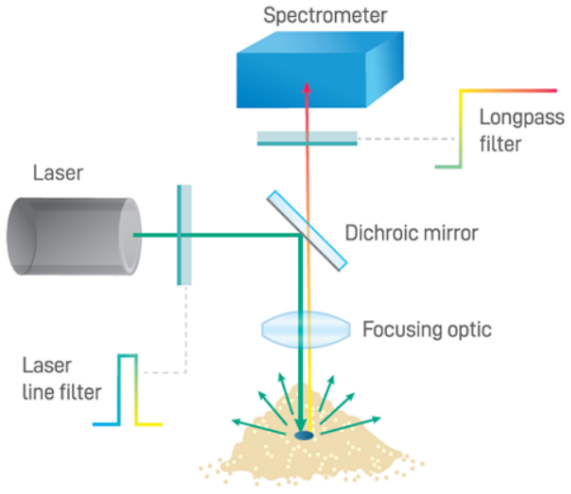

Figure 2.7: A schematic view of Raman spectrometer [37].

high-intensity laser serves as the excitation source, providing the intense light necessary for generating

detectable Raman signals. Raman scattering is a relatively rare event, occurring at a probability of one part in a million, hence the need for high laser intensities to compensate for this rarity. While it is possible to use any wavelength to produce a Raman spectrum, the excitation wavelength is the crucial factor influencing Raman signal intensity. The intensity of Raman scattering is inversely proportional to the fourth power of the excitation wavelength (λ^{-4}). This implies that shorter laser wavelengths result in stronger Raman signals and vice versa. However, shorter wavelengths are more likely to induce autofluorescence, which can obscure the Raman signal. Thus, the selection of the appropriate laser wavelength primarily depends on the type of sample, balancing signal intensity against autofluorescence for the material under examination. The sample interface of the Raman spectrometer system comprises the optics responsible for directing, focusing, and collecting the relatively weak Raman emissions for transmission to the spectrometer. Typically, a longpass dichroic filter is employed to reflect the shortwave laser light onto the sample and transmit Raman scattered light to the spectrometer, as illustrated below. In addition, the sampling optics often incorporate an additional longpass filter with a minimum optical density (OD) of 6 to block the predominant Rayleigh scatter originating from the excitation laser light. Raman system sampling optics are available in various optical configurations. Some employ fibre optic coupling, enabling the integration of sampling optics into a probe for remote use with the spectrometer, while others utilize fully integrated sampling optics to reduce the system's size and minimize optical losses. Finally, the Raman spectrometer simultaneously captures and detects all the light that passes through the sample interface, providing a spectrum that shows the Raman shift (expressed in cm^{-1}) in relation to the laser frequency. This requires a sufficient range, strong signals, and good optical resolution. Important performance characteristics include sensitivity, a good signal-to-noise ratio, and the ability to collect a lot of light, expressed as numerical aperture (NA). This work utilizes a Horiba Raman Spectrometer. The spectra are obtained using a 638 nm laser with 30 mW power, a 1800 grating (450-850 nm) and an acquisition time of 5 seconds, with a signal accumulation of 20.

2.6 UV-Vis spectroscopy

UV-Vis spectroscopy is a method used to investigate the linear optical characteristics of materials within the UV-Vis-NIR range (200 nm to 2500 nm). It involves measuring the intensity I_0 of monochromatic radiation and the transmitted intensity I, which is affected by absorption, reflectivity, and scattering phenomena. The resulting spectrum is typically expressed in terms of transmittance (T) or absorbance (A), which are related through the following equations:

$$T = \frac{I}{I_0} \qquad A = -log(T) \tag{2.2}$$

The measurement is conducted using a spectrophotometer, comprising a monochromatic source, a sample holder, and a detector. To ensure the availability of monochromatic radiation across a broad range, a continuum-emitting source is used, in conjunction with a monochromatic system, typically employing a diffraction grating, before passing through the sample. Spectrophotometers can be configured in various ways: single beam, double beam in time, and double beam in space. In the single beam configuration, it is necessary to measure the reference (I_0) separately. The double beam configuration allows simultaneous measurement of both the reference (I_0) and the sample (I). In the double beam in time configuration, the beam is alternately directed to the sample and reference using a chopper. In the double beam in space configuration, the beam is divided into two paths, one directed to the sample and the other to the reference. In this latter configuration, two identical detectors are employed to measure I_0 and I. In this study, the absorption spectra of the samples were measured using a double-beam spectrophotometer Jasco V-670 (Fig. 2.8). The instrument is equipped with two light sources: a deuterium lamp, covering wavelengths between 190 to 350 nm, and a halogen lamp, covering wavelengths from 350 to 2500 nm, each having its own diffraction grating. Additionally, the instrument features two detectors: one for the UV-Vis range (photomultiplier tube, PMT) and another for the NIR range (Peltier-cooled PbS detector). The spectra recorded are in terms of percentage trasmittance in a wavelenght range from 300 nm to 1100 nm, using 100 nm/min scan rate and 1.0 nm and 4.0 nm bandwidth for UV-Vis and NIR range respectively.

Figure 2.8: Spectrophotometer Jasco V-670

2.7 Photoelectrochemical analysis

Photoelectrochemical (PEC) techniques encompass a range of experimental methods used for the determination of electrical and chemical properties of materials, including their interaction with light, in conjunction with an electrolyte within a PEC cell. These techniques can be categorized into static and dynamic approaches. In the static category, the analyte solution is not subjected to current flow. An illustrative example is the Open Circuit Potential measure (OCP), where the cell potential is measured under static conditions. In the dynamic category, the current is allowed to flow through the analyte solution. To this branch belongs amperometry and voltammetry, which entail the measurement of current as a function of a fixed or variable potential, respectively. Another possible classification is the division into stationary and small-perturbation techniques, which can be Electrochemical Impedance Spectroscopy (EIS), Intensity-Modulated Photocurrent Spectroscopy (IMPS), and Intensity-Modulated Photovoltage Spectroscopy (IMVS). In the former, a potential perturbation is introduced, while in the latter two, a perturbation of light intensity that affects the sample is applied. The techniques used in this work, namely linear sweep voltammetry (LSV), EIS, and IMPS, are now described in greater detail. In LSV, the potential v is linearly varied over time from an initial potential V_i to a final one V_f at a scan rate dV/dt, while the current is sampled (see Fig. 2.9). It can be conducted with or without sample illumination, and in this work, it is referred to as *I-V dark* and *I-V light*, respectively. The scan rate used is 5 mV/s, and the range is typically from 0.9 to 2.0 V vs RHE.

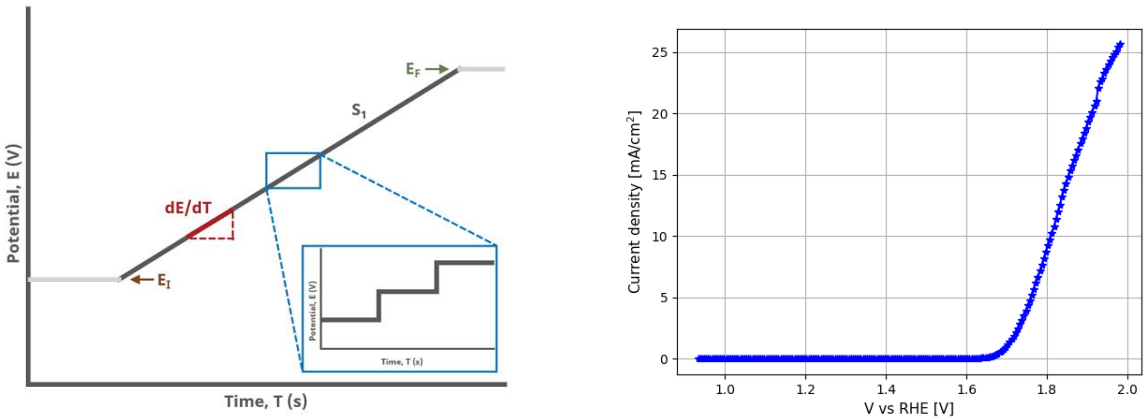

Figure 2.9: Principles of Linear Sweep Voltammetry (left). An example of the current-to-voltage output response of LSV. The data refers to the sample with 45 nm Fe deposited and annealed for 2h at 480°C (right).

EIS, instead, is a transfer function technique that models the output signal (AC current I) to the input signal (AC voltage V) over a wide range of frequencies f as follows:

Input $\mathrm{V} = V_0 \sin(2\pi f t) + V_{DC}$

Output $\mathrm{I} = I_0 \sin(2\pi f t + \phi)$

Transfer function $\mathrm{Z} = \frac{V}{I} = \mathrm{Re}[Z(f)] + j\,\mathrm{Im}[Z(f)]$

where Z is the total impedance of the system, which can be divided into its real and imaginary components. They are related by Kramers-Kronig relations [40]:

$$\mathrm{Re}[Z(\omega)] = \mathrm{Re}[Z(\infty)] + \frac{2}{\pi}\int_0^\infty \frac{u \cdot \mathrm{Im}[Z(u)] - \omega \cdot \mathrm{Im}[Z(\omega)]}{u^2 - \omega^2}\,du \tag{2.3}$$

$$\mathrm{Im}[Z(\omega)] = \frac{2\omega}{\pi}\int_0^\infty \frac{\mathrm{Re}[Z(u)] - \mathrm{Re}[Z(\omega]}{u^2 - \omega^2}\,du \tag{2.4}$$

where $\omega = 2\pi f$. A schematic view is depicted in Fig. 2.10. It is essential to apply a small-amplitude

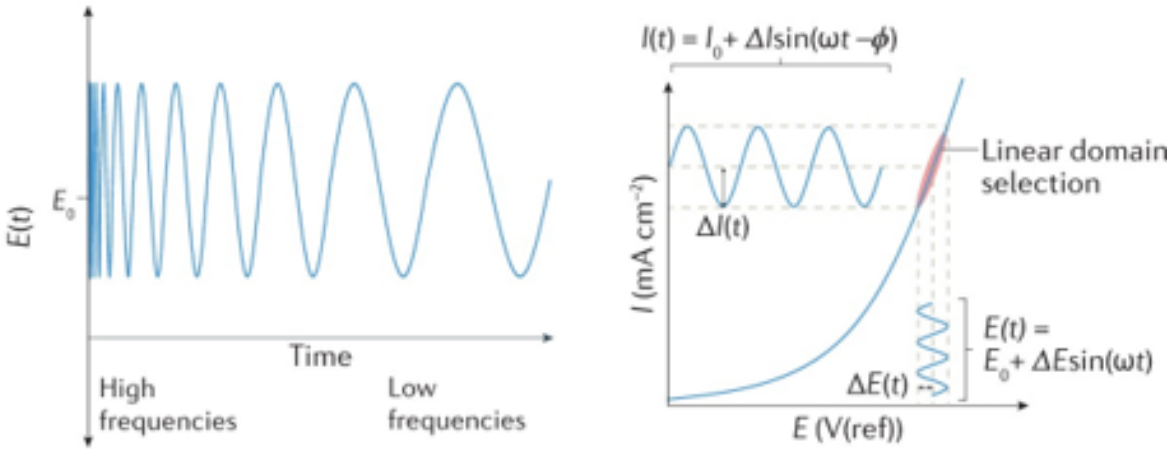

Figure 2.10: Principles of Electrochemical Impedance Spectroscopy (EIS) [39]

perturbation, denoted as V_0, to ensure a linear relation between the applied signal and the system's response. Additionally, it is assumed that the system is stable, meaning that it returns to its original state once the perturbation stops. This technique allows for the investigation of Linear Sweep Voltammetry (LSV) curves in the frequency domain, making it possible to detect the underlying charge transfer processes and their underlying dynamics, each characterized by different time constants and resonating at distinct frequencies. Usually, data are plotted in a Bode plot, in a $\mathrm{Re}[Z]$ or $\mathrm{Im}[Z]$ vs f or in the more common $-\mathrm{Im}[Z]$ vs $\mathrm{Re}[Z]$, called Nyquist plot (see Fig. 2.11). If the measure is performed by illuminating the sample, it is called Photoelectrochemical impedance spectroscopy (PEIS).

If the small perturbation pertains to light intensity, the transfer function $Q(\omega)$ relates the extracted current density $\widetilde{j_e}$ to the perturbation of the incident photon flux $\widetilde{\phi}$, enabling the investigation of photocurrent production in a manner similar to Electrochemical Impedance Spectroscopy (EIS) [61]:

$$Q(\omega) = \frac{\widetilde{j_e}}{q\widetilde{\phi}} \tag{2.5}$$

This technique is known as Intensity Modulated Photocurrent Spectroscopy (IMPS). In this work, we employ an advanced variant of IMPS, called Controlled Intensity Modulated Photocurrent Spectroscopy (CIMPS), where a feedback system ensures that the light perturbation in time follows a sinusoidal function of defined frequency. In this case, the output transfer function H is represented as the ratio of the extracted current and the power intensity and can be related to Q as follows:

$$Q = H \cdot \frac{hc}{q\lambda} \tag{2.6}$$

where h is Planck constant, c is the speed of light, q is the elementary charge and λ is the wavelength of the light source [61]. Ponomarev and Peter [74] established a model which allows us to extract

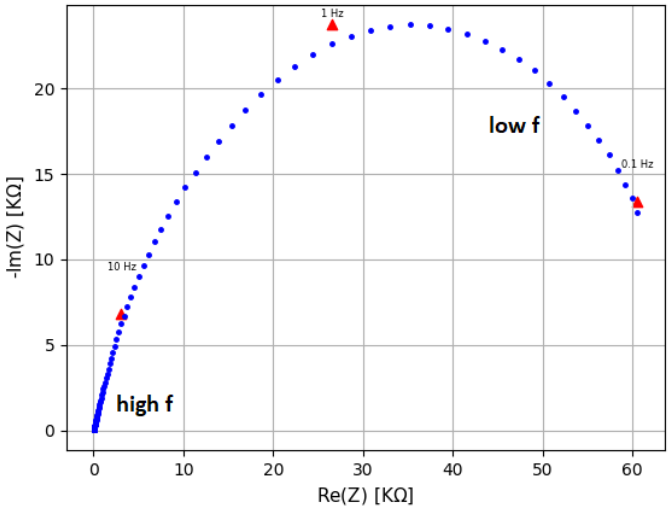

Figure 2.11: An example of Nyquist plot, where the points with the highest frequency are on the left side. Data refers to the sample with 45 nm Fe deposited, annealed in air for 2 hours at 600°C.

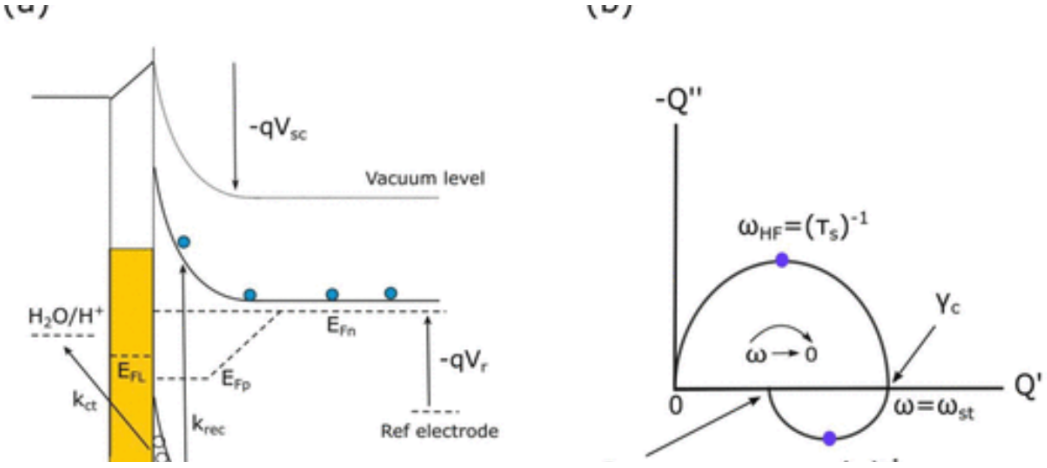

Figure 2.12: Scheme of the charge transfer processes occurring at a planar semiconductor-electrolyte interface, proposed by Peter et al. The two main processes of charge transfer of holes and recombination in the conduction band are indicated by their constant rate (left). IMPS response spectrum displayed in a Nyquist plot that is expected and described by Peter's model [61].

Figure 2.13: Front (left) and backside (right) of the photoelectrochemical cell used in this work. The coiled Pt wire can be seen in the former.

from the IMPS response some relevant information about the charge processes which occur at the semiconductor-electrolyte interface. A picture of this model is illustrated in Fig. 2.12. It delineates the interplay between minority carrier transfer from the semiconductor to the electrolyte at their interface, occurring at a characteristic rate denoted as k_{ct}, and recombination with electrons in the conduction band at the semiconductor interface, which occurs at a characteristic rate labelled as k_{rec}. The IMPS transfer function was derived by considering a basic charge compensation between the space charge capacitance and the Helmholtz capacitance on the electrolyte side at the interface. In this way, an analytical expression can be found:

$$Q(\omega) = Q_{ste}\frac{1 + j\gamma\omega\tau_{ct}}{(1 + j\omega\tau_s)(1 + j\omega\tau_t)} \tag{2.7}$$

where several parameters are introduced, and they will be explained in the following. q_{ste} is defined as the ratio of the charge transfer constant rate k_{ct} and the sum of both constant rates, whereas γ is a ratio which involves the space charge and the Helmholtz capacitances. The characteristic times which appear in the formula are linked to the model in the following way: τ_s is the product of the total capacitance, i.e. the connection in series of the space charge and the Helmholtz capacitance; τ_{ct} is the characteristic time of charge transfer of holes into solution and lastly τ_t is the inverse of the sum of the two constant rates k_{ct} and k_{rec}. The IMPS transfer function described by Eq. (2.7) can be plotted in a Nyquist plot and gives the shape shown in Fig. 2.12(right). One arc is in the negative high-frequency quadrant, and one arc is in the positive low-frequency quadrant, which reaches its maximum at τ_t^{-1}. From the latter and the value of the low-frequency intercept in the real axis, which corresponds to Q_{ste}, the constant rates can be extrapolated. Another important quantity is the External Quantum Efficiecy (EQE), which is a measure of how effectively a photovoltaic device converts incident photons into electrical current. It is defined as the ratio of the number of charge carriers collected to the number of incident photons. Its derivative respect to the incident photon flux ϕ is called the differential external quantum efficiency ($EQE_{PV,diff}$) which appears as a first-order factor in the Taylor expansion of the extracted current respect to ϕ. Its relation with the IMPS transfer function is that it is equal to the real part of Q at the lowest frequency. So, given an IMPS spectrum, the two constant rates and the differential external quantum efficiency can be simply calculated.

The experimental setup required for the type of techniques described so on, primarily consists of four elements: the photoelectrochemical (PEC) cell, the potentiostat, the frequency response analyzer (FRA), and the light source. The first one is the device where the electrochemical reaction takes place, for which a general overview has been provided in Section 1.2. In this work, the cell was constructed in Teflon at the mechanical workshop of the Physics and Astronomy Department, and as shown in Fig. 2.13, it has two openings on its two lateral faces. One allows the light to enter and illuminate the sample from the front and is covered with a quartz plate. The other side is where the sample is

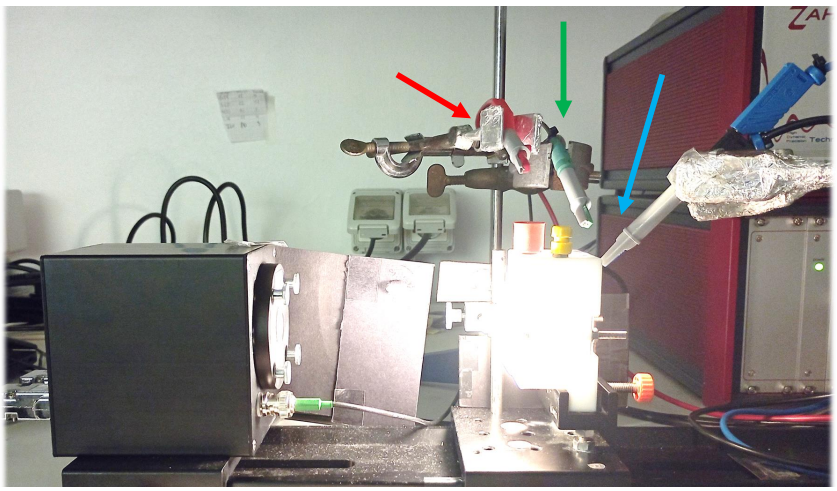

Figure 2.14: Photo of the setup in working condition. The sample is not mounted. The counter, reference and working leads are respectively indicated with red, green and blue arrows.

positioned, and it is pressed with an O-ring and a plexiglass plate. The sample area exposed to the solution is 0.1979 cm^2. The cell is connected to the potentiostat in a three-electrode and four-terminal configuration, which consists of the working electrode (WE), the counter electrode (CE) and the reference electrode (RE), as illustrated in Fig. 2.14. The photoanode being investigated serves as the working electrode, where the oxidation reaction occurs under a desired potential difference compared to the stable potential of the reference electrode. The potentiostat assesses the potential difference between the working and reference electrodes and rectifies any deviations from the desired value by enabling current flow between the working and counter electrodes. Measuring the semiconductor's potential with respect to the one of a reference electrode V_{Ref} offers the advantage of maintaining the measured potential difference independent of the current passing through the cell. In contrast, the potential difference between the semiconductor and the metal counter electrode depends on V_H at the metal electrode, which fluctuates unpredictably with the current, as previously discussed in Section 1.2. The measured potential V can be converted in the usual RHE scale with the following equation, based on the Nernst equation:

$$V(RHE) = E^0 + V_{Ref} + 0.054 \cdot pH \tag{2.8}$$

where E^0 is the standard potential of the reference electrode. The working sense lead is sorted to the WE and is used to more accurately measure the applied voltage to the electrochemical cell. The contact for the working electrode is created by attaching a small piece of copper foil with a strip of Teflon tape onto a narrow region of the glass-FTO substrate, where iron has intentionally not been deposited. The contact is securely maintained by the pressure exerted by the plexiglass piece that secures the sample in place on the O-ring. Fig. 2.15 provides a schematic representation of the potentiostat. The signal generator generates the desired signal waveform (for example, a constant value or a sine wave) and transmits it to the control amplifier. The control amplifier applies this signal waveform to the cell and adjusts its magnitude to match the user's input value. The applied signal can be either a voltage (in potentiostatic mode) or current (in galvanostatic mode). The potential difference between the Reference and Working Sense electrodes is measured by the electrometer. Furthermore, the measured voltage signal is sent back to the control amplifier, where it is compared to the desired voltage value. If a deviation is detected, the control amplifier modifies its output signal to counteract the initial perturbation. The current passing through the cell is quantified using the current-to-voltage converter (I/V Converter). To achieve this, the current signal is converted into a voltage signal. This conversion is accomplished using a resistor (R_m) within the I/V converter. The voltage drop measured across the resistor is directly proportional to the current flow through the cell.

The potentiostat is linked to a frequency response analyzer (FRA), which guarantees the application of a sine-wave perturbation signal to the cell and the subsequent analysis of the response, decomposing it into its real and imaginary components. As depicted in Fig. 2.16(left), the FRA can calculate the

impedance of the examined cell by comparing the sinusoidal response $I(t)$ with two synchronized reference signals: one that is in-phase ($\sin \omega t$) and another that is phase-shifted by 90 degrees ($\cos \omega t$) with respect to the sinusoidal voltage perturbation. In particular, the generator generates a sinusoidal voltage excitation signal at a specific frequency, $V \sin \omega t$, which is simultaneously applied to the cell and the real part correlator. This perturbation is superimposed onto a DC voltage signal V_0, directed to the cell through the potentiostat. The generator also produces a second waveform, which is phase-shifted by 90 degrees relative to the excitation waveform and is directed to the imaginary part correlator. Both correlators process the cell response $I(t)$ by multiplying it with the generated waveform. The resulting signals are then directed to integrators, effectively eliminating all harmonic responses except for the fundamental frequency, allowing for the calculation of both the real and imaginary components of the impedance. This process can be iterated at different frequencies, with the number of periods over which integration occurs varying accordingly. Lastly, the light source illuminates the sample from the front, and its intensity is regulated by a photodiode and a feedback system. This setup also enables the modulation of intensity in a way that allows for the application of a small perturbation at a specific frequency.

In this study, all measurements were conducted using Ag/AgCl or Hg/HgO reference electrodes, a 1 M KOH (pH = 14.25) electrolyte, and the combined FRA-potentiostat Zahner Zennium Pro. Additionally, the Zahner XPOT/211 module and the Thorlabs photodiode were employed for light measurements, along with a Zahner LSW-125 mW/cm^2 white LED as the light source. As shown in Fig. 2.16(right), the dominant wavelength of the LED is around 600 nm (615 nm, to be precise). EIS/PEIS measurements were performed with a 5 mV amplitude perturbation, in a frequency range from 50 mHz to 10^5 Hz, and typically with a DC voltage scan from 1.08 to 1.63 V vs RHE. CIMPS measurements utilize a 10% light intensity modulation, a frequency range from 100 mHz to 10^4 Hz, and a DC voltage scan from 1.08 to 1.88 V vs RHE. In order to ensure the stability of the system, the first potential at which EIS/PEIS/CIMPS is initially performed is repeated after the sequence. The measurement procedure begins with the setup connection. Initial impedance checks are performed in the dark to ensure optimal electrical contacts, followed by monitoring the open-circuit potential (OCP) as it reaches equilibrium. The system is then conditioned through repeated cycles of I-V measurements to verify electrode stability and eliminate impurities. Subsequently, I-V measurements are conducted both in the dark and under illumination, spanning the potential range of V = 0.9-1.9. Optional impedance measurements may also be included to provide a thorough characterization of the system. This comprehensive protocol ensures reliable data collection and a comprehensive understanding of the photoelectrochemical system's behaviour.

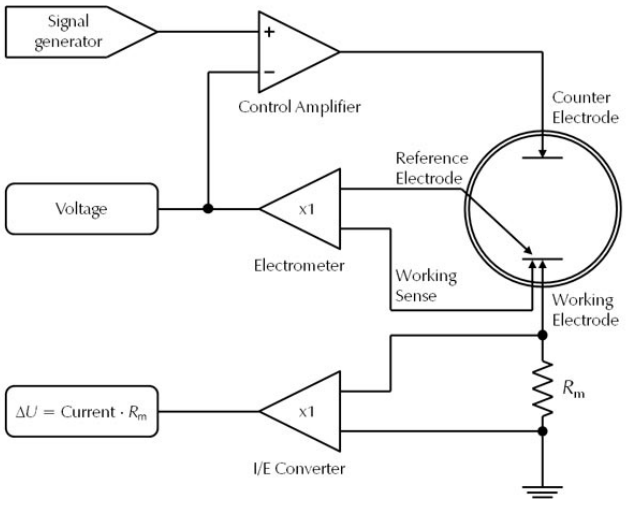

Figure 2.15: Schematic electrical circuit representation of the potentiostat [38].

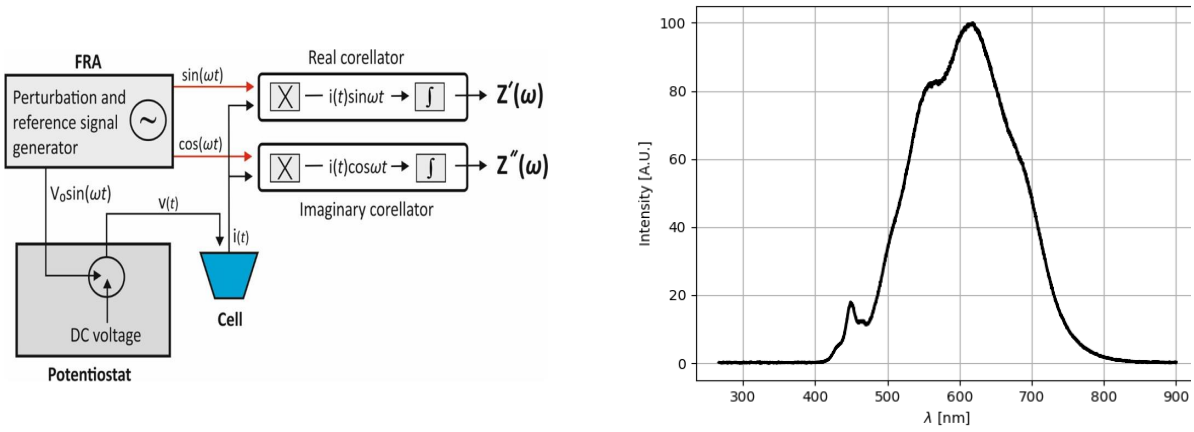

Figure 2.16: A scheme of the frequency response analyzer (FRA) [40] (left). The intensity spectrum of the Zahner LSW-1 white LED used in this work. It can be noted that it is centred at around 615 nm.

2.8 Synthesis of nanostructured thin films

The samples are prepared using soda lime glass coated with FTO (Fluorine-doped Tin Oxide) substrates with dimensions of 20x15 mm, a thickness of 2.2 mm, and a nominal resistance of 8 Ωcm^2 (TEC 8, Ossyla). The choice of this substrate is due to its ease of electrode contact during PEC measurements and, from a future perspective, the possibility of backlight illumination, thus avoiding the passage of light through the solution. The substrates undergo a cleaning procedure, which involves sonicating them for 10 minutes each in three different solvents, namely acetone, ethanol, and isopropanol. They are air-dried and then placed in the deposition chamber to deposit the Fe film via magnetron sputtering. The thickness of the film deposited is monitored by measuring a reference using Atomic Force Microscopy (AFM). Following the film deposition, thermal annealing is employed to modify structural, electrical, and optical properties through heat treatment. This process commonly induces phase transformations, enhances specific properties, initiates oxidation or reduction reactions, mitigates defects, and activates dopants. During annealing in a reactive atmosphere, various forces and processes come into play. Firstly, atoms in the thin film move and diffuse through the material due to the supplied thermal energy. These atoms can participate in nucleation and growth processes, eventually leading to the formation of nanostructures. Finally, the atoms from the gas present in the annealing chamber can promote oxidation or reduction reactions, depending on the material composition and the gases present. The annealing process can be controlled through various parameters, including temperature, pressure, atmosphere, and time. This synthesis procedure is less commonly used compared to the solution-based colloidal method described by Vayssieres [22], but it offers the advantage of producing more robust structures and providing better control over synthesis parameters [17]. Among the samples prepared during the experimental campaign from March to August, this thesis focuses on a limited number of samples, which, for convenience, can be divided into three sets, as illustrated in Table 2.1.

Set name	Sample name			
A	45nm 2h 480°C	45nm 2h 550°C	45nm 2h 600°C	45nm 2h 650°C
B	120nm 2h 600°C	220nm 2h 600°C	120nm 2h 650°C	220nm 2h 650°C
C	250nm 24h 350°C	250nm 24h 350°C,3h 600°C	60nm Fe-Sn 1.3%	60nm Fe-Sn 3%

Table 2.1: Samples studied in the thesis divided into three sets: 'A', 'B' and 'C'. The name of samples refers to the principal parameter of investigation, film thickness deposited and temperature annealing. If not specified, the material deposited is iron.

The first set, identified by the name 'A', pertains to the samples in which 45 nm of iron film was

deposited and thermally treated in air with increasing temperature from 480°C to 650°C. The second set, labelled with the letter 'B', includes four samples with a greater thickness compared to the previous set, annealed at temperatures of 600°C or 650°C. The primary focus of the thesis is on these first two sets. Finally, there is a third set, labelled with the letter 'C', which includes four additional samples used for some comparisons. The samples are named according to the parameters under study in the thesis. Where not specified, the deposited material is Fe.

Chapter 3

Experimental results: thin film characterization

In this chapter, the morphological, optical, compositional, and crystalline order properties of the samples studied in the thesis are discussed. Specifically, an example of a nanostructure is presented, created with a 250 nm thick deposited Fe layer and annealed at low temperature for an extended period (24 h). Subsequently, attention is directed towards the characterization of these properties for two series of samples. In one series, the annealing temperature varies, while in the other, the thickness of the deposited Fe film is altered.

3.1 Formation of Fe_2O_3 nanowhiskers

Nanostructuring has emerged as a key approach to address the optoelectronic limitations of hematite, as initially demonstrated with cauliflower-like nanostructures [44]. In the initial phase of the experimental campaign, the focus was on creating a nanowire array. Vertically aligned nanowires demonstrated exceptional performance, offering significant advantages, such as a substantially increased electrode surface area, crucial for driving the photoelectrochemical charge transfer [45]. Additionally, photo-generated charge carriers only need to travel a short distance, typically just a few nanometers, to reach the surface. This surface can be further customized to reduce surface recombination rates or facilitate the transfer of charge carriers to the electrolyte. Another notable benefit of employing a nanowire array strategy is efficient light trapping, as nanowire arrays lack a well-defined interface but rather exhibit a gradual change in the air-material ratio, leading to a gradual change in refractive index [42]. This, in turn, naturally reduces surface reflectivity and promotes effective light absorption along the nanowire axis, typically a few microns in length. Enhanced light trapping in nanowire arrays has been demonstrated through 3D simulations [46]. In literature, the use of $\alpha - Fe_2O_3$ nanowire arrays has been discussed, with specifications indicating nanowire diameters of 5—10 nm to support efficient hole transport to the surface and a nanowire length of at least 400—500 nm to ensure complete light absorption within the array [45]. In the context of commercial applications, it is essential that the synthesis of nanowires or nanostructures is both cost-effective and reproducible on a large scale. Currently, only a limited number of bottom-up techniques are available for this purpose, including (i) solution-based hydrothermal synthesis, (ii) electrodeposition, and (iii) thermal oxidation of iron [42]. The last approach is followed by this work, using long low-temperature annealing conditions in ambient air to promote the diffusion of iron cations out the surface. In particular, the formation of Fe_2O_3 nanowhiskers occurs during specific oxidizing thermal treatments, in which, together with oxygen diffusion in the film, there is a spatially non-homogeneous iron out-diffusion and oxidation. The in-homogeneity is likely related to the formation of fast diffusion channels for Fe, favoured by defects. The driving force for the iron out-diffusion is a gradient of cation vacancy [43]. An example of the nanostructured thin films obtained with this approach is shown in the SEM images (top view) of Fig. 3.1. The film is obtained by thermal annealing in air at 350°C of a metallic Fe film, 250 nm

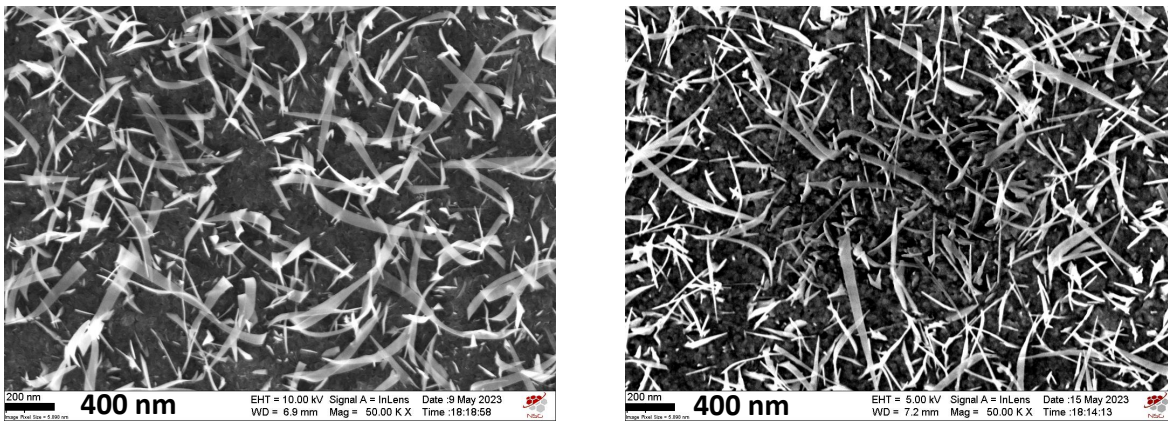

Figure 3.1: SEM images (top view) of 250 nm Fe deposited on FTO annealed in air for 24 hours at 350°C (left) and after an additional 3 hours of annealing treatment at 600°C(right).

thick, deposited by PVD (Fig. 3.1 left). Thin nanowhiskers are visible, grown perpendicularly to the surface, with a very high aspect ratio. The length of the longest ones is more than 1 μm, and the size in the two directions perpendicular to the whisker axis are about 100 nm and less than 10 nm. In Fig. 3.1 (right), the same nanostructured film has been further annealed at 600°C in air (3h) to improve the crystallinity. The morphology is maintained. The corresponding GIXRD patterns for the two cases are shown in Fig. 3.2.

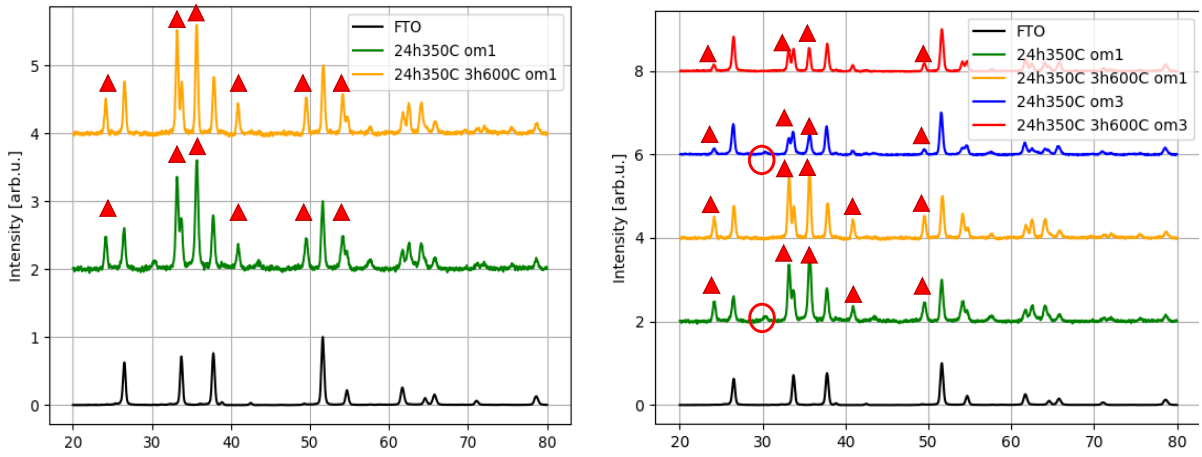

Figure 3.2: (left) GIXRD spectra at ω=1° of FTO substrate (black) and 250 nm Fe deposited on FTO, annealed in air for 24 hours at 350°C (green) and after an additional 3 hours heat treatment at 600°C (yellow). (right) GIXRD spectra comparison of the same samples at different ω (1°, 3°). With red markers hematite peaks are labelled, instead the magnetite peak at 30.1° is highlighted with a circle.

The analysis was performed using the free software MAUD. Relevant phases were input, and lattice parameters and grain size values were determined for each phase. Two expected phases were hematite and FTO. Hematite possesses the corundum structure, which is trigonal (hexagonal scalenohedral) with symbol 3 2/m, space group R3c, and lattice parameters a = 5.0356 Å and c = 13.7489 Å, with six formula units per unit cell [3]. FTO was considered as SnO_2 and has a tetragonal structure with space group $P4_2/mnm$ and lattice constants a = 4.737 Å and c = 3.185 Å, with two formula units per unit cell.

In addition to hematite peaks (at 2θ = 24.1° (012), at 33.1° (104), at 35.6° (110), at 40.9°(113), at 49.5°(024) and at 54.1°(116)) and FTO peaks (at 2θ = 26.5° (110), at 33.7°(101), at 37.8°(200) and

Table 3.1: GIXRD results for the nanowhiskers layer on FTO.

Sample name	Fe_2O_3			FTO		
	a(Å)	c(Å)	size (nm)	a(Å)	c(Å)	size (nm)
24h 350°C ω =1°	5.031(5)	13.745(5)	52(5)	4.757(5)	3.197(5)	62(5)
24h 350°C 3h 600°C ω =1°	5.034(5)	13.739(5)	98(5)	4.748(5)	3.194(5)	80(5)
24h 350°C ω =3°	5.036(5)	13.752(5)	52(5)	4.761(5)	3.200(5)	64(5)
24h 350°C 3h 600°C ω =3°	5.038(5)	13.751(5)	98(5)	4.754(5)	3.198(5)	73(5)
Fe_2O_3 [47]	5.036(1)	13.749(1)				
FTO [48]				4.737(1)	3.185(1)	
FTO				4.754(5)	3.198(5)	

at 51.6°(211)), the film annealed at 350°C also exhibits a peak at $2\theta = 30.1°$, which disappears after the second thermal treatment. This peak was identified as (220) peak of Fe_3O_4. This observation is attributed to the fact that 350°C represents the minimum temperature at which iron oxides transform into the most stable thermodynamic phase, which is indeed hematite [3], so some traces of magnetite are plausible. The analysis results, as presented in Table 3.1, indicate that the lattice parameters remain unchanged for both hematite and FTO. These values are consistent with those found for bare FTO (a = 4.754(5) Å, c = 3.1984(5) Å, and a grain size of 77(2) nm). The second annealing process primarily affects the grain dimensions of both phases, suggesting that higher temperatures can improve the crystalline order. In terms of photoelectrochemical (PEC) performance, this could result in a reduced concentration of recombination centres. Furthermore, results obtained at a larger angle of incidence (ω), corresponding to a longer penetration depth (470 nm vs 150 nm, for bulk Fe_2O_3 [49]), are also included in Table 3.1. Notably, there are no significant variations, indicating the sample's uniform composition and average crystalline grain size.

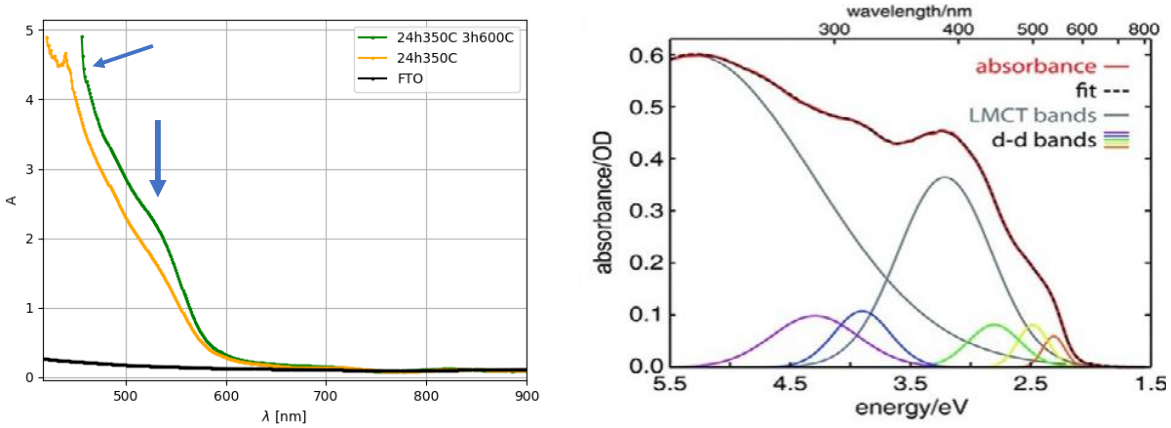

Figure 3.3: UV-Vis absorbance spectra of samples with 250 nm Fe deposited on FTO, annealed in air for 24 hours at 350°C (green) and after an additional 3 hours thermal treatment at 600°C (yellow). The spectrum of bare FTO is also plotted in grey (left). Theoretical absorption spectrum of hematite with the underlying contributions [56](right).

The corresponding optical absorption spectra for the two samples are reported in Fig. 3.3(left), where they are compared to the absorption spectrum for bare FTO. The spectra exhibit the typical feature of Fe_2O_3, notably two significant bands around 565 nm and 400 nm. In the literature, the low energy portion of the absorption spectrum has been attributed to Fe d-d transitions, while the higher energy features in the spectra, particularly those around 390 400 nm, are believed to be the result of O_{2p}-Fe_{3d} ligand to metal charge transfer (LMCT) excitations [51]. A theoretical spectrum for comparison is shown in Fig. 3.3(right). The main difference induced by the high-temperature process is a slight increase in the absorbance. This can be due to a larger fraction of Fe_2O_3 being formed during the 600°C-annealing, even if an increase in extinction could be related to an increased scattering from

the nanostructures. The energy gap can be estimated from the Tauc plots [52]. Considering that the

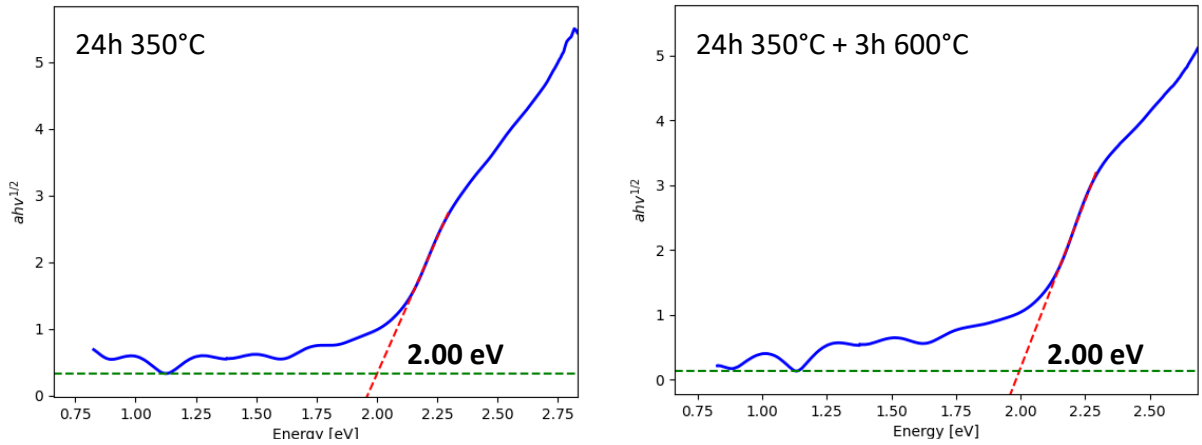

Figure 3.4: Tauc plots of specimens with 250 nm Fe deposited on FTO, annealed in air for 24 hours at 350°C (left) and after an additional 3 hours of heat treatment at 600°C (right). The E_{gap} was calculated as the intersection between the red line, which fits the sloping part, and the green line, which represents the baseline.

hematite is an indirect semiconductor, the energy gap can be found by plotting the value of $(\alpha h\nu)^{\frac{1}{2}}$ versus the photon energy and extrapolating to zero absorbance the linear behaviour obtained. The results are shown in Fig. 3.4. It has to be noted that here, since a scattering contribution to the measured extinction coefficient has to be taken into account, the E_{gap} is estimated by extrapolating the linear behaviour to the value of flat absorbance. The estimated energy gap values are XX eV and XX eV for the sample annealed for 24 hours at 350°C and for the one with the additional 3 hours at 600°C thermal treatment. The agreement with the 1.98 eV value found in literature is good [53].

3.2 Effect of different annealing temperature

Here, the effect of air annealing at different temperatures is discussed. It has to be considered that the thermal stability of the FTO substrate is limited to T<550°C. For higher annealing temperatures, the Sn^{4+} ions diffuse on the iron oxide layer. This has a beneficial effect on the Fe_2O_3 electronic conductivity. Indeed, the replacement of Fe^{3+} with Sn^{4+} can lead to a higher concentration of donors, leading to an increased electronic conductivity. On the other hand, the Sn doping profile on Fe_2O_3 is not completely predictable since it also depends on the nanocrystalline nature of the deposited film, which in turn also depends on the annealing conditions. To simplify the study, we have decided to focus on one (small) Fe thickness (45 nm), which is expected to be thick enough to fully cover the underneath substrate. At the same time, once the Sn diffusion starts, the thinner the film is, the smaller the Sn concentration gradient in it will be.

The morphology of the samples with 45 nm of iron deposited on FTO and heated at increasing temperatures from 480°C to 650°C remains consistent. As seen in the SEM images shown in Fig. 3.5, the substrate grains are clearly visible. Here, the nanowhiskers do not form. This is mainly due to the fact that fast iron oxidation, due to both a relatively high temperature and a low film thickness, does not allow the out-diffusion of Fe ions, which is normally triggered by a gradient of cation vacancy [43]. This fact allows us to consider separately the effect of Fe_2O_3 nanowhiskers, obtained in thick films, and of the Sn-doping, dominant in thin films, especially in the photoelectrochemical properties, Observing the GIXRD spectra, as shown in Fig. 3.6, only two phases are visible: Fe_2O_3 and FTO. For the former, peaks at 33.1°(104), 35.6° (110) and 54.1°(116) are observed, while for the latter, peaks at 26.5° (110), 33.7° (101), 37.8° (200) and 51.6° (211) are evident. At T = 650°C, some peaks around (104) and (110) for Fe_2O_3 are noticeable; however, they likely belong to the underlying FTO. This is probably due to the X-ray beam hitting the region intentionally left without deposition for electrical contact.

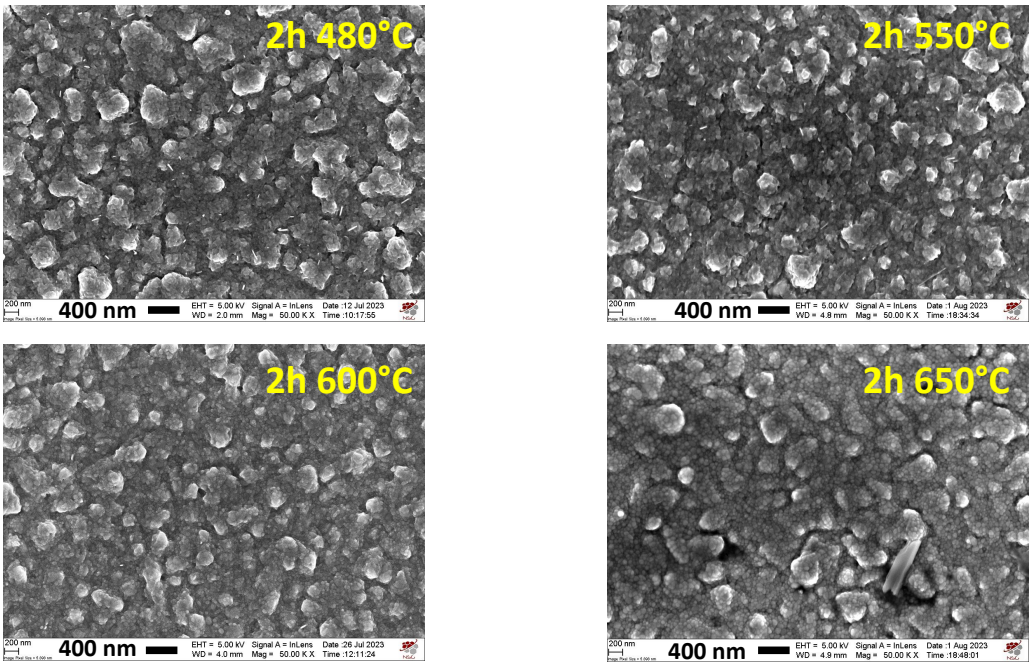

Figure 3.5: SEM images of 45 nm Fe deposited samples annealed in air at different annealing temperatures for 2 hours.

Notably, there are no distortions in the cell parameters, as listed in Table 3.2. The grain size also remains relatively constant, except for the sample heated to 650°C, where it is smaller for both phases. Considering that the thickness of the oxidized film about double with respect to the metallic one (the Fe atomic concentration in the bcc αFe is $8.49 \cdot 10^{22}$ atoms/cm^3, in the α-Fe_2O_3 is $3.80 \cdot 10^{22}$ atoms/cm^3), the crystalline grain size of the hematite phase is about half of the whole film thickness. The same samples were also analyzed using Raman spectroscopy. The experimental data are illustrated in Fig. 3.7 in comparison to spectra taken from literature of known phase [54]. The expected peaks for hematite are clearly visible, including the two A_{1g} modes at 225 and 498 cm^{-1}, as well as four of the five E_g modes (247, 293, 299, 412, 613 cm^{-1}) [54]. Additionally, the two-phonon scattering band is observed at 1319 cm^{-1}. In the inset, it can be seen that the sample heated to 480°C shows a peak (at 662 cm^{-1}) that is normally attributed to the magnetite (Fe_3O_4) phase [54]. This could be due to the not complete phase transformation at this relatively low temperature. The fact that the Fe_3O_4 is not detected in the GIXRD patterns (Fig. 3.6) suggests that it is a highly disordered phase that is completely transformed into Fe_2O_3 at high-temperature. The absorption spectra exhibit the same characteristics for all samples, notably two significant bands around 565 nm and 400 nm (see Fig. 3.8), already seen and discussed in Section 3.1. The temperature effect results in an increase in absorbance and, consequently, a reduction of approximately 7% in the penetration depth (a rough

Table 3.2: Results of the GIXRD analysis on 45 nm Fe film deposited on FTO, annealed in air for 2 hours at different temperature.

Sample name	Fe_2O_3			FTO		
	a(Å)	c(Å)	size (nm)	a(Å)	c(Å)	size (nm)
2h 480°C	5.038(5)	13.752(5)	52(5)	4.756(5)	3.199(5)	74(5)
2h 550°C	5.036(5)	13.754(5)	54(5)	4.754(5)	3.199(5)	72(5)
2h 600°C	5.036(5)	13.745(5)	52(5)	4.745(5)	3.196(5)	76(5)
2h 650°C	5.040(5)	13.759(5)	42(5)	4.751(5)	3.198(5)	69(5)
Fe_2O_3 [47]	5.036(1)	13.749(1)				
FTO [48]				4.737(1)	3.185(1)	
FTO				4.754(5)	3.198(5)	

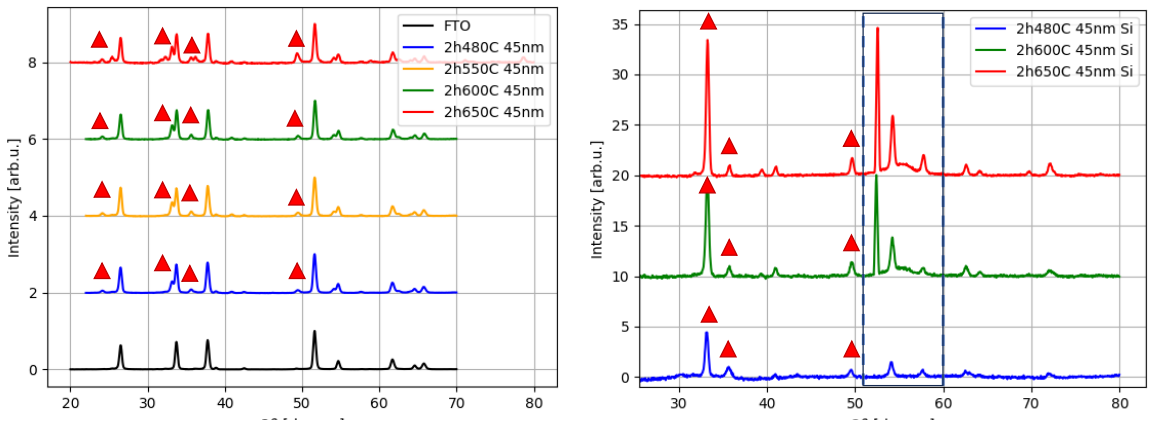

Figure 3.6: GIXRD spectra of 45 nm Fe on FTO samples with varied temperature annealing, distinguished by colour. Bare FTO is also shown in black (left). GIXRD spectra of specimens with 45 nm Fe deposited on Si substrate and after annealed at varied temperature, distinguished by colour. The region in the rectangular area regards the Si signal. Red markers label hematite peaks.(right)

Table 3.3: Results of the GIXRD analysis on 45 nm Fe film deposited on Si, annealed in air for 2 hours at different temperatures.

Sample name	Fe_2O_3		
	a(Å)	c(Å)	size (nm)
2h 480°C	5.032(5)	13.753(5)	46(5)
2h 600°C	5.025(5)	13.723(5)	55(5)
2h 650°C	5.023(5)	13.718(5)	72(5)

estimate, at $\lambda = 550$ nm, is 75 nm for the samples heated to 480°C and 550°C and 70 nm for the sample heated to 650°C). The increase of the absorbance at T>480°C is consistent with a larger fraction of crystalline hematite, in agreement with the Raman results. Furthermore, an estimation of the energy gap was performed, as previously discussed in Section 3.1. The Tauc plots for these systems (Fig. 3.9) show an increase of the energy gap increasing annealing temperature from 480°C to 550°C, which can be explained by a greater degree of structural order. The energy gap values found in order of annealing temperature are:1.95(3) eV, 2.02(1), 2.03(1). Except for the first value, the results are in agreement with 1.98 eV found in literature [53]. It is worth noting that changing the substrate has a more pronounced effect at higher temperatures. Table 3.3 presents the GIXRD analysis results for samples with Fe films deposited on Si (the sample with an annealing temperature equal to 550°C is not available). As temperature increases, grain size expands, and there is a significant reduction in cell parameters.

So, the Raman scattering and UV-Vis spectra suggest that the effect of air annealing at increasing temperature on a 45 nm thick Fe, in the range 480-650°C is to increase the Fe_2O_3 crystalline fraction, likely improving the film crystallinity. The corresponding crystalline size does not vary significantly upon annealing in this temperature range. By the way, the same Fe deposition was performed on Si substrates, and the obtained samples have been analysed by GIXRD, obtaining the results reported in Table 3.3. Iron is still in the hematite phase, as for the FTO substrate. Nevertheless, while upon 480°C annealing, the lattice parameters and crystal size are consistent with the results obtained for the films deposited on FTO substrates, the annealing at a higher temperature on the film deposited on Si lead to a slightly shorter lattice parameter and to an increased crystalline grain size. An increase in the grain size is expected due to the increased diffusion (as already observed, see Table 3.2). Different reasons could be given for this substrate-dependent behaviour. With an inert substrate, it is expected that the hematite nanocrystals grow as the annealing temperature is increased, as observed in the

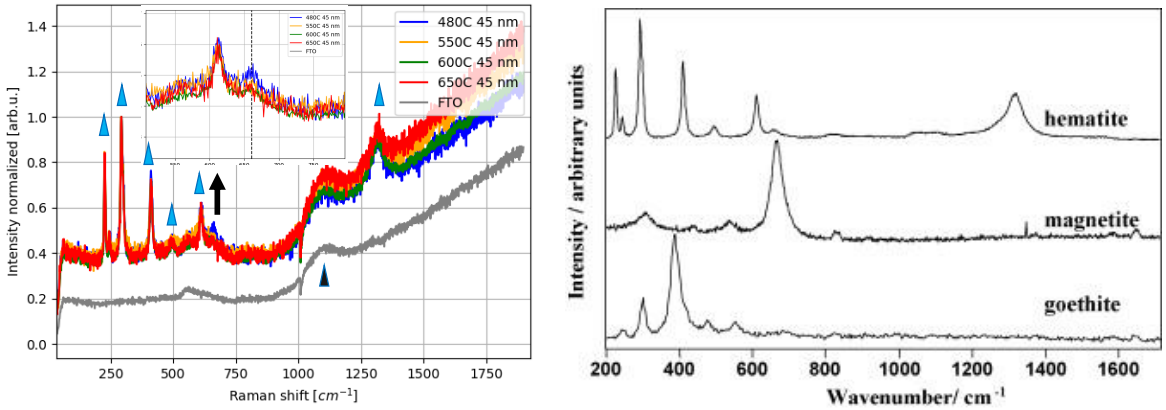

Figure 3.7: Raman spectra of iron oxide photoanodes with 45 nm Fe deposited on FTO, annealed in air for 2 hours at increasing annealing temperature. The spectrum of bare FTO is also plotted in grey. The zoom around $660cm^{-1}$ gives a look of a probable magnetite trace. Blue markers highlighted the hematite peaks (left). Theoretical Raman spectrum of iron oxides, hematite and magnetite in particular [54](right)

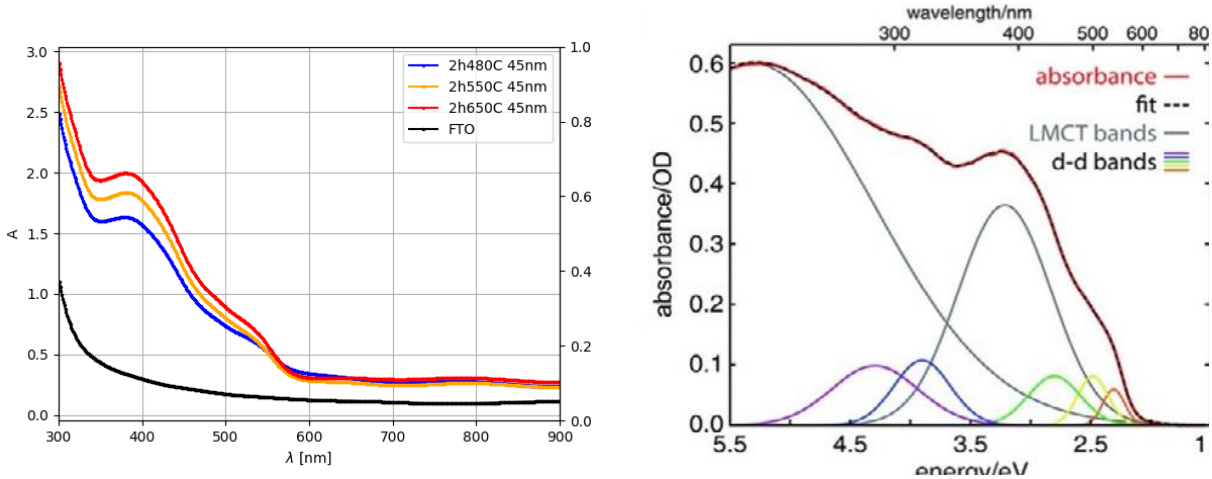

Figure 3.8: UV-Vis absorbance spectra of specimens with 45 nm Fe deposited on FTO, annealed in air for 2 hours at an increasing annealing temperature. The spectrum of bare FTO is also plotted in grey (left). Theoretical absorption spectrum of hematite with the underlying contributes [56](right).

case of the Si substrate. The fact that Si is a flat substrate with a low thermal expansion coefficient ($2.5 \cdot 10^{-6}\mathrm{K}^{-1}$) with respect to the Fe_2O_3 one (about $10^{-6}\mathrm{K}^{-1}$) can lead to the observed compressed Fe_2O_3 structure. When the glass-FTO substrate is used, although the thermal expansion coefficient of FTO is just $3.6 \cdot 10^{-6}\mathrm{K}^{-1}$ [57], high substrate roughness (about 30 nm, i.e., comparable to the film thickness) can help to relax the film structure. Further investigation is needed to assess this point. In particular, XPS analysis is foreseen to possibly detect Sn atoms at the film surface.

3.3 Effect of different film thickness

From a morphological perspective, when increasing the initial thickness of the iron film, from 45 nm to 120 nm and 220 nm, SEM images (Fig. 3.10, first row) reveal the formation of iron oxide nanowhiskers. Their surface density is lower when compared to samples with long annealing at low temperatures (see Fig. 3.1). A constant presence of small grains at the base is also visible. In this case, a 600°C and 650°C annealing was considered since it is the one for which the most promising photoelectrochemical properties are recorded (see Section 4.1.1). Even when changing the substrate from FTO to Si, the

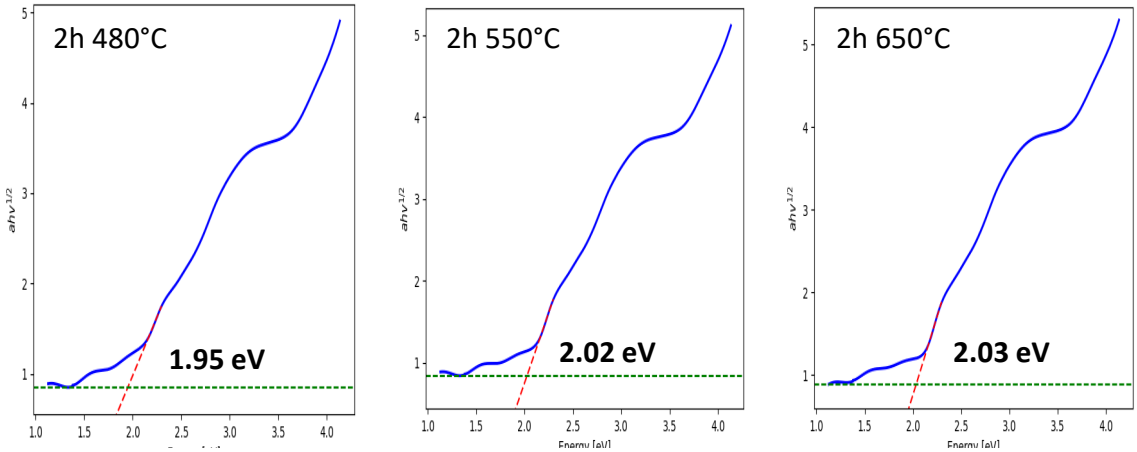

Figure 3.9: Tauc plots of specimens with 45 nm Fe deposited on FTO, annealed in air for 2 hours at increasing annealing temperature. The E_{gap} was calculated as the intersection between the red line, which fits the sloping part, and the green line, which represents the baseline.

trend remains consistent (Fig. 3.10, second row). This can be explained by the fact that at greater thicknesses, there is more material available, and a gradient of iron cation density can be established in the thickness direction, while the rarity of the structures is attributed to the fact that at such high temperatures, the balance between oxygen entering and iron cations leaving is skewed towards the former.

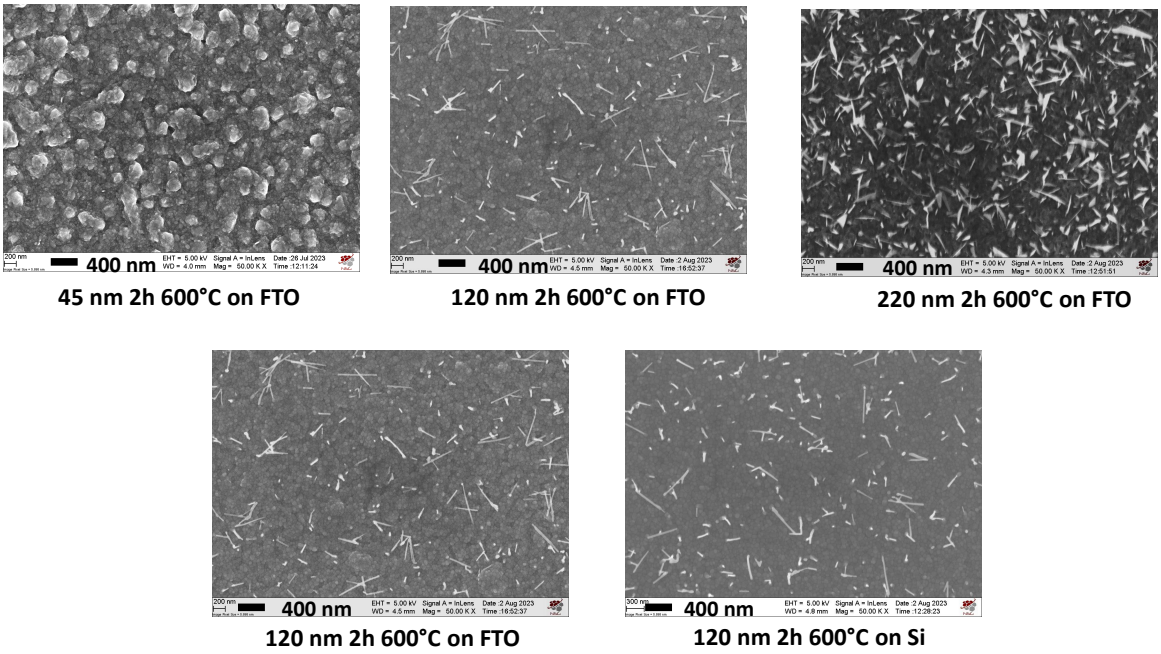

Figure 3.10: In the first row, SEM images (top view) of iron oxide samples with different thickness film deposited on FTO at constant annealing temperature (T= 600°C). In the second row, a comparison of samples with the same annealing temperature ($T = 600$°C) and thickness of the film deposited (120 nm), but different substrates (FTO and Si).

The GIXRD spectra, shown in Fig. 3.11, clearly show that the signal from hematite is higher for thicker iron oxide film, as it should be. Moreover, the grain size of Fe_2O_3 changes, as shown in Table 3.4, which presents the results of the analyses conducted using the MAUD software. Subsequently, investigations were carried out at higher incident angles ($\omega = 3°$), resulting in greater penetration depths (470 vs 150 nm), for samples with 220 nm of deposited Fe heated at 600°C and 650°C. As depicted in Table 3.4,

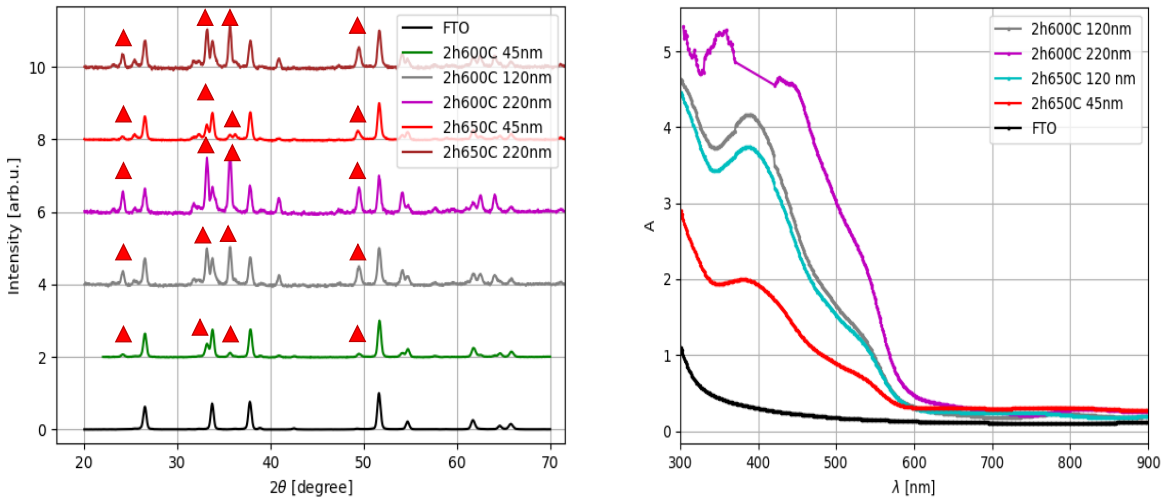

Figure 3.11: GIXRD spectra of iron oxide photoanodes realized on FTO with different thicknesses of Fe deposited (left). A bare FTO spectrum is plotted too, and red markers label hematite peaks. UV-Vis absorption spectra of the same samples with comparison to a thinner one realized with similar annealing temperature (right).

Table 3.4: GIXRD analysis results of Fe samples on FTO annealed in the air for 2 hours at 600°C and 650°C with different film thicknesses deposited. When not specified $\omega = 1°$.

Sample name	Fe_2O_3			FTO		
	a(Å)	c(Å)	size (nm)	a(Å)	c(Å)	size (nm)
45 nm 600°C	5.036(5)	13.745(5)	54(5)	4.745(5)	3.196(5)	76(5)
120 nm 600°C	5.036(5)	13.752(5)	72(3)	4.753(5)	3.194(5)	65(5)
220 nm 600°C	5.037(5)	13.749(5)	94(4)	4.755(5)	3.191(5)	71(5)
220 nm 600°C $\omega = 3°$	5.041(5)	13.764(5)	61(3)	4.759(5)	3.197(5)	69(5)
45 nm 650°C	5.040(5)	13.759(5)	42(2)	4.751(5)	3.198(5)	69(5)
220 nm 650°C	5.037(5)	13.753(5)	78(3)	4.752(5)	3.193(5)	69(5)
220 nm 650°C $\omega = 3°$	5.043(5)	13.771(5)	58(4)	4.758(5)	3.199(5)	71(5)

the grain size is not homogeneous. On the upper layer, the grains are larger, and the mild increase in the c-axis cell parameter of hematite in the underlying layers suggests a plausible stress in the entire structure, likely related to the formation of nanostructures. Increasing the thickness also has an impact on the optical properties of the film. As seen in Fig. 3.11(right), the absorption increases with greater thickness. In Table 3.5, the energy gap values found from Tauc plot analysis (Fig. 3.12) are reported. The agreement with the literature E_{gap} value of 1.98 eV [53] is good.

So, the GIXRD results show that while the lattice parameter a does not vary significantly neither with the film thickness (45 nm-220 nm range) nor with the probed depth, a slight increase of the c parameter with the probed depth suggests a stress in the structure. Moreover, the crystal size increases with the film thickness, and larger nanocrystals are found closer to the film surface. From the UV-Vis, it can be stated that by varying the film thickness, the light-harvesting capability can be tuned, but the edge of absorption is not altered.

Table 3.5: Energy gap of iron oxide specimens realized with different iron thickness deposited on FTO and annealed at 600°C and 650°C.

Sample name	120 nm 600°C	220 nm 600°C	45 nm 650°C	120 nm 650°C
E_{gap} (eV)	2.02(1)	2.0181)	2.03(1)	2.01(1)

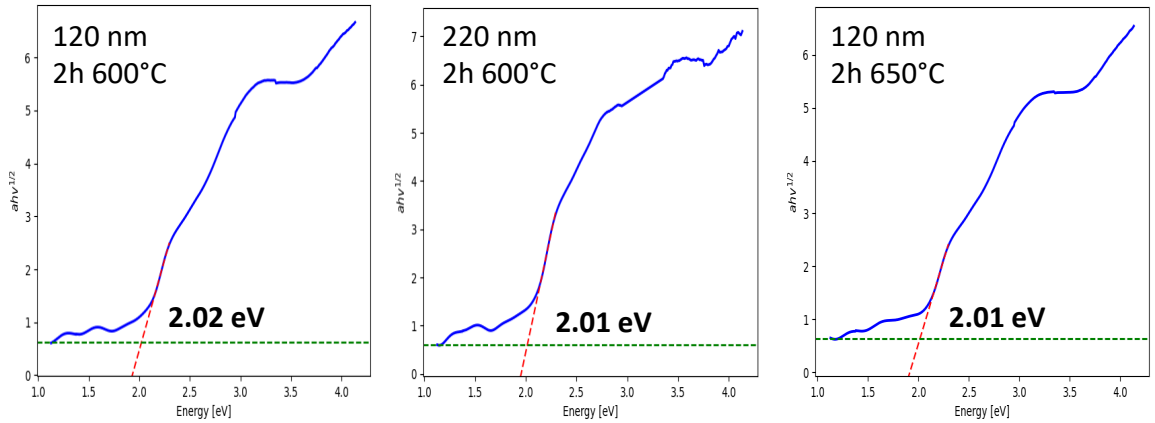

Figure 3.12: Tauc plots of iron oxide photoanodes realized with iron film with different thickness(120-220 nm) deposited on FTO.

Chapter 4

Experimental results: PEC and impedance characterization

In this chapter, the performance of the produced Fe_2O_3-based nanostructured photoanodes to promote water splitting is investigated. First, standard photoelectrochemical measurements are reported and compared to literature results. Then, the charge transfer processes in the dark and in visible light illumination conditions are addressed using Electrochemical Impedance Spectroscopy (EIS) and PhotoElectrochemical Impedance Spectroscopy (PEIS). Finally, the sample showing the highest photocurrent is investigated through CIMPS (Controlled Intensity-Modulated Photocurrent Spectroscopy) measurements, which provide further insights.

4.1 Effect of the annealing temperature on the functional properties of iron oxide photoanodes

4.1.1 I-V results

The Fig. 4.1 shows the I-V curve (normally called Linear Sweep Voltammetry, LSV) recorded in the dark for a photoelectrochemical cell prepared as described in Chapter 2 and in which the photoanode constituted by one of the FTO-Fe_2O_3 nanostructured layers discussed in Chapter 3. In particular, the Fig. 4.1 reports the results obtained starting from a 45 nm thick Fe film, annealed in air for 2 hours at different temperatures. The general behaviour is the same for all the anodes, and it is a sort of diode-like behaviour. This is related to the presence of a space charge region in the iron oxide layer close to the solid-liquid interface that has been depleted by majority carriers (electron in the case of hematite). Only when the anode polarization is sufficiently high to overcome the electric field generated by the depletion region, the current can flow. It should be noted that the current flow has to be considered here as a signature that water oxidation, that is, the chemical reaction attended at the anode surface, occurs. When this happens, as explained in Chapter 1, hydrogen is generated at the cathode. As shown in Fig. 4.1, as the temperature increases, the dark current at high potentials, exhibiting diode-like behaviour, decreases, and the onset values increase. Given that there is no precise definition of onset, an operational definition has been established. It was chosen to take the onset potential as the voltage value at which the current reaches the value of 0.1 mA/cm^2. The onset values, from lower to higher temperatures, are as follows: 1.65(1), 1.64(1),1.67(1), and 1.70(1) V vs RHE. The increase in resistance likely stems from a variation in the number of carriers, possibly associated with changes in oxygen vacancy amount. Hematite is anticipated to utilize oxygen vacancies as shallow donor dopants. The creation of an oxygen vacancy introduces two electrons per absent oxygen atom, increasing the overall majority carrier electron concentration and, consequently, conductivity. However, the introduction of two extra electrons may simultaneously convert Fe^{3+} to Fe^{2+}. At elevated concentrations, Fe^{2+} sites might function as recombination centres for photoexcited holes due to electronic states within the band gap. The evolution of photocurrent arises from the competition between these concurrent

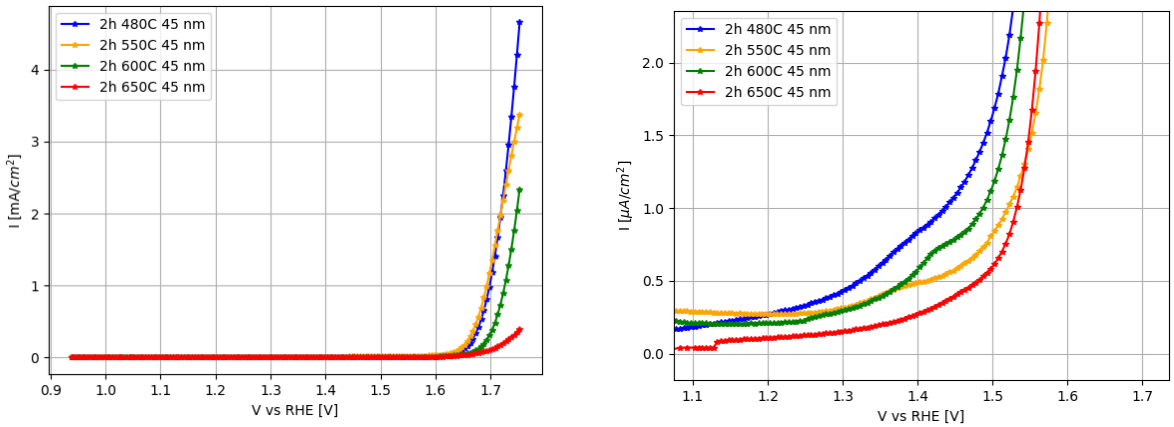

Figure 4.1: I-V plots of 45 nm Fe on FTO samples with varied temperature annealing, distinguished by colour (left). Zoom around the onset potential values of the same curves(right).

phenomena [59]. Thermal annealing in ambient conditions can modify oxygen vacancy quantities, resulting from O_2 in-diffusion from air to the films. As noted in [60], in the case of ZnO, an increase in annealing temperature correlates with a reduction in oxygen vacancies. As evidence that this phenomenon also occurs in this case, one could highlight the observed transition from magnetite to hematite [59] in the 250 nm Fe sample after a 3-hour annealing at 600°C discussed in Section 3.1. Upon

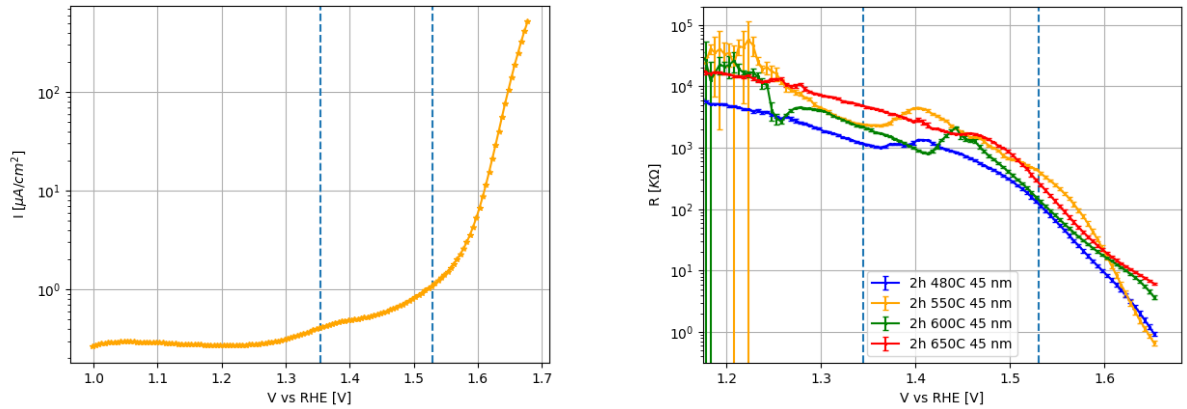

Figure 4.2: I-V plot in the dark condition of Fe sample on FTO heated 2 hours 550°C, divided into three zones (left). Resistance curves defined as derivatives of voltage with respect to current and obtained from I-V curves in the dark condition of Fe samples annealed at different temperatures distinguished by colour (right).

closer examination of the measured curves, exemplified in Fig. 4.2 (left), and a comparison with the curves derived from the voltage-current relationship, i.e., the resistance curves (Fig. 4.2 right), three distinct regions become evident: one at low potentials, characterized by virtually negligible currents (in the range of nA), an intermediate region where a more or less pronounced bump is noticeable (≈[1.35-1.55]V), and finally, a last part where the currents sharply increase. The region around 1.4 V is of significant interest, both due to its proximity to the reference potential of 1.23 V vs RHE, where the water splitting reaction takes place (as illustrated in Section 1.1), and because it is the zone where the signature from surface states occurs, as will be seen in the EIS analysis in Section 4.2.2.

Now, consider the results of a similar experiment performed by illuminating the sample with a white LED with a power of 25 mW/cm^2 from the side of the electrolyte/photoanode interface. The I-V curves of each single specimen are plotted together in Fig. 4.5. It can be seen that the current-to-voltage data exhibit the same diode-like behaviour observed under dark conditions. However, zooming in around the reference potential of 1.23 V (still Fig. 4.5) and comparing the current values with or

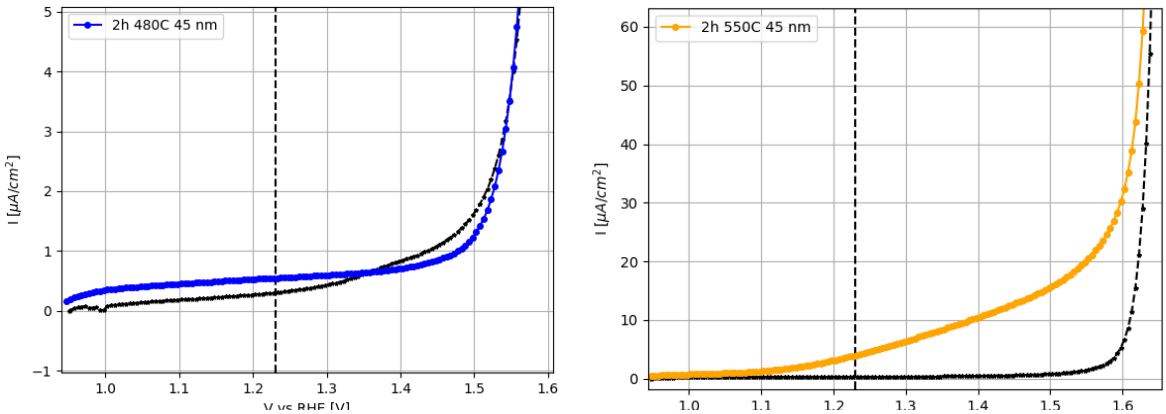

Figure 4.3: I-V curves in the illuminated condition of iron oxide photoanode realized on FTO, thermally annealed 2 hours at 480°C (left) and 550°C (right). Respective I-V dark curves are plotted in dashed line

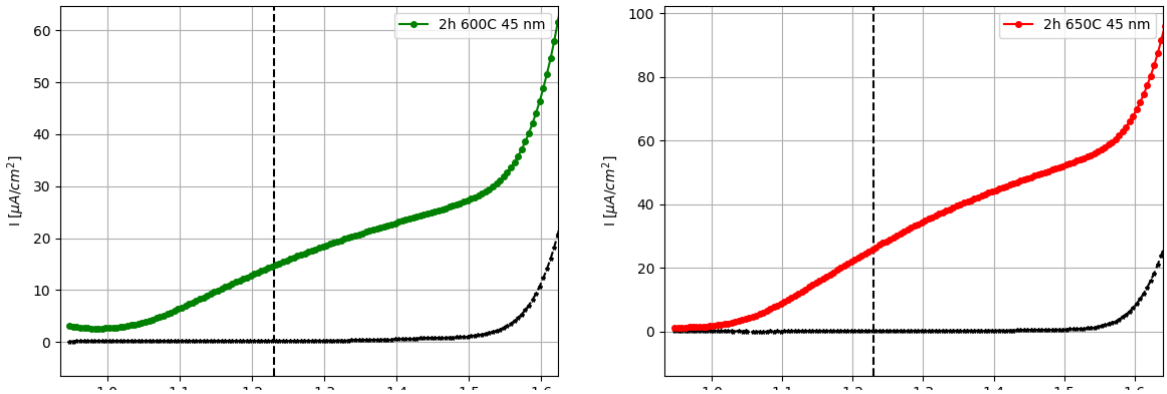

Figure 4.4: I-V curves in the illuminated condition of iron oxide photoanode realized on FTO, thermally annealed 2 hours at 600°C (left) and 650°C (right). Respective I-V dark curves are plotted in a dashed line.

without sample illumination, it is evident that from 1.0 V to 1.6 - 1.7 V, there is a more or less significant photocurrent signal, depending on the sample, with the exception of the sample heated to 480°C where the curves overlap from the beginning. Therefore, the LSV in light conditions can be divided into two regions: a so-called 'photoactive' region and a region after 1.6 - 1.7 V where the photocurrent is negligible, with respect to the current recorded in the dark condition. In this latter zone, the resistance trend versus temperature annealing T, found in the previous analysis of the I-V curves under dark conditions, is thus found. In the 'photoactive' region, the photogenerated holes are thus effectively transferred into the solution and have enough energy to promote the water oxidation reaction. A clear trend with respect to the annealing temperature is observed, as exemplified in Fig. 4.6, which shows the photocurrent values (light-dark) at the standard reference potential of 1.23 V vs RHE. As the temperature increases, the photocurrent also increases. Moreover, it should be noted that the recorded photocurrent certainly is due to the iron-oxide-based layer. Indeed, SEM analysis strongly suggests that the iron oxide film is completely covering the FTO substrate. Anyway, the photoelectrochemical response of the FTO substrate alone (with no iron deposition) has been recorded, and it is reported in Fig. 4.5 (under light illumination). It is clear that the FTO contribution to the photocurrent is negligible for V¡1.5V. One possible reason for this growth is the improvement in the crystal structure of the sample, particularly observed in the transition from T=480°C to T=550°C, as discussed in Section 2.5, thereby reducing the number of recombination centres. From the absorbance data, shown in Fig. 3.8, it can be inferred that as the temperature increases, the photoanode is able to absorb more photons and consequently generate a greater number of photocarriers. However,

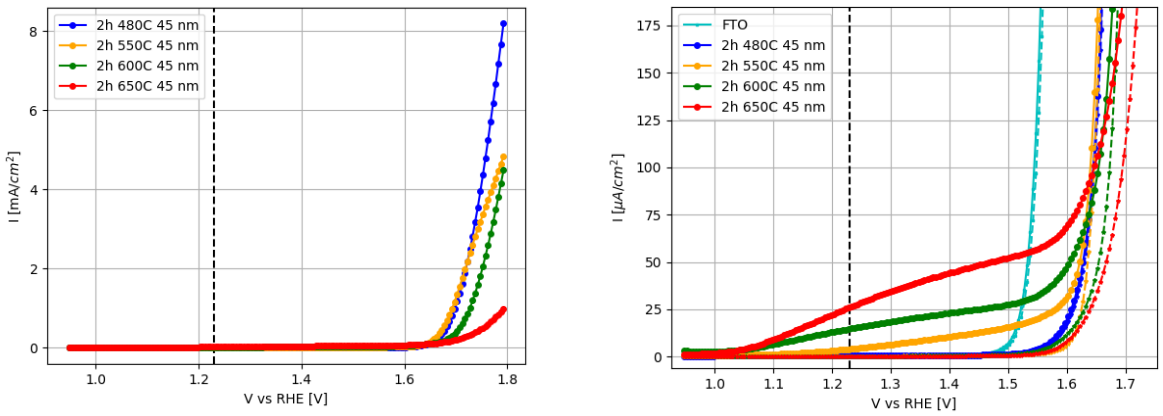

Figure 4.5: I-V plots in the illuminated condition of Fe sample on FTO heated 2 hours at different temperatures, distinguished by color (left). Inset of the same plots in the photoactive region, with I-V dark curves in dashed line superimposed with the same colour legend. FTO I-V dark and illuminated curves are shown in cyan(right).

it is thought that this factor alone cannot fully explain such a significant increase in photocurrent from 480°C to 650°C, considering that this growth pertains to a range not effectively covered by the available lamp, as seen in the Fig. 4.6. The same figure illustrates a comparison of the illumination ranges between the white LED used in this study and the solar spectrum recorded at sea level. It can be asserted that the best performance in terms of solar water splitting is achieved for the sample heated to 650°C ($I_{photo} = 26\ \mu A/cm^2$, see Fig. 4.6). Literature results on similar systems grown by PE-CVD indicate a photocurrent density of about 215 $\mu A/cm^2$ when illuminated by a solar simulator [18]. A thorough comparison would necessitate the use of a solar simulator, which will be available at DFA soon. Nevertheless, considering that the total power used accounts for one-fourth of the solar AM 1.5 spectrum and that the emission spectrum of the LED used only partially overlaps with the absorption spectrum of hematite (Fig. 4.6 right), the results obtained for the photoanode annealed at 650°C are likely not too far from the literature values.

Effect of Sn doping

To better understand the possible effect of Sn doping on the iron oxide nanostructured film, two photoanodes have been prepared, co-depositing Sn and Fe in the metallic form and then annealing to induce oxidation. In particular, the Fe target was placed on the DC torch and the Sn in the RF one. During this co-deposition, the sample holder was continuously rotating to ensure a spatially homogeneous deposition. By adjusting the RF source power, the fraction of Sn in the film can be controlled. Two different conditions were tested, obtaining two metallic films, 60 nm thick. The Sn fraction was measured by EDX, obtaining 1.5% and 3% for the two cases. Then, the samples underwent a thermal oxidation in air at 550°C for two hours. In Fig. 4.7, the I-V curves are shown and compared to those obtained before. The samples with deposited Sn also exhibit a diode-like behaviour and the existence of a photoactive region in the same potential range as seen before (approximately from 1.0 to 1.6 V). Observing the current values at high potentials, it is evident that a higher percentage of deposited Sn corresponds to a greater resistive behaviour. In the 'photoactive' region instead an increase in the Sn percentage leads to an increase in the photocurrent. At 1.23 V vs RHE, the values are as follows: 3.8 $\mu A/cm^2$ (Fe only), 22 $\mu A/cm^2$ (Sn 1.5%), and 43 $\mu A/cm^2$(3%). These results demonstrate a strong correlation with Sn doping, especially noting that the latter two values are in the same ratio as the concentration values found via EDX (1.5% and 3% respectively). Furthermore, the sample annealed at 650°C has a lower photocurrent than the Fe Sn 3% sample (at 1.23 V, 26 vs. 43 $\mu A/cm^2$) and is almost equal to the Fe Sn 1.5% sample (at 1.23 V, 26 vs. 22 $\mu A/cm^2$). The effect of Sn is therefore more significant in terms of photocurrent compared to the annealing

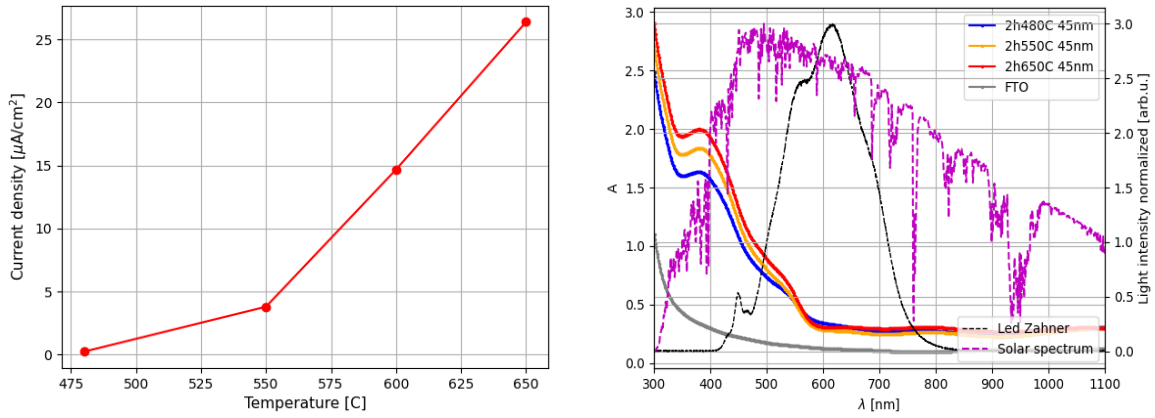

Figure 4.6: Photocurrent values, defined as $I_{light} - I_{dark}$ at 1.23 V vs RHE of Fe samples on FTO versus temperature annealing (left). Comparison of absorption spectra of the same samples and the intensity power spectra of the white LED used in this work and of the Sun. The spectra were normalized to their maximum (right).

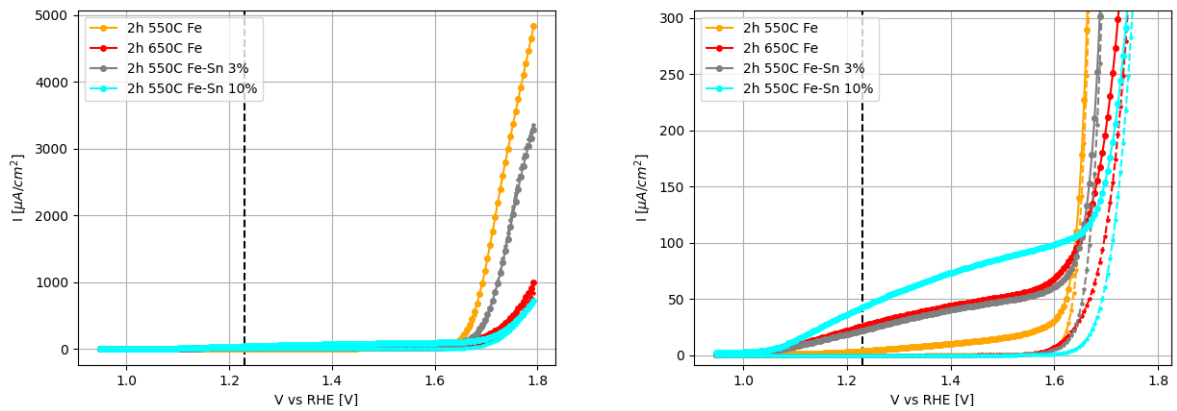

Figure 4.7: I-V plots in illuminated and dark(dashed line) condition for 45 nm Fe deposited on FTO annealed 2 hours at 550°C (yellow) and 650°C(red), and for 60 nm Fe-Sn deposited on FTO annealed 2 hours at 550°C with Sn nominal percentage of 3%(grey) and 10% (light blue). On the right, an inset in the photoactive area around 1.23 V vs RHE

temperature, and one may say that most likely the Sn percentage in the 45 nm 650°C sample is around 1.5%. One could argue that the thickness is not identical, but as will be seen in the Section 4.3, the increase in thickness actually lowers the photocurrent. Regarding the examined samples, an X-ray absorption spectroscopy (XAS) measurement is underway to measure the Sn site in the iron oxide layer. The fact that the photocurrent increases is likely due to the unintentional diffusion of Sn from the underlying FTO. The literature reports that, for hematite films deposited on this substrate, X-ray photoelectron spectroscopy (XPS) measurements show that Sn diffuses from 650°C [50] or even from 600°C [69]. Sn^{4+} ions incorporate into the hematite octahedral structure, replacing Fe^{3+} cations, acting as a dopant, particularly as an electron donor. As shown in [50], Mott-Schottky analyses indicate an increase in charge density in hematite nanostructures annealed at higher temperatures. However, ultra-fast transient absorption studies reveal that Sn doping does not affect the dynamics of photoexcited electrons, which operate on a picosecond scale, thus influencing the separation of photo-generated charges. In [62], a comparison is reported between two 600 nm iron samples deposited via sputtering, one on Au and one on FTO, both subjected to the same thermal treatments (2h at 500°C and 10 min at 800°C). The sample deposited on gold shows no photocurrent, suggesting the crucial role of Sn in tuning the photocurrent performance.

4.2 Impedance results

Now, further insights into the effect of annealing temperature from the analysis of impedance spectra in the dark and under illumination will be described. To conduct this analysis, it was useful to effectively represent the physical system with a circuit model, which is now introduced.

4.2.1 Charge transfer through photoanode/solution: equivalent circuit

The main purpose of EIS is to provide an interpretation of current-to-voltage curves, specifically aiming to address the contributions leading to $R_{tot} = \frac{dV}{dI}$. Through an equivalent circuit model (EC) composed of resistive and capacitive elements, which correspond to specific physical processes, an interpretation of impedance data across a broad spectrum of frequencies is achieved. The EC describes the sequential displacement/accumulation of carriers in distinct processes within the system, together with the specific locations that produces steps of Fermi levels of the carriers, in relation to the electrostatic potential distribution in the system [15]. It is occasionally argued that the interpretation of results based on EC is ambiguous due to the possibility of different equivalent representations of a given impedance function. While various representations of a single physical-chemical model are possible, it is also true that EC allows for the conveyance of a substantial amount of information, especially when a simplified model is used, taking into account the actual information contained in the data. Hematite photoanodes benefit from a well-established equivalent circuit model for interpreting impedimetric data in both dark and light conditions. This model, introduced by Bisquert and colleagues in [15], is derived from a theoretical kinetic model discussed in [66]. The proposed physical

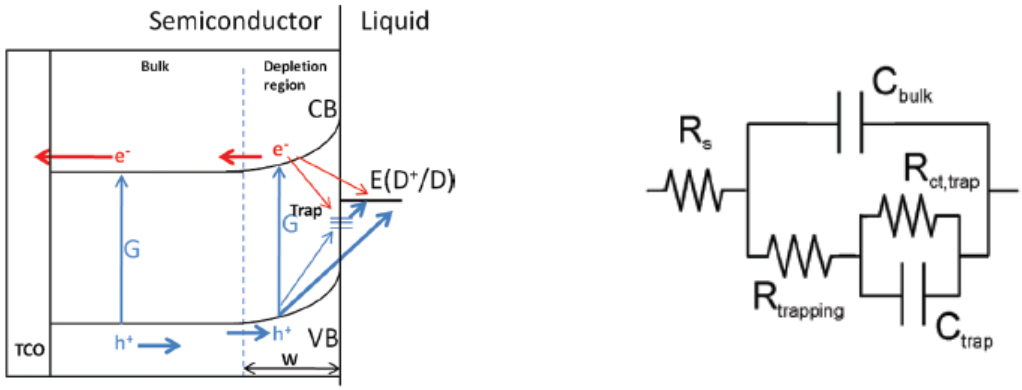

Figure 4.8: Physical model which describes the dynamics of charge carriers (left) and its equivalent circuit in simplified version (right) [15].

model for the dynamics of charge carriers is illustrated in Fig. 4.8(left), depicting their generation (G) through processes such as light absorption, surface-state trapping, and interfacial charge-transfer reactions. The associated circuit model is presented in Fig. 4.8(right), composed of the following individual elements. R_S is the resistance associated to the cell, i.e. the solution, the electric contacts and the internal resistance of the instrument. C_{bulk} is given by the series combination of two dielectric-origin capacitors: the capacitance associated with the space charge region (C_{sc}) and the capacitance associated with the Helmholtz layer (C_h), which was already described in Section 1.2. $R_{trapping}$ describes the phenomena of recombination and trapping of electrons and holes in surface states within the conduction and valence bands. On the other hand, $R_{ct,trap}$ characterizes the charge transfer from these surface states to the solution. Finally, C_{trap} is the surface-state capacitance defined as:

$$C_{trap} = AqN_{ss}\frac{\partial f_{ss}}{\partial E_{Fn}} \tag{4.1}$$

where A is the surface area of the electrode, q is the elementary charge, N_{ss} and f_{ss} are the surface states density and their fractional occupancy, E_{Fn} is the electron Fermi level as defined in Section 1.2.

As from the formula above, the capacitance reach its maximum value when the applied potential allows for a charging of the surface states, condition that occurs when the energy of the electronic quasi-Fermi level is very close to the energy of the unoccupied surface states. Note that the process related to charge transfer in solution from surface states is conditioned by trapping/detrapping from the bulk to these states. This logic is exemplified by the fact that the two RCs are nested.

The impedance spectra predicted by the model are characterized by the presence of two arcs in the Nyquist plot. The experimental data, at first glance, confirm this interpretation, more or less

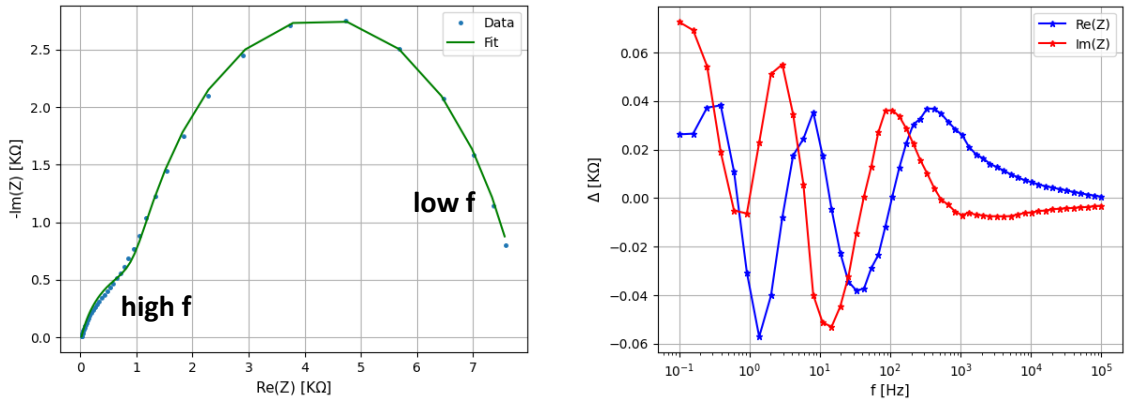

Figure 4.9: Experimental real and imaginary impedance data with fit superimposed shown in a Nyquist plot (left) and their correspondent fit residuals (right). The data, measured in dark condition at V = 1.63 V, refers to the sample with 45 nm Fe film deposited annealed in air for 2 hours at 650°C.

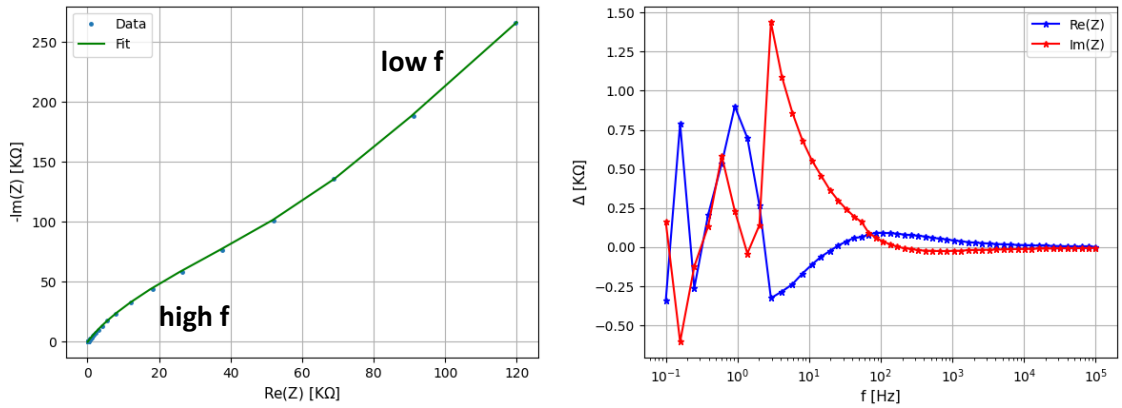

Figure 4.10: Experimental real and imaginary impedance data with fit superimposed shown in a Nyquist plot (left) and their correspondent fit residuals (right). Here the two circles seen in the above figure are not yet clearly visible. The data, measured in dark condition at V = 1.33 V, refers to the sample with 45 nm Fe film deposited annealed in air for 2 hours at 650°C.

explicitly (see Fig. 4.9 and Fig. 4.10 as two examples that will be discussed in the next paragraph). The data were then analyzed using a custom program based on the Python library impedance.py [67]. Since the capacitors are not ideal, they were replaced by constant phase elements (CPE). The impedance of the CPE is described by the following equation:

$$Z_{CPE} = \frac{1}{Q(j\omega)^n} \tag{4.2}$$

where Q, expressed in F s^{n-1}, is the parameter containing the capacitance information, and n is a constant ranging from 0 to 1. The origin of constant phase elements is commonly attributed to

the surface roughness of solid electrodes, which, in turn, results in an uneven distribution of various properties across the electrode surface. Alternatively, other theories suggest that the origin of CPE is linked to the mixed diffusion-kinetic controlled adsorption of ions or other impurities from the electrolyte onto the electrode surface. These two theories align in the sense that at a higher surface roughness, the coverage due to the adsorbed ions or impurities is smaller [40]. The capacitance values are then obtained using the formula proposed by Brug et al. in [68], in the case where R and CPE are in parallel and connected in series to R_s:

$$C = Q^{\frac{1}{n}} \left(\frac{1}{R_s} + \frac{1}{R} \right)^{\frac{n-1}{n}} \tag{4.3}$$

Lastly, the time constant are derived, $\tau = RC$. For simplicity, in the following, the τ are also nominated 'high' and 'low', for trapping/detrapping and charge transfer from surface traps respectively. In addition, the samples are labelled only by their annealing temperature, i.e '480°C' etc. In the next section EIS data and analysis in dark condition are presented. Then PEIS data and the comparison with the previous are shown.

4.2.2 Impedance analysis

The impedance spectra were acquired applying to a continuous polarization a perturbation amplitude of 5 mV over a frequency range from 100 mHz to 0.1 MHz. The DC potential was varied from 1.13 to 1.63 V vs RHE in steps of 50 mV. Taking the iron oxide photoanode annealed at 650°C as an example, a first case study, the impedance spectra recorded in dark condition ant different polarization potential values are reported in Fig. 4.11 (in form of Nyquist plot) and in Fig. 4.12 (in form of -Im(Z) and Re(Z) vs the excitation frequency). It can be observed that the curves overlap until V=1.43 V, forming a broad low-frequency arc, overlapping with a less distinguishable arc visible at at higher frequencies. Further increasing the potential, impedance, as seen in the dark I-V, drastically decreases, allowing the closure of the low-frequency arc and better distinguish the two contributions (see Fig. 4.11 right, at V=1.63 V). Nevertheless, these two processes can still be adequately resolved even at low potentials with the circuit described in the previous section. In Fig. 4.11 the best fit curves, obtained using the model described in the previous paragraph, are superimposed to the experimental data. The model's effectiveness is confirmed by residuals, reported in Fig. 4.13. Moreover, the resistance R_{lsv} derived from the I-V should be equal to the sum of the resistances obtained from the impedance fit: $R_{lsv} = R_s + R_{trapping} + R_{ct,trap}$. The overlap of these parameters is shown in the Fig. 4.14, also for the other studied samples.

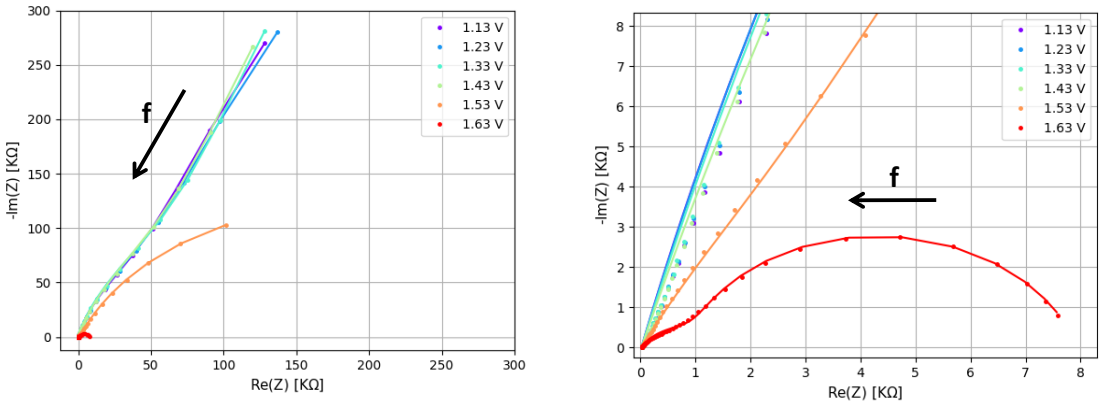

Figure 4.11: Impedance data Z, with fit superimposed, of 45 nm Fe deposited on FTO annealed in air for 2-hour at 650°C, measured in dark condition at different DC voltage distinguished by color. They are displayed in Nyquist mode, i.e. -Im(Z) vs. Re(Z). Frequency increases from the right to the left. On the right zoom of the plot in the low impedance region at V=1.63 V vs RHE.

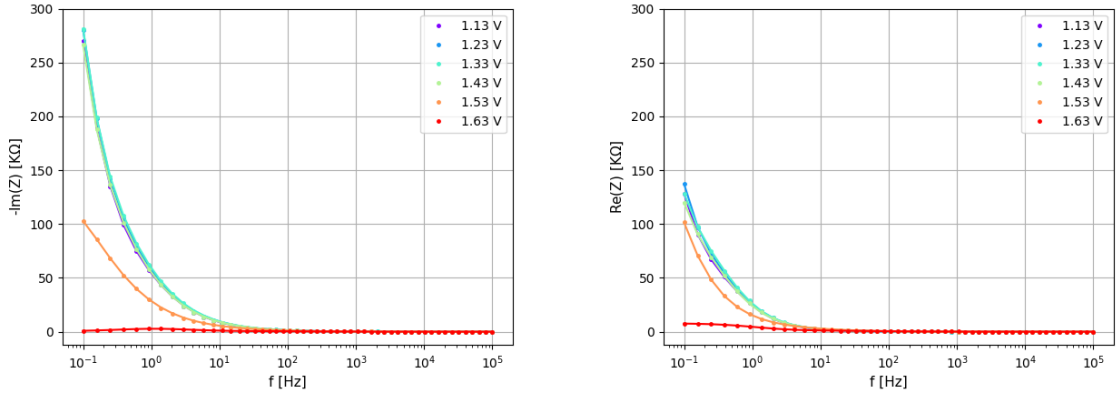

Figure 4.12: Imaginary (left) and real (right) impedance data, wit fit superimposed, of 45 nm Fe deposited on FTO annealed in air for 2-hour at 650°C, measured in dark condition at different DC voltage distinguished by color.

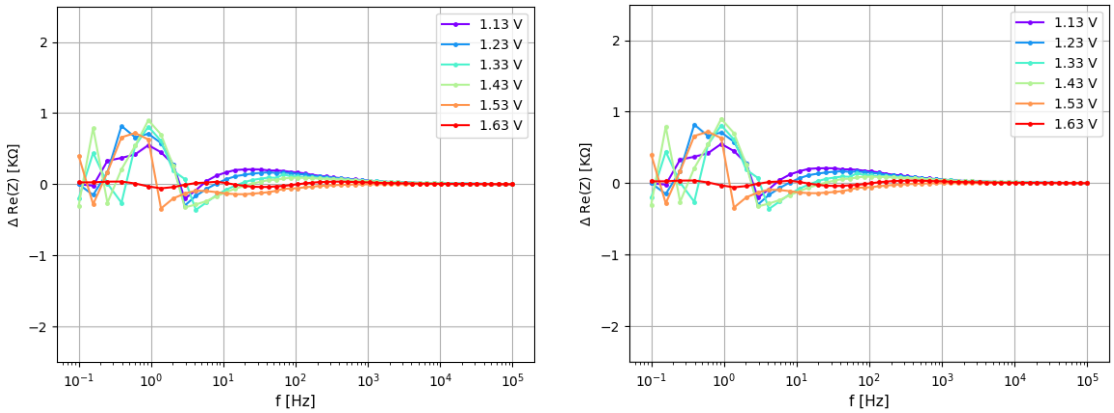

Figure 4.13: Imaginary (left) and real (right) fit residuals of 45 nm Fe deposited on FTO annealed in air for 2-hour at 650°C, measured in dark condition at different DC voltage distinguished by color.

So expanding the overview to all four samples, the effect of the annealing temperature on the impedance spectra can be observed in Fig. 4.15 and subsequent figures. It can be noted that the impedance reach its maximum at V=1.33 V. Looking at the impedance components versus frequency (Fig. 4.18) at the lower potential (1.13 V), the imaginary part surpasses the real part. Conversely, at the higher potential (1.63 V), the opposite occurs (Fig. 4.19). Note that in the plot of Im(Z) vs. f at 1.63 V, for example in the case of 650°C, there are two processes, one around 1 Hz, another after 30 Hz. The curve is 'shifted' towards higher frequencies, indicating faster characteristic times of the processes involved, compared to the others.

Moving to a more quantitative analysis, the results of the fits are now presented. In particular, the individual elements of the used equivalent circuit, their trends, their behaviour with varying temperature, and any correlations between them are analyzed. Firstly, as can be seen in Fig. 4.20, it is observed that $R_{trapping}$ and $R_{ct,trap}$ are separated by approximately 1-2 orders of magnitude, and follow the same trend regardless of temperature, decreasing their values starting from about 1.5 V. For $R_{trapping}$, there is an additional confirmation of the results from the I-V analysis, indicating that as the temperature increases, the material becomes more resistive. Regarding $R_{ct,trap}$, on the other hand, a clear trend with respect to temperature cannot be deduced. However, to some extent, the three regimes shown in Fig. 4.2 are reflected:

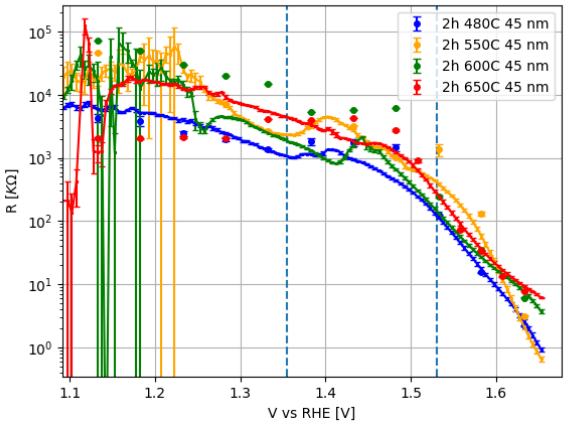

Figure 4.14: Comparison between the resistance value from LSV R_{lsv} and the sum of the resistance found with EIS analysis $R_{tot} = R_s + R_{trapping} + R_{ct,trap}$.

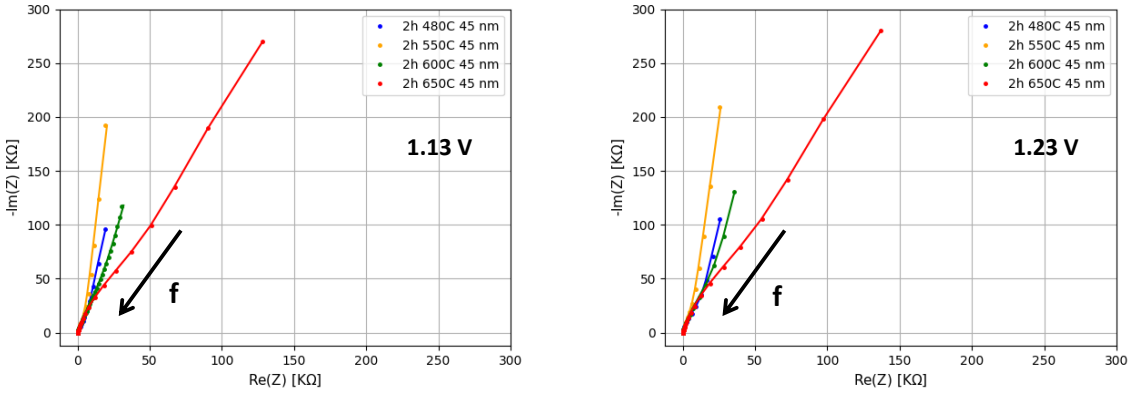

Figure 4.15: Nyquist plot of experimental EIS data (points marker) in dark condition of Fe sample annealed at different temperatures, at 1.13 V(left) and 1.23 V vs RHE (right). The fit is superimposed and the color legend is the following: blue (480°C), yellow(550°C), green(600°C) and red 650°).

- a region at low potentials where the resistance is very high, if not infinite (samples at 550°C and 600°C), in which the charge transfer from surface states (SS) is almost negligible, probably because there is no charge on the SS. It is noteworthy that the sample at 650°C in this region has relatively lower and stable values;
- a second zone around 1.3 and 1.5 V where the resistance stabilizes at a constant value, likely indicating an ongoing chemical reaction step;
- finally, a third region where the behaviour seen in the LSV is reproduced.

The decrease in $R_{ct,trap}$ is correlated with the increase in C_{trap} (from 10^{-5} to 10^{-3} Fcm^{-2}) for V¿1.5 V vs RHE as can be seen in Fig. 4.21. Following the reasoning presented in [15], this indicates a favored channel for charge transfer from the populated SS. Below 1.5 V, the values of C_{trap} are comparable with C_{bulk}, which shows a constant trend with respect to V and, given its dielectric nature, an inverse relationship with T (higher T, lower capacitance values, lower currents). In particular, for the sample at 650°C, C_{bulk} is an order of magnitude lower (10^{-6} vs 10^{-5}) compared to C_{trap}. The values can be partly compared with those reported in the article [15], where the authors use a simplified version of the circuit consisting of an RC in series with the resistance R_s (Randles circuit). Large values for resistance, around $10^8 \Omega cm^2$, and bulk capacitance values around $10^{-6} F cm^{-2}$ are reported, lower

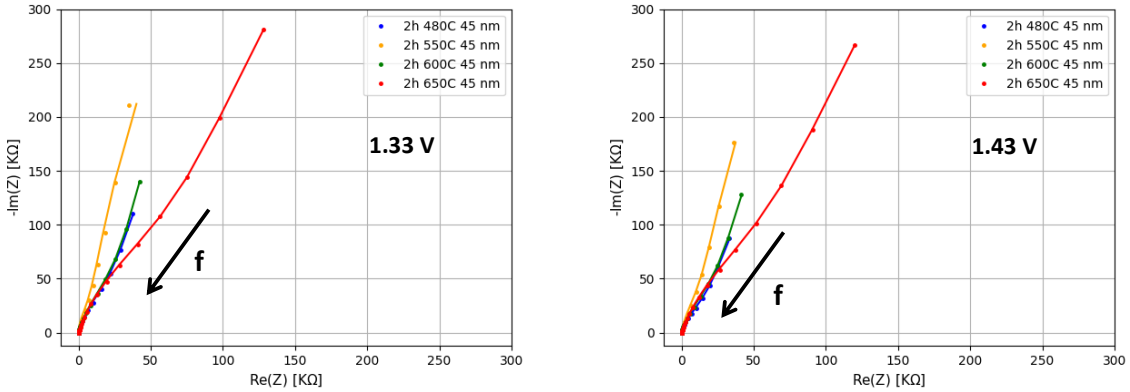

Figure 4.16: Nyquist plot of experimental EIS data (points marker) in dark condition of Fe sample annealed at different temperatures, at 1.33 V(left) and 1.43 V vs RHE (right). The fit is superimposed and the color legend is the following: blue (480°C), yellow(550°C), green(600°C) and red 650°).

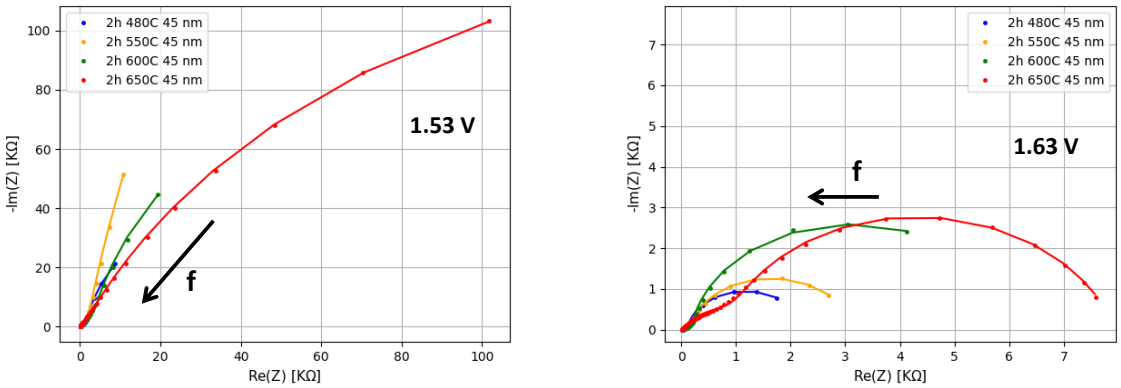

Figure 4.17: Nyquist plot of experimental EIS data (points marker) in dark condition of Fe sample annealed at different temperatures, at 1.53 V(left) and 1.63 V vs RHE (right). The fit is superimposed and the color legend is the following: blue (480°C), yellow(550°C), green(600°C) and red 650°). Note the change of scale.

than what was found ($10^{-5} Fcm^{-2}$ except for 650°C, where it is $10^{-6} Fcm^{-2}$). This suggests that the effective extension of the surface in contact with the solution is in the present case higher than the pure geometrica area, due to the rough surface of the photoanode. Regarding the times (see Fig. 4.22, two processes can be distinguished: the slow process of charge transfer from surface states to the solution, which at 1.4 V vs RHE for all samples is on the order of 10 s, and a faster process of charge transfer to surface states from the bulk, on the order of 1 s at 1.4 V again for all samples, which fast drops down after 1.5 V (10^{-2} s at 1.63 V). The latter is partially in line with what is reported in [15]. A clear trend with respect to temperature is not clearly visible, except for the fact that for the photoanode annealed at 650°C, the slow process (Fig. 4.22 right) is the fastest.

For samples heated to temperatures exceeding 550°C, the same EIS scan was performed while illuminating the sample with a white LED centered around 600 nm with a power of 25 mW/cm^2. The Photoelectrochemical Impedance Spectroscopy (PEIS) raw data with the overlaid fit are presented in Fig. 4.23 and subsequent with the same color legend used so far. From a qualitative perspective, one can observe a clear difference between the spectra of 550°C compared to those at higher temperatures. While the former exhibits a very broad arc that only closes at high potentials, the latter two display two arcs already at low polarization potential, with their shape and overlap changing with varying

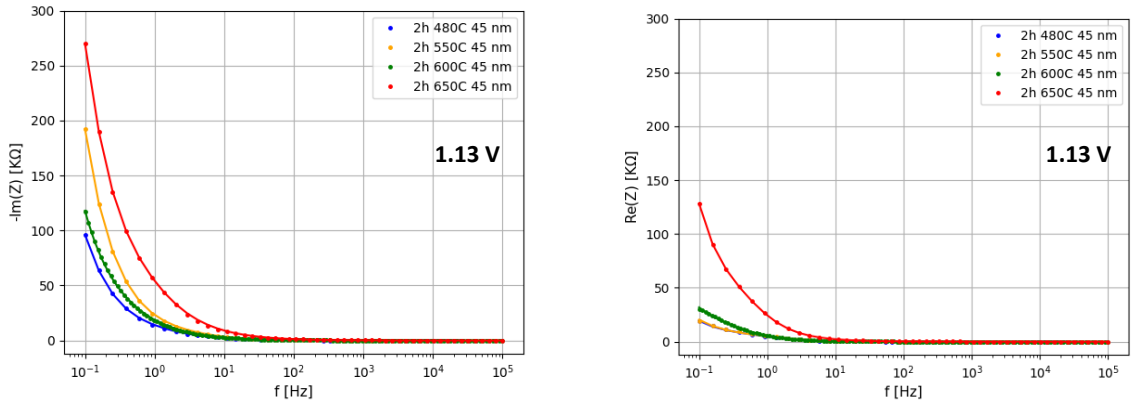

Figure 4.18: Real(left) and imaginary part (right) of impedance data (points marker) in dark condition of Fe sample annealed at different temperatures, at 1.13 vs RHE. The fit is superimposed and the color legend is the following: blue (480°C), yellow(550°C), green(600°C) and red 650°).

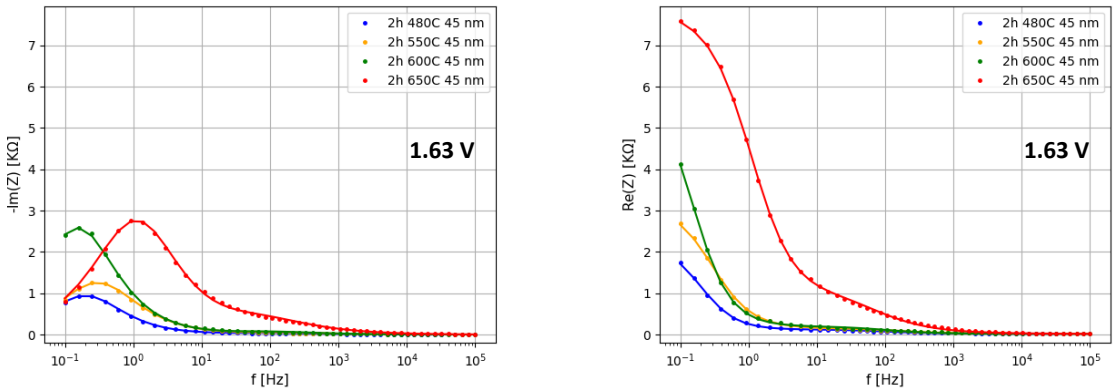

Figure 4.19: Real(left) and imaginary part (right) of impedance data (points marker) in dark condition of Fe sample annealed at different temperatures, at 1.63 vs RHE. The fit is superimposed and the color legend is the following: blue (480°C), yellow(550°C), green(600°C) and red 650°).

potential values. In these cases, it is more evident that around 1.43 V, the impedance reaches its maximum value (see also the plot of Z components vs. frequency in Fig. 4.25 and Fig. 4.26). A perfect agreement was found between the resistances obtained through fitting and the resistance curves from the light I-V, except for the 550°C sample (Fig. 4.28). This is likely due to the presence of a third contribution at high frequencies (around 10 kHz), independent from the DC voltage applied, that the model does not describe. Further investigation are needed to understand this point. An interesting characteristic evident from the fit results pertains to low-frequency resistances (Fig. 4.29). In the samples at 600°C and 650°C, a decreasing trend of the reistance values $R_{ct,trap}$ is observed from low potentials to approximately 1.38 and 1.43 V, followed by an increase of about one order of magnitude before descending again around the onset value. This trend is correlated with the observed trend for C_{trap} (not observed for 550°C), which corresponds to the findings in the article by Bisquert et al. mentioned above [15], including the potential window at which this occurs (see Fig. 4.30). Based on Eq. (4.1), the capacity associated with surface trap states peaks around these energies, corresponding to the main energy level of these states. The fact that R_{trap} resistances decrease and are lower than $R_{trapping}$ during the charging process further confirms that this process is the main charge transfer pathway. Regarding the high frequency resistances, it is observed that before the onset of the current, they are more or less similar (650°C is again the least resistive), but for V¿1.5V, the trend seen in the

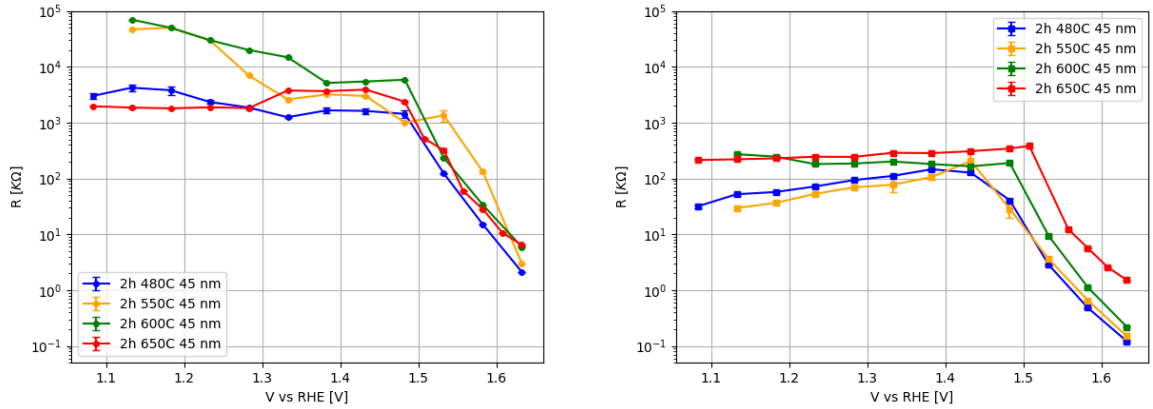

Figure 4.20: $R_{ct,trap}$ (left) and $R_{trapping}$ (right) from analysis of EIS in dark condition of 45 nm Fe sample annealed at different T, distinguished by color.

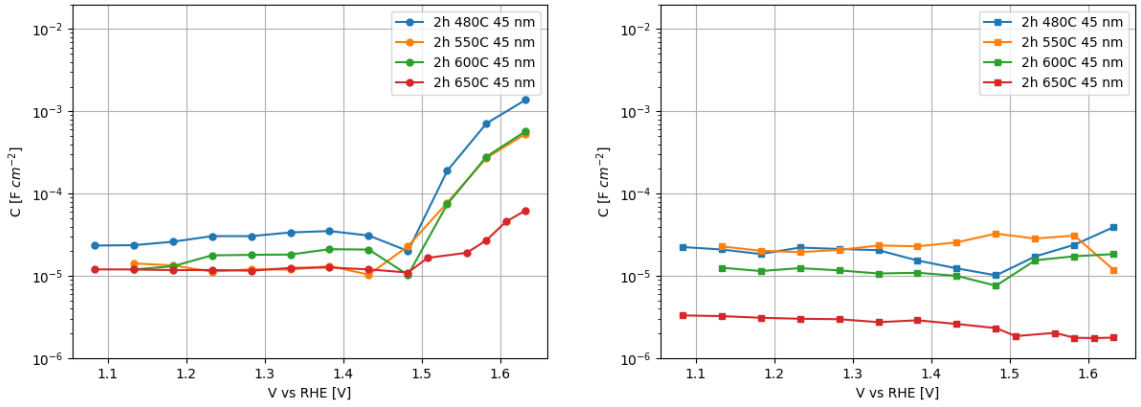

Figure 4.21: C_{trap} (left) and C_{bulk} (right) from analysis of EIS in dark condition of 45 nm Fe sample annealed at different T, distinguished by color.

dark (higher temperatures, more resistive) is repeated (Fig. 4.29). Finally, the C_{bulk} capacity of 650°C is nearly an order of magnitude lower than the other two samples heated at lower temperatures, but the constant trend is similar (Fig. 4.30). A comparison of times with ref. [15] shows a difference of about one order of magnitude in the charge transfer process from surface states in solution (about 1 s vs. 0.1 s reported at 1.2 V vs RHE) and one or two orders of magnitude, depending on the chosen sample, for the faster bulk process (0.1 s, or for 650°C 0.01 s, vs 1 ms reported at 1.2 V vs RHE). The comparison is partly affected by the fact that the experimental lighting conditions are different: the authors use a solar simulator with a filter to reduce the power to 33 mW/cm^2, still higher than the power of 25 mW/cm^2 used in this work. The values of time constants obtained from the analysis are shown in Fig. 4.31.

It is now interesting to compare the EIS results in light and darkness, aiming to gain additional insights. As a case study, the sample exhibiting the highest photocurrent value at 1.23 V vs RHE is chosen, namely, the photoanode realized with a 45 nm thick Fe film deposited and annealed in air at a temperature of 650°C. As can be seen in Fig. 4.34 the parameters $R_{trapping}$ and C_{bulk} do not vary so much, wherease a significant discrepancy is observed in both resistance and capacitance related to surface states, as depicted in Fig. 4.33. Photoexcitation of hematite is indeed necessary to allow charge carriers to significantly fill the trap states. It is then observed that at high potentials, above 1.53 V, the discrepancy decreases, aligning with the experimental observation that the photocurrent

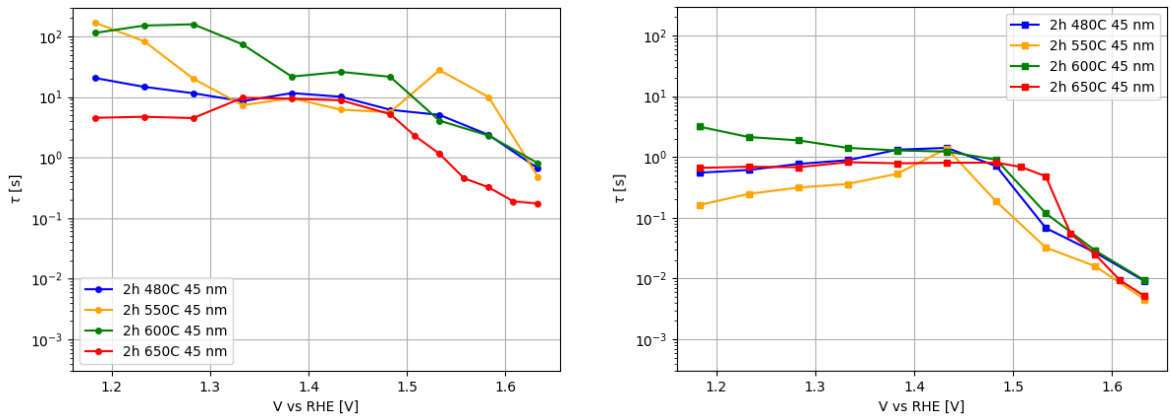

Figure 4.22: τ_{SS} (left) and τ_{bulk} (right) from analysis of EIS in dark condition of samples with 45 nm Fe deposited and annealed at different T, distinguished by color.

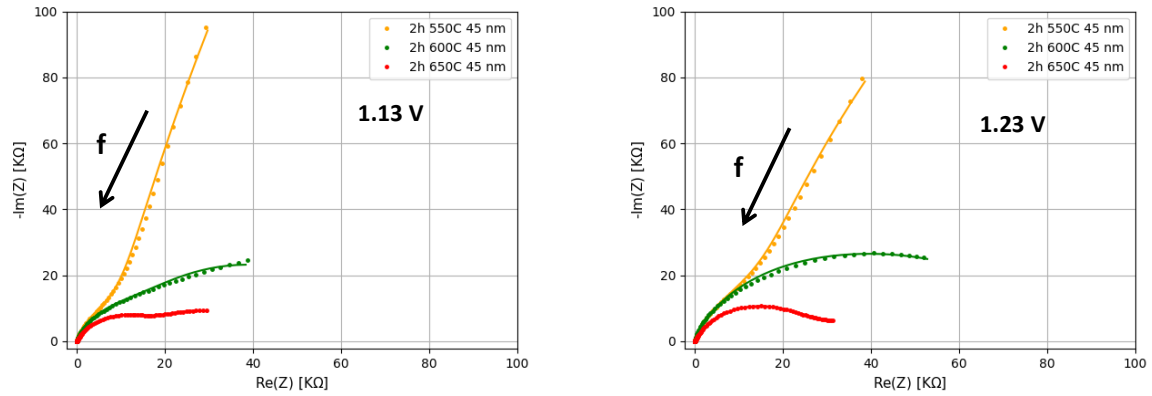

Figure 4.23: Nyquist plot of experimental EIS data (markers) in illuminated condition of iron oxide photoanodes annealed at different temperatures, at 1.13 V(left) and 1.23 V vs RHE (right). The fit is superimposed to the data.

drops down. Regarding the time constants values it can be noticed in Fig. 4.34 that when illuminating the sample the processes of charge transfer are faster.

So it was observed that the model is sufficiently efficient in describing the impedance data and resolving two contributions, with relatively close times that at V = 1.4 V vs RHE are as follows: $\tau_{bulk} = 1$ s (in dark condition), 0.1 s (illuminating), $\tau_{bulk} = 10$ s or more (in dark condition), 1 s (illuminating). It was then noted that a higher photocurrent response is correlated with the presence in the impedance data fit results under illumination conditions of a peak in the chemical capacity C_{trap} describing the occupation of surface states in the range 1.3 V-1.5 V vs RHE, and a decrease in the charge transfer resistance from these states to the solution $R_{ct,trap}$ in the same range. Additionally, it is observed that the peak of C_{trap} is visible under illumination conditions. These trends are in line with what is discussed in [15], where the connection is emphasized with the fact that the photoexcitation of hematite is indeed necessary to allow charge carriers to significantly fill the trap states, and that the potential range in which the phenomenon occurs is related to the principal energy level of these states.

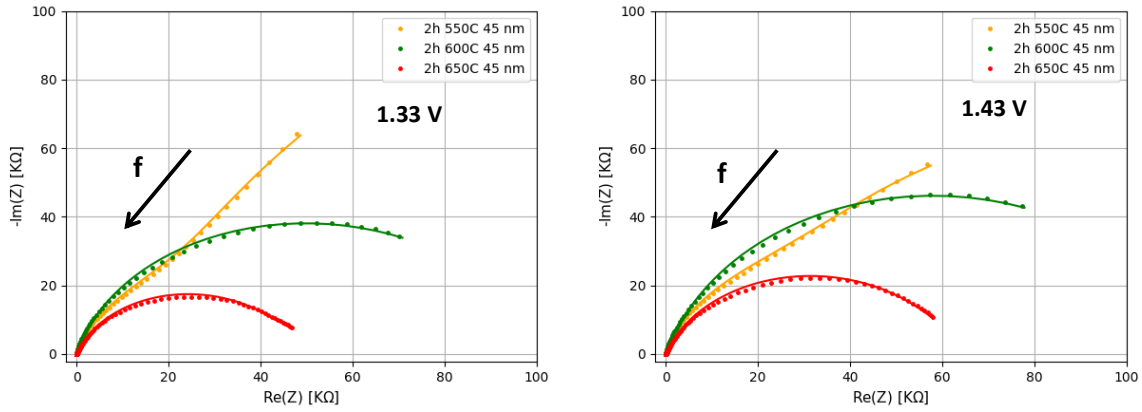

Figure 4.24: Nyquist plot of experimental EIS data (markers) in illuminated condition of iron oxide photoanodes annealed at different temperatures, at 1.33 V(left) and 1.43 V vs RHE (right). The fit is superimposed to the data.

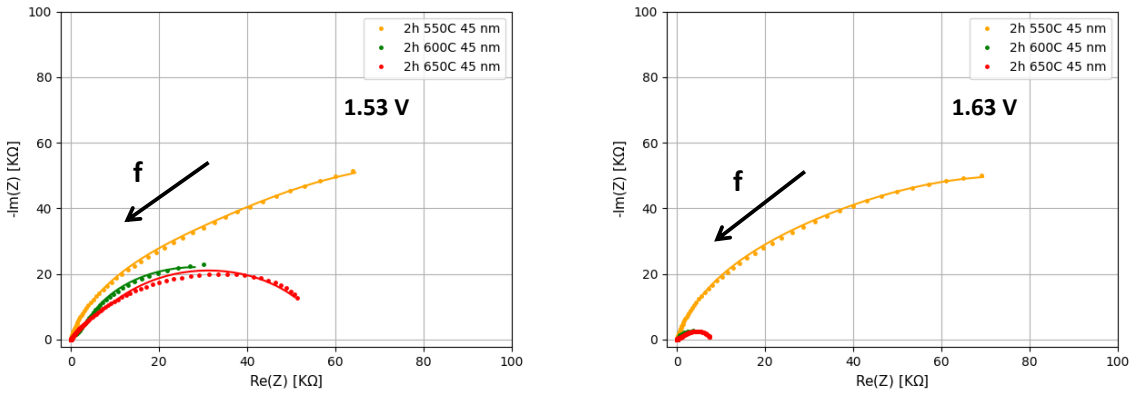

Figure 4.25: Nyquist plot of experimental EIS data (markers) in illuminated condition of iron oxide photoanodes annealed at different temperatures, at 1.53 V(left) and 1.63 V vs RHE (right). The fit is superimposed to the data.

4.3 Effect of the layer thickness on the functional properties of iron oxide photoanodes

The impact of the film's thickness on the photoelectrochemical properties of hematite photoanodes constitutes another crucial parameter. The PEC results of samples annealed for 2 hours at 600°C and 650°C with varying thicknesses (45, 120, 220 nm) are now presented. Unfortunately, the 220 nm sample at 650°C broke during the annealing process, as this temperature poses a risk to the soda-lime glass, which serves as the main substrate for the FTO.

4.3.1 I-V results

From the current-voltage curves measured under dark conditions, as shown in Fig. 4.35, it is observed that at high potentials increasing the thickness increases the resistance. In order of thickness, the onset voltage values, defined as in Section 4.1.1, for photoanodes annealed at 600°C are: 1.67(1) V, 1.72(1) V, and 1.77(1) V. Instead for samples annealed at 650°C they are: 1.70(1)V and 1.78(1) V. Before the onset voltage, thicker samples exhibit a higher dark current compared to 45 nm samples. In particular, the 120 nm sample at 600°C shows a predominantly ohmic behaviour in the region of

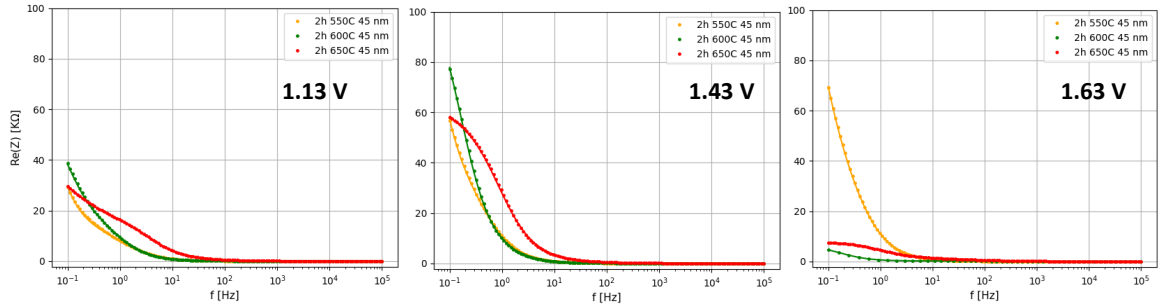

Figure 4.26: Real part of impedance data (markers) in illuminated condition of iron oxide photoanodes annealed at different temperatures, at 1.13, 1.43 and 1.63 vs RHE. The fit is superimposed and the color legend is the following: yellow(550°C), green(600°C) and red 650°)..

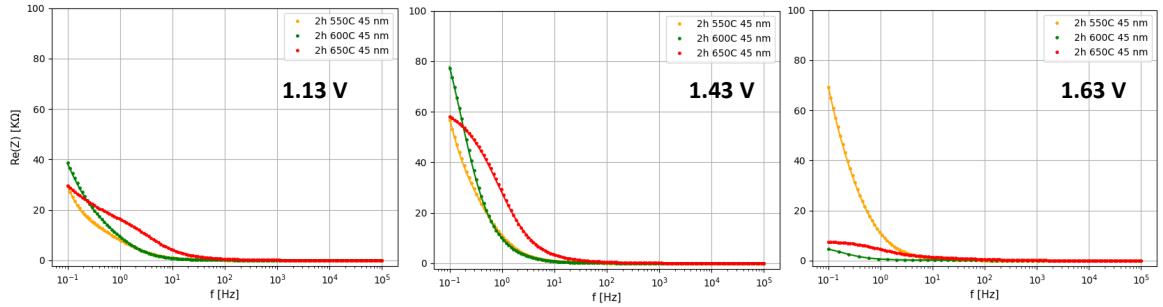

Figure 4.27: Imaginary part of impedance data (markers) in illuminated condition of iron oxide photoanodes annealed at different temperatures, at 1.13, 1.43 and 1.63 vs RHE. The fit is superimposed to the data.

interest around 1.23 V, as depicted in Fig. 4.35. It is noteworthy that, even for a thickness of 120 nm, the previously observed result is confirmed, indicating that higher temperatures result in greater resistance. Conducting the same measurement under light, illuminating with a white LED from the anode/electrolyte interface side, it is observed that at a fixed annealing temperature of 600°C, increasing the thickness from 120 nm to 220 nm leads to a decrease in photocurrent (see Fig. 4.36). It is also observed that at higher voltages, the dark and light currents overlap at higher potentials for greater thickness. Focusing on the region of interest around 1.23 V, as shown in Fig. 4.36 (right), it is noted that the current for the photoanode obtained from a Fe deposition of initial thickness of 120 nm is higher than the one obtained from a thinner deposition (45 nm), but the contribution of photocurrent is lower. Then it can be stated that with greater thickness, the photocurrent is lower. This result is more pronounced at T=650°C (see Fig. 4.37). The photocurrent values at 1.23 V vs RHE are plotted in Fig. 4.38, where the decreasing trend with thickness is clearly visible. Particularly at 1.23 V vs RHE, the percentage difference of photocurrent going from 45 nm to 120 nm and 220 nm is respectively -30% and -55%, while for 650°C from 45 nm to 120 nm is -20%.

Analyzing the possible reasons explaining these results, it is important to note that, based on absorption data (Section 3.3), one could expected a higher photocurrent signal with increasing thickness, in agreemnet with a higher light absorption (see Fig. 3.11). Focusing on photoanodes annealed at

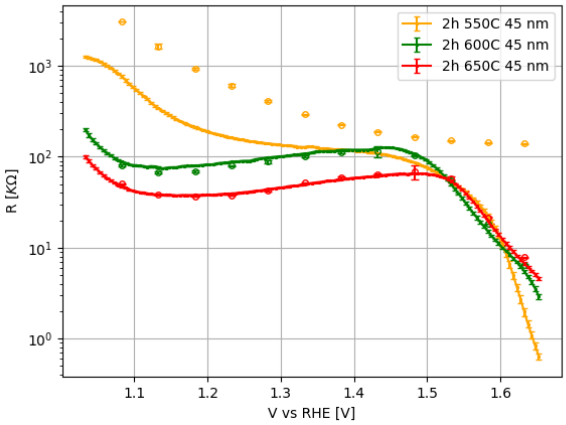

Figure 4.28: Resistance curves, defined as derivatives of voltage respect to current, obtained from I-V curves in illuminated condition of Fe samples annealed at different temperature distinguished by color.

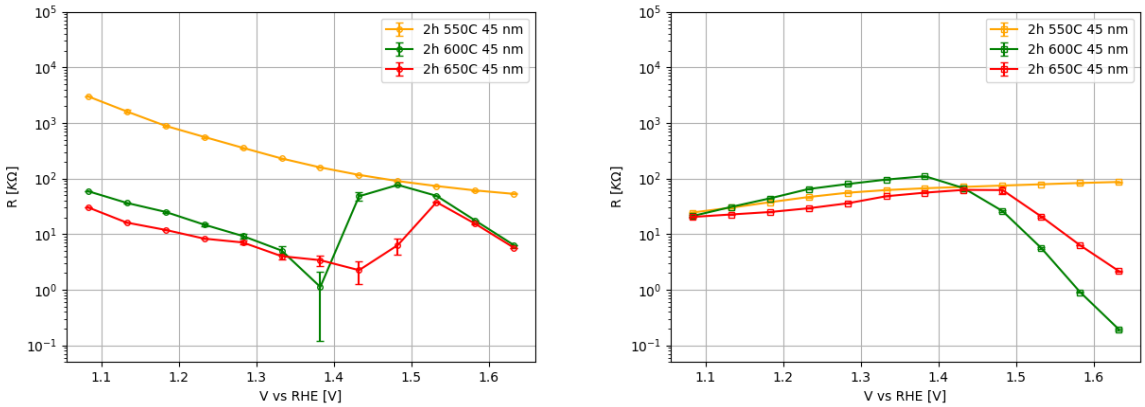

Figure 4.29: $R_{ct,trap}$ (left) and $R_{trapping}$ (right) from analysis of EIS in illuminated condition of 45 nm Fe sample annealed at different T, distinguished by color.

the temperature T = 600°C, a possible explanation for low photocurrent obtained from the thickest photoanode could take into account the following observations. Compared to others, it is the most resistive, as evident from the dark currents. The results of the GIXRD analysis (Section 3.3) also revealed that the grain size varies, measuring 94(5) nm in the first approximately 100-200 nm and reducing to 61(5) nm at deeper levels (around 400-500 nm). This inhomogeneity might suggest the presence of a higher density of recombination centres with respect to the other cases. Moreover, it should be considered the limited light penetration depth in the hematite film. To this respect, considering a reference wavelength of 550 nm, it is about 200 nm for a bulk Fe_2O_3 crystal [2]. In our case, neglecting the fraction of diffused light, the optical abosorption spectra suggest a value around 110 nm. That is, most part of the light is absorbed in a 100 nm thick layer below the surface. The fraction of the layer thickness that is not photoexcited cannot produce photocurrent and, on the contrary, can host dissipative processes for the electronic flow. In addition to this, as seen in the Section 4.1.1, Sn thermal diffusion from FTO to the hematite substrate can increase the photocurrent. This point reserves further investigation. Nevertheless, it is expected that Sn fraction in the photoactivee region is lower for thicker photoanodes. The situation is more delicate concerning the photoanode with 120 nm iron film deposited, where the penetration depth is comparable to its thickness, and the excessively high dark current obscures the contribution of photocurrent. This indicates the presence of intermediate states in the bandgap acting as recombination centres. Also it could be suggested that, in this case as well, Sn plays a role, and the doping region primarily concerns the interface between

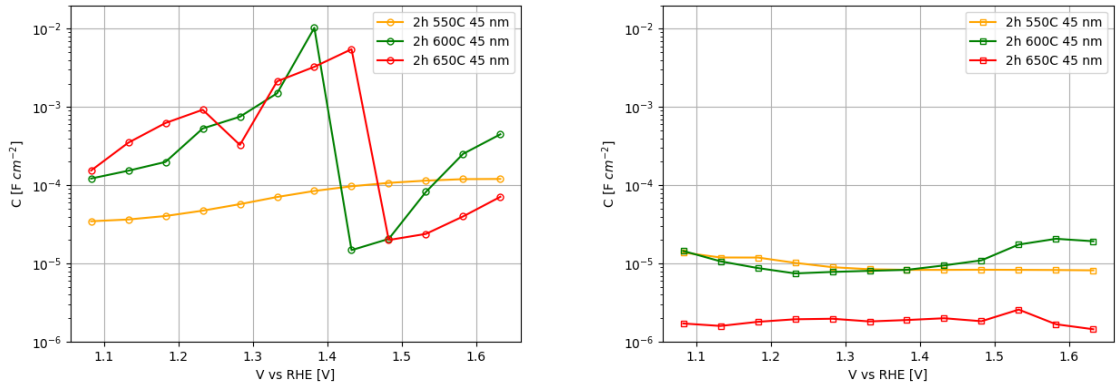

Figure 4.30: C_{trap} (left) and C_{bulk} (right) from analysis of EIS in illuminated condition of 45 nm Fe sample annealed at different T, distinguished by color.

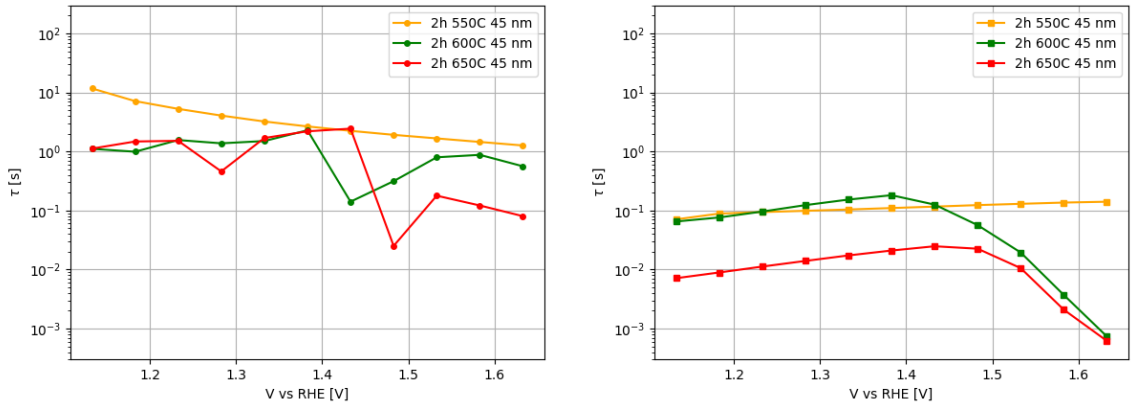

Figure 4.31: τ_{SS} (left) and τ_{bulk} (right) from analysis of EIS in illuminated condition of 45 nm Fe sample annealed at different T, distinguished by color.

hematite and FTO. Partial confirmation of this could be seen in the differences in photocurrent at 1.23 V compared to the 45 nm sample. It is observed that the difference in the photocurrent (45 nm vs 120 nm) is greater at lower temperatures, aligning with the fact that Sn diffuses less at lower temperatures [62]. In addition, in [71] SIMS data for samples produced by CVD with increasing thickness (100, 190, 360 nm) demonstrate a progressive reduction in relative Sn content with the film thickness increasing under identical heat treatment conditions (1h 650°C). In literature the effect of thickness in PEC performance is still debated. For effective photon absorption in PEC applications, it has been recommended in several studies that films exceeding 400 nm in thickness are necessary to enhance light harvesting capabilities [70]. Conversely, considering the short hole diffusion length of α-Fe_2O_3 (2–5 nm) [14], it has been observed that holes generated outside the depletion region undergo recombination, contributing minimally to water oxidation photocurrent. Adjusting both the film thickness and aggregate size to match the magnitude of the depletion layer effectively limits recombination events. This, in turn, enhances the efficient transport of electrons to the external circuit, leading to an overall improvement in performance. Determining the optimal deposition thickness remains an ongoing challenge, yielding contrasting results among different research groups [71]. So, the strategy suggested to significantly improve the photocurrent is to dope the initial iron film with Sn, in the whole film thickness, and to consider a film thickness of the order of the light penetration depth. The results obtained well match literature results. By using this novel approach, consisting in the

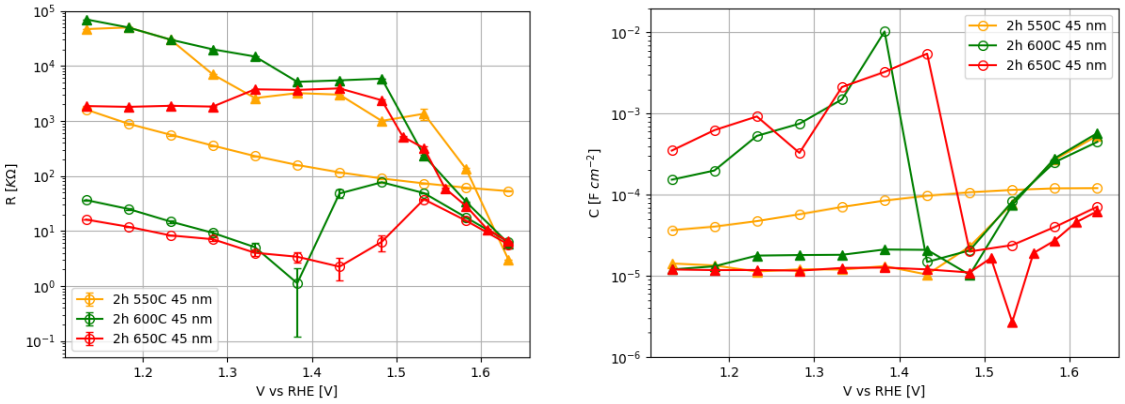

Figure 4.32: $R_{trapping}$ (left) and C_{bulk} (right) from analysis of EIS in dark (blue) and illuminated (red) condition of the sample realized with a 45 nm thick Fe film deposited and annealed in air at a temperature of 650°C.

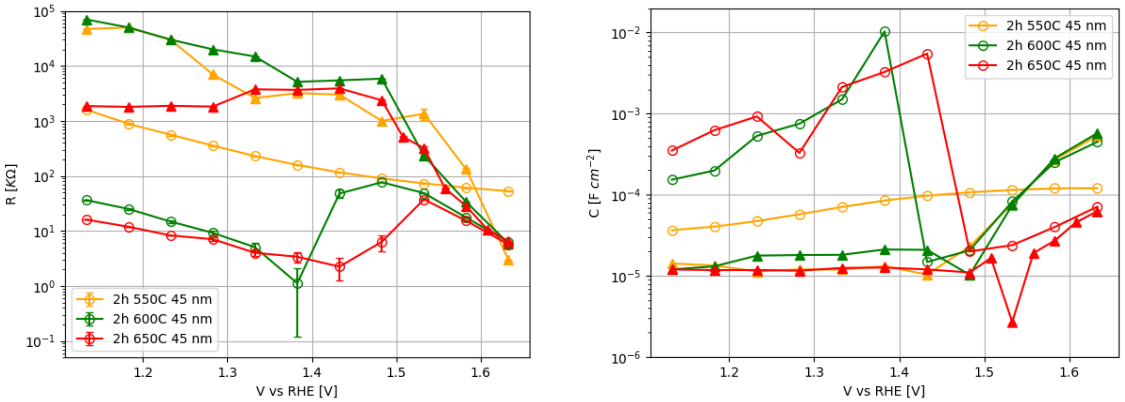

Figure 4.33: $R_{ct,trap}$ (left) and C_{trap} (right) from analysis of EIS in dark (blue) and illuminated (red) condition of the sample realized with a 45 nm thick Fe film deposited and annealed in air at a temperature of 650°C.

deposition of a metallic Fe film instead of a iron oxide one, can offer the advantage of inducing the nanowhiskeres growth during the oxidizing thermal treatment, so allowing an increase of the effective electrode surface in contact with the solution.

4.3.2 Impedance results

Now, impedance measurements conducted on samples annealed at 600°C with increasing thickness are presented. Consider first the EIS results for the photoanode prepared starting from a film thickness of 120 nm. In Fig. 4.40 the impedance spectra (Nyquist plots) are reported, as measured for different polarization potential values in dark conditions. It is noted that up to V = 1.33 V, the curves in the Nyquist plot practically overlap. Zooming in at low impedances (or high frequencies) reveals a well-defined arc at all potentials, and a third contribution between this and the larger arc can be inferred. A first attempt to fit the data with the model proposed in Section 4.2.1 failed, indicating that the two charge transfer paths (direct or mediated by surface states) are not sufficient to properly describe the charge transfer process in the present case. As noted above, this can be clearly seen by comparing the Nyquist measured at V=1.63 V (Fig. 4.40, right) to the same measurement for a thinner film (Fig. 4.11), in particular in the region between the two arcs (corresponding to the frequency range 1-100Hz). It is evident that a third contribution to the impedance is needed. To better analyze

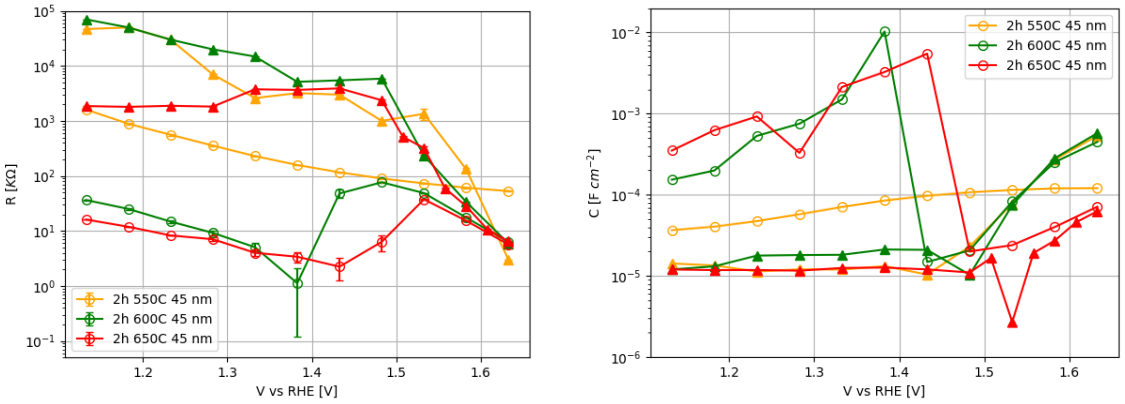

Figure 4.34: τ_{SS} (left) and τ_{bulk} (right) from analysis of EIS in dark (blue) and illuminated (red) condition of the sample realized with a 45 nm thick Fe film deposited and annealed in air at a temperature of 650°C.

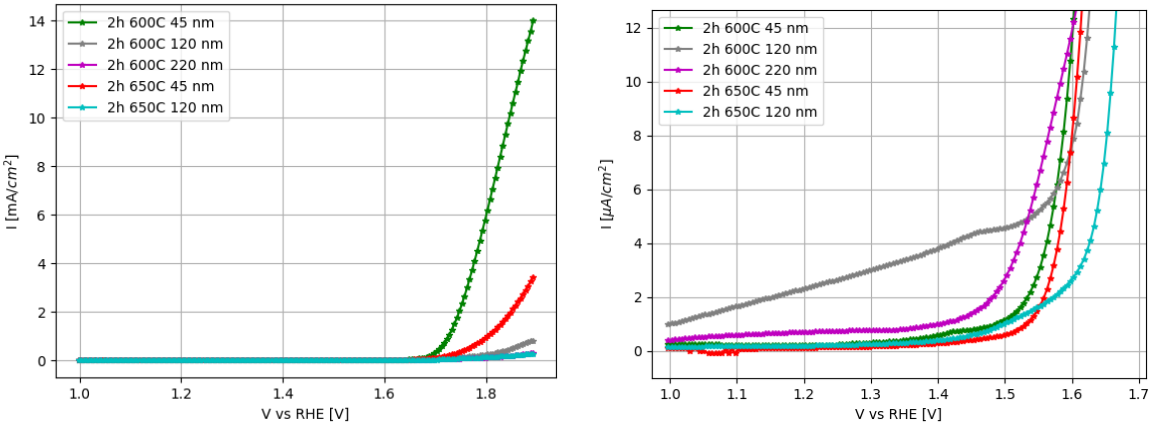

Figure 4.35: IV plots in dark condition of Fe samples on FTO samples with different thickness and annealed in air for 2 hours (at 600°C,650°C), distinguished by color (left). Zoom of the same curves around 1.23 V vs RHE (right).

this point, a possible approach can be found by comparison with the impedance analysis proposed for another photoactive material, i.e., perovskite films fabricated for photovoltaic applications. In that case, an impedance contribution coming from charge transfer processes in the solid state is proposed [61]. As always indicated in [61], a possible modification to the circuit model used so far is the addition of a series resistor R_3 and capacitor C_3 (see Fig. 4.39). The fitting results obtained with this model (Fig. 4.39) are reported in Fig. 4.41 and Fig. 4.42, showing a good agreement with the experimental data. Further verification of the validity of the new introduced model is provided by the more or less substantial agreement of the resistance values obtained from the IV curve and the sum of resistance values obtained from the fit, as visible in Fig. 4.38. This observation is also applicable to the photoanode obtained starting from a 220 nm-thick Fe film. Thus, an impedance scan at three potential values (V = 1.13 V, 1.33 V, and 1.63 V) of the real and imaginary components is provided for all three samples (Fig. 4.41 and Fig. 4.42, the best fitting curves are superimposed to the experimental data.).

From a more quantitative perspective, the fit results indicate that the charge transfer from surface states to the solution is favored with increasing potential (decrease in $R_{ct,trap}$ in Fig. 4.43 left). It is observed that for V¡1.5 V, the $R_{ct,trap}$ of the sample with intermediate thickness is lower than that of the thicker one (indeed, a higher current is observed). Beyond this value, the result is consistent

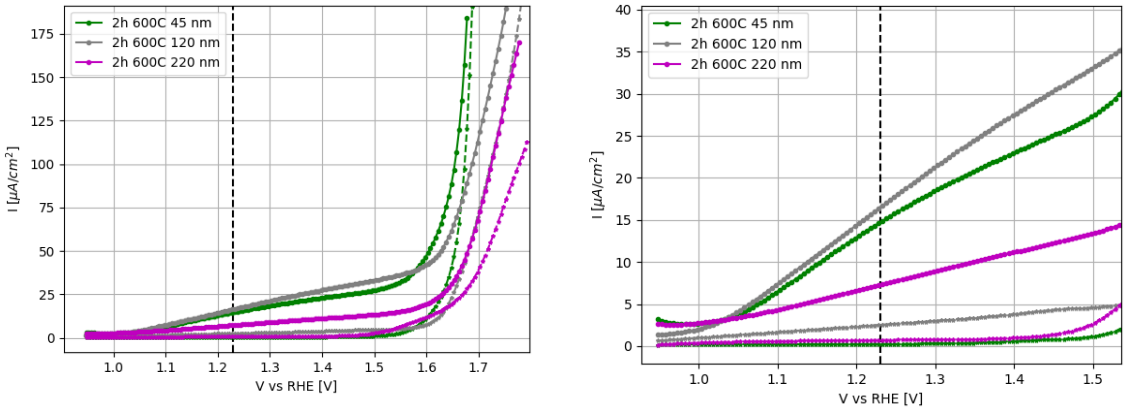

Figure 4.36: IV plots in dark (dashed line) and illuminated condition of Fe samples on FTO samples with different thickness and annealed in air for 2 hours at 600°C (left). Zoom of the same curves around 1.23 V vs RHE (right).

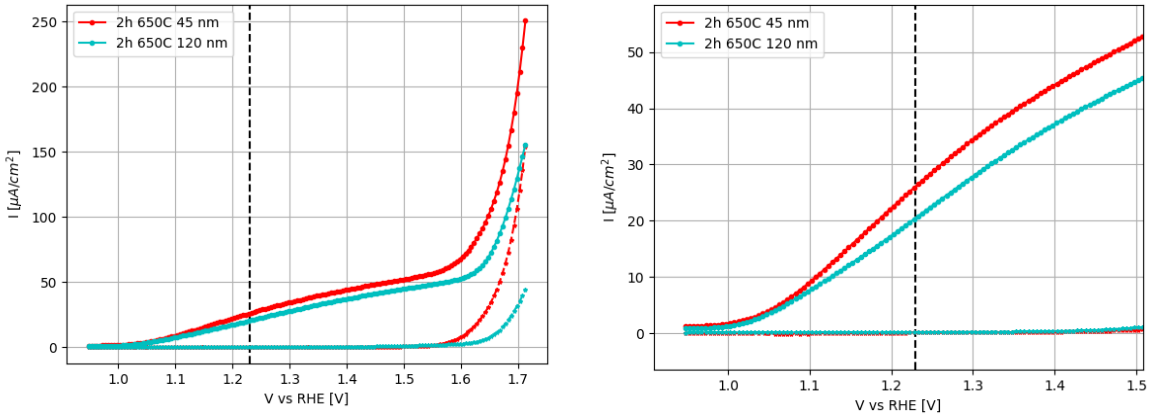

Figure 4.37: IV plots in dark (dashed line) and illuminated condition of Fe samples on FTO samples with different thickness and annealed in air for 2 hours at 650°C (left). Zoom of the same curves around 1.23 V vs RHE (right).

with the trend that thicker samples face greater difficulty in conducting current. Regarding C_{trap}, it is observed in Fig. 4.44 left, that for the sample with Fe film thickness deposited of 45 nm and 120 nm, the values are similar and higher than the thicker photoanode. This strongly correlates with the observed photocurrent results, i.e the values of photocurrent of the specimen with low and intermediate thickness are similar and greater than the thicker one. Concerning $R_{trapping}$ and C_{bulk}, it is noted that the values for thicker samples are lower than those of the thinner one, except for $R_{trapping}$ at $V > 1.5$ V (see Fig. 4.43 and Fig. 4.44 middle). The parameters of the third contribution are very similar between the two samples (for example Fig. 4.44 right). In summary, the specimen with 120 nm and 220 nm iron film deposited thickness have practically similar parameters, with the important exception of C_{trap}. Lastly, charge transfer times in solution are on the order of 5-10 s around V = 1.4 V for all three samples, while a noticeable difference is observed in the times related to bulk processes between the sample with 45 nm Fe film deposited thickness and the other two thicker ones (1 s vs. 0.2 ms for V < 1.5 V). The characteristic time values for the third contribution do not vary substantially until around V = 1.5 V and are on the order of 0.1 s. This relatively high value makes it highly unlikely to attribute the origin of this contribution to the hematite-FTO interface interaction. Further investigations are underway. The trace of a third contribution was also found in the observation of CIMPS spectra of the '45 nm' 650°C sample, which will now be discussed.

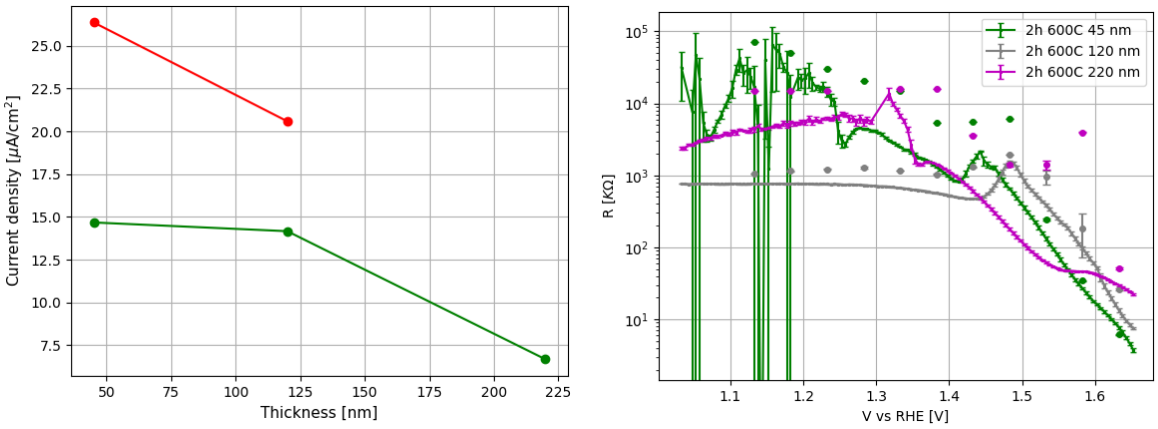

Figure 4.38: Photocurrent values at 1.23 V vs RHE of Fe samples on FTO respect to variation of film deposited thickness (left). Comparison between the resistance value from IV R_{iv} and the sum of the resistance found with EIS analysis $R_{tot} = R_s + R_{trapping} + R_{ct,trap} + R_3$. (right).

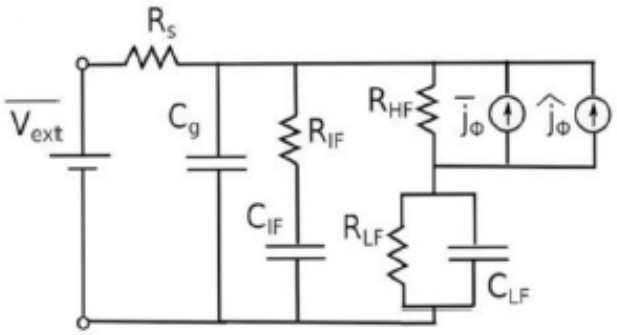

Figure 4.39: Modified equivalent circuit model used to analyze impedance data in dark condition of iron oxide photoanode with 120 nm or 220 nm iron film deposited and thermally treated for 2 hours at 600°C [61]

4.4 CIMPS results

The CIMPS response of the photoanode exhibiting the highest photocurrent, i.e. the 45 nm deposited and annealed in air for 2 hours at 650°C, has been studied. The obtained results, plotted on the Nyquist plot, are shown in Fig. 4.46, ranging from the potential of 1.13 V to 1.73 V in steps of 100 mV. Examining one of these potential curves, for example, at 1.23 V, one can observe the presence of an arc in the positive Q quadrant and another arc in the negative Q quadrant. As discussed in Section 2.7, a spectrum of this shape can be interpreted using the model proposed by Peter et al. [74], thereby deriving the charge transfer rate from surface states k_{ct} and charge recombination rate k_{rec}. The values obtained from this analysis are shown in Fig. 4.47. The trend observed aligns with expectations: as the potential increases, charge separation is facilitated (decreasing k_{rec}), and the injection of photogenerated holes into the solution is promoted (increase in k_{ct}). In more detail,k_{ct} transitions from a value of 0.7 s^{-1} at V=0.98 V to 5.6 s^{-1} at V=1.5 V, while k_{rec} at the same potential values shifts from 3.8 s^{-1} to 0.7 s^{-1}. In particular, there is a sharp increase in the charge transfer rate recorded around the reference potential for water oxidation. This is a promising indication, given that the region of interest centers around this potential. Another parameter derived from the IMPS spectra analysis is the $EQE_{pv,diff}$ (defined in Section 2.7). About the EQE, here it is worth noting that, as expected, it progressively increases by increasing the polarization potential. About the overall efficiency of the system, the low absolute values are mostly related to the spectral mismatch between the exciting light source emission and the hematite absorption spectrum. Unfortunately, at present the feedback process, that is used to modulate the light intensity sinusoidally, only works with the led

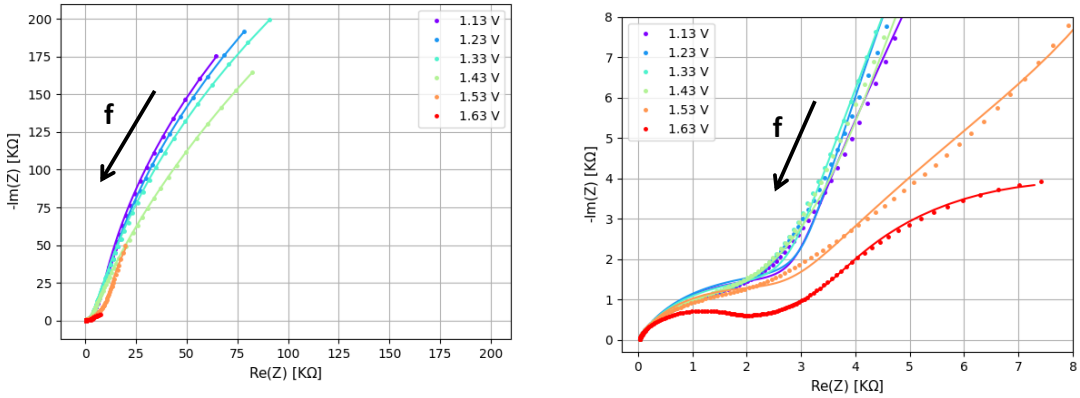

Figure 4.40: Nyquist plot of impedance data measured at different potential in dark condition of Fe sample 120 nm deposited, annealed in air for 2 hours at 600°C

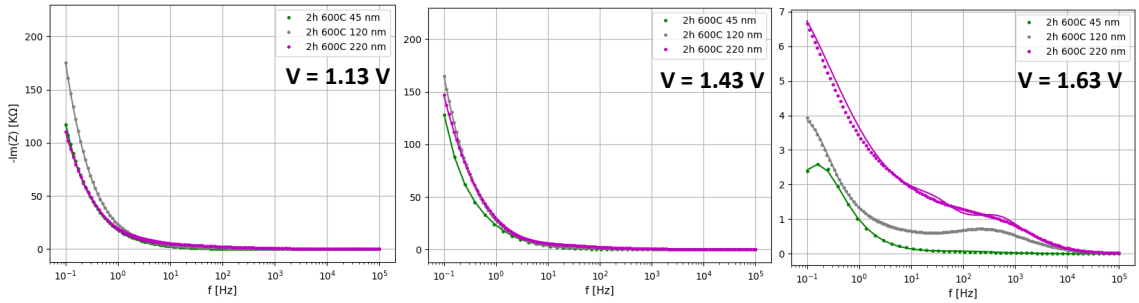

Figure 4.41: Imaginary part of impedance data measured in dark condition of Fe sample annealed in air for 2 hours at 600°C with different film thickness deposited, at 1.13, 1.43 and 1.63 vs RHE. The fit is superimposed to the data and the color legend is the following:: green (45 nm), grey (120 nm), purple (220 nm).

diode that is used in this work. A next step will be to improve the experimental setup allowing to use other light emission sources, properly matching the absorption characteristics of the system to be investigated.

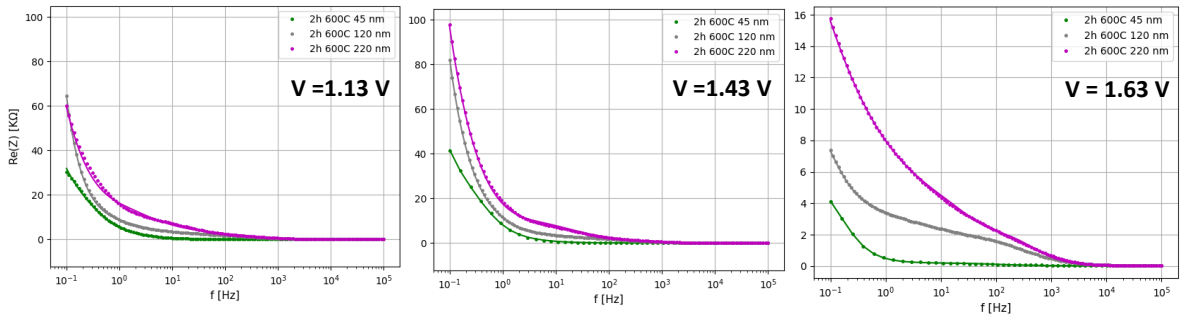

Figure 4.42: Real part of impedance data measured in dark condition of Fe sample annealed in air for 2 hours at 600°C with different film thickness deposited, at 1.13, 1.43 and 1.63 vs RHE. The fit is superimposed to the data and the color legend is the following:: green (45 nm), grey (120 nm), purple (220 nm).

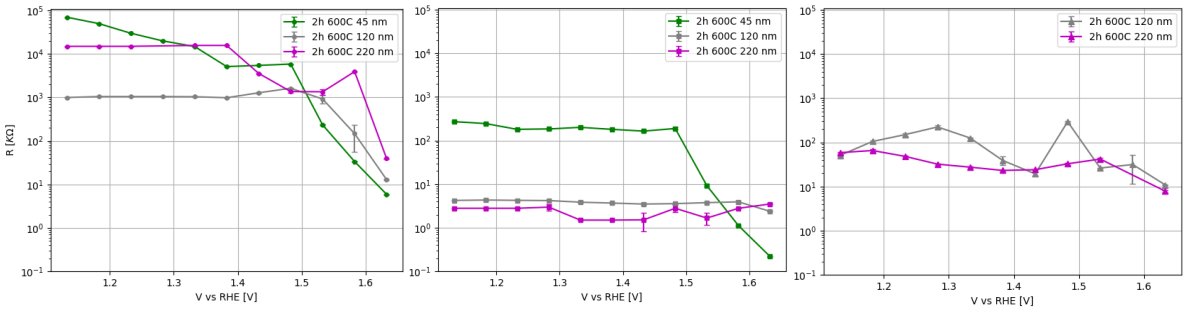

Figure 4.43: In order from left to right: $R_{ct,trap}$,$R_{trapping}$, R_3. The color legend is the following:: green (45 nm), grey (120 nm), purple (220 nm).

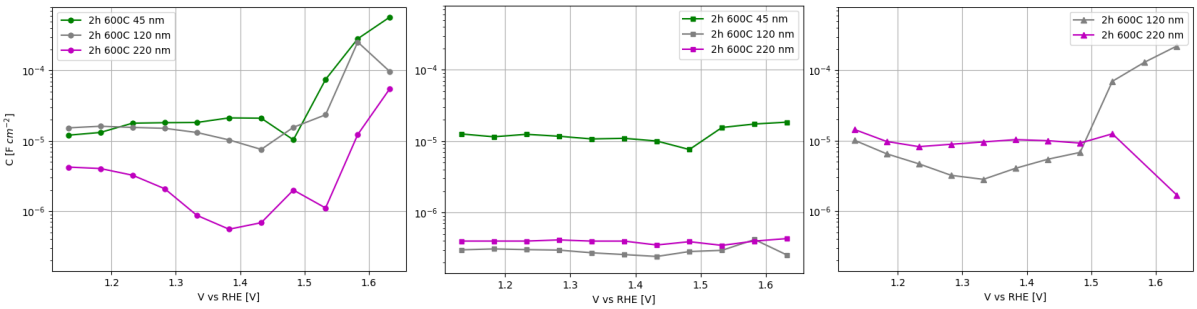

Figure 4.44: In order from left to right: C_{trap}, C_{bulk} and C_3. The color legend is the following:: green (45 nm), grey (120 nm), purple (220 nm).

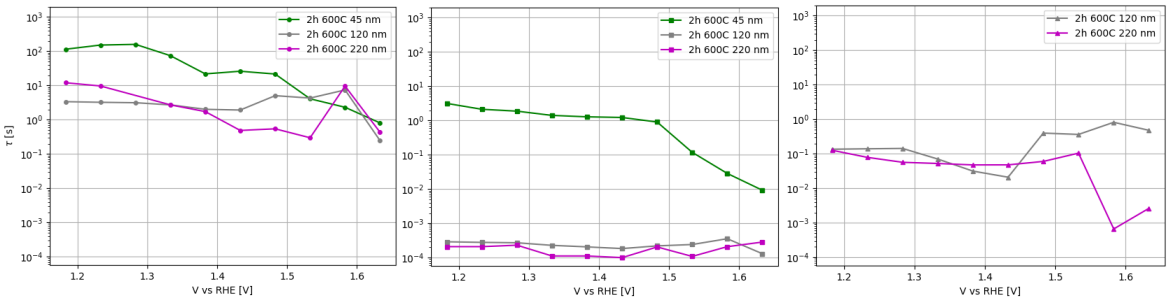

Figure 4.45: In order from left to right: τ_{trap}, τ_{bulk} and τ_3. The color legend is the following:: green (45 nm), grey (120 nm), purple (220 nm).

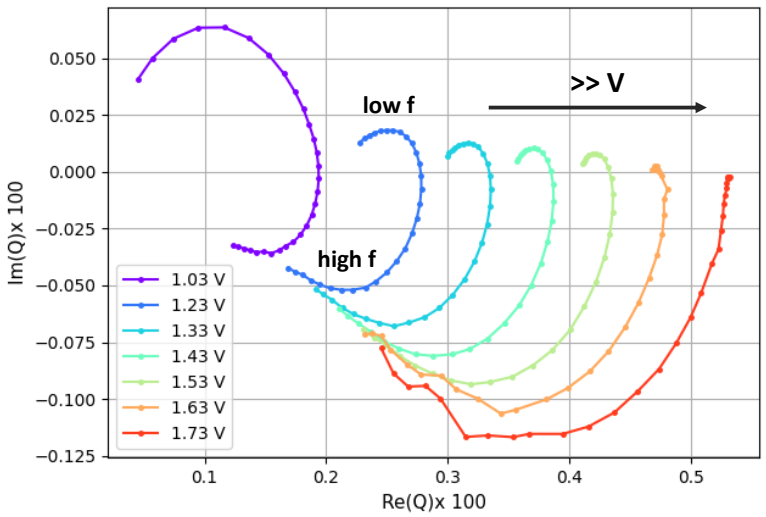

Figure 4.46: CIMPS data dysplayed in Nyquist plot of Fe sample 45 nm eposited annealed for 2 hours at 650 °C. Different color indicates different potential at which the measure has been conducted. Low frequency arc is in the upper quadrant.

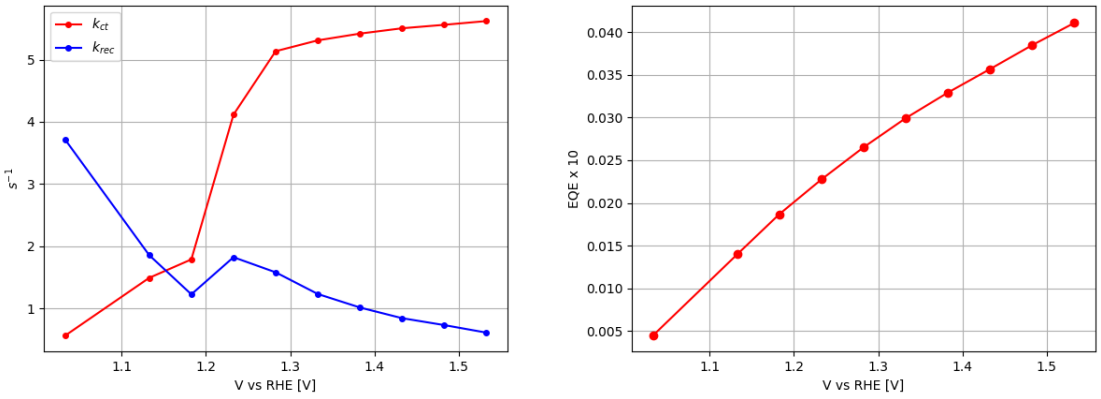

Figure 4.47: Trend respect to the applied voltage of charge transfer (k_{ct}) and recombination (k_{rec}) constant ratesc(left) and of the differential photovoltaic external quantum efficiency $EQE_{PV,diff}$ (right) for 45 nm Fe sample on FTO, annealed for 2 hours in air at 650°C.

Chapter 5

Conclusions

The thesis falls within the research field of developing solar-assisted hydrogen production through a water splitting process. In this field, the development of efficient and sustainable photoanodes is crucial. They should ideally absorb a maximum part of the solar energy and use it to produce, with the highest efficiency, photogenerated charges whose energy is suitable to promote water oxidation. In this framework, the study presented in this thesis is an experimental investigation of photoanodes based on sustainable iron-oxide nanostructured layers, prepared by Physical Vapour Deposition of a metallic film on a transparent conductive substrate, followed by suitable thermal annealing treatments in an oxidizing atmosphere. In particular, the objective of the thesis was to understand the physical parameters that promote the production and efficient transfer of photo-generated charges in solution and to provide a model describing the physics at the interface between the photoanode and the electrolyte solution in which it is immersed.

Focus has been placed on two primary synthesis factors: the annealing temperature and the thickness of the deposited Fe film. Various characterization techniques were employed to conduct the study. Surface sample morphology was studied using Atomic Force Microscopy (AFM) and Scanning Electron Microscopy (SEM), while the composition and crystalline structure were investigated through Raman spectroscopy and Grazing Incidence X-Ray Diffraction (GIXRD). The analysis of optical properties was conducted through absorbance measurements, and finally, the study regarding the ability for water splitting was carried out via photoelectrochemical (PEC) measurements, including current-to-voltage, impedance under dark and illuminated conditions (EIS), and Controlled Intensity Modulated Photocurrent Spectroscopy (CIMPS) technique.

The results on photoanodes obtained by varying the temperature of the annealing process indicate that higher annealing temperatures favour the growth of larger crystal grains of the hematite (Fe_2O_3) phase, that is the most stable oxidized phase useful to promote water oxidation. Raman analysis does not detect any residual Fe_3O_4 nanophase after annealing at T¿500C. Moreover, if the thickness of the initial metallic film is larger that about 100 nm, a dense layer of iron oxide nanowhiskers grows on the film surface. When the hematite nanostructured layers are used as photoanodes in a photoelectrochemical cell to promote water splitting, the photocurrent recorded upon illumination with a white LED strongly depends on the annealing temperature used to prepared the photoanode. Higher photocurrent values are obtained if higher annealing temperatures are used. One first reason for this is the increased film absorbance and crystallinity promoted by a higher annealing temperature. Nevertheless, as suggested by the scientific literature, the thermal diffusion of tin from the conductive substrate into the hematite film can play an important role. To better understand the potential impact of Sn doping on the nanostructured iron oxide film, two photoanodes were prepared by codepositing Sn and Fe in metallic form (thickness of 60 nm), followed by oxidizing annealing. It was observed that for the same annealing temperature (T=550°C, i.e. below the threshold for Sn diffusion from the substrate), increasing the percentage of Sn present resulted in an increase in photocurrent, in agreement with the previous results.

The experimental results on photoanodes obtained by increasing the initial Fe film thickness (from 45 to 220 nm) show that the thicker the material, the lower the recorded photocurrent. This result, which contradicts the observed increase in absorbance values and, consequently, a greater light harvesting capability, can be explained by considering that, for thick layers, the region where photons are absorbed and the region doped with Sn by thermal dffusion have a limited overlap.

An outcome of the increase in thickness is the possibility of nanostructure formation. In this study, a qualitative observation from SEM images revealed that with deposited film thickness below 120 nm, the morphology consists essentially of small hematite grains, and the crystallite size increases as the film thickness increases. Morphologically, it was also observed that long and low-temperature annealing in air promotes a more dense nanowhisker structure than short high-temperature thermal treatment, in agreement with the proposed process for the nanowhisker formation, that requires the formation of a cations vacancy gradient along the film thickness direction, favored by a lower annealing temperature.

The maximum photocurrent recorded at the reference potential for water oxidation pertains to the photoanode obtained by proper annealing of a 45-nm thick Fe film, amounting to about 1 mA/(cm2W). Considering that the emission spectrum of the LED used only partially overlaps with the hematite absorption spectrum, the results obtained are likely well comparable to literature values. A rigorous comparison will be done in the next future, since a solar simulator will be soon available at the DFA.

The second objective of the thesis was the modeling of the physical processes governing the response of the photoanode immersed in the electrolyte solution through impedance measurements (EIS) in the dark and under illumination, as well as the CIMPS technique. The equivalent circuit used to fit the impedance response of the samples under study simulates two charge transfer processes with their respective characteristic times: one involves the trapping/detrapping of charges from the bulk to surface states with the characteristic time τ_{bulk}, and the other involves charge transfer from these states to the solution with the characteristic time τ_{trap}.

It was observed that the model is sufficiently efficient in describing the impedance data and resolving two contributions. A higher photocurrent response is correlated with the presence in the impedance data fit results under illumination conditions of a peak in the chemical capacity C_{trap} describing the occupation of surface states in the range 1.3 V-1.5 V vs RHE, and a decrease in the charge transfer resistance from these states to the solution $R_{ct,trap}$ in the same range. Additionally, it is observed that the peak of C_{trap} is visible under illumination conditions. These trends show that the photoexcitation of hematite is indeed necessary to allow charge carriers to significantly fill the trap states, and that the potential range in which the phenomenon occurs is related to the principal energy level of these states. A partial confirmation of the model's validity was also found in the dark EIS analysis for thicker photoanodes. However, the circuit model used is not entirely sufficient to describe all underlying processes, as suggested by the dark EIS analyses for samples with a greater thickness of deposited film and the CIMPS analysis of the sample showing the best photocurrent performance. Further investigations are needed. Also, from the CIMPS analysis it is observed that with the increase in applied voltage, there is a predictable decrease in the recombination rate and an increase in the constant rate of charge transfer. In particular, an abrupt increase of the charge transfer rate is recorded for polarization potential around the reference value for water oxidation. This is a promising indication since the region of interest is around this potential.

From future perspectives, the use of a solar simulator will allow for a study under illumination conditions closer to those expected for field use. Additionally, a more quantitative comparison with literature data will be possible. The impedance analyses (in the dark, under light, and modulated by photocurrent) have yielded encouraging results. It will be necessary to delve deeper into the work with the aim of producing a unified model capable of describing all experimental results. To achieve this, it will certainly be helpful to fabricate photoanodes with homogeneous composition, in line with the presented results, properly tuning the Sn doping by deposition. Moreover, the use of a metallic tin-doped iron film as starting material for the photoanode production, which is an original approach firstly used in this thesis, will allow for the full exploitation of the iron oxide nanowhiskers that form

during the oxidizing process in a controlled atmosphere, largely increasing the solid-liquid interface for an efficient solar-assisted hydrogen generation.

Bibliography

[1] https://www.iea.org/reports/world-energy-balances-overview/world

[2] B. Iandolo, B. Wickman, I. Zorić and A. Hellman. The rise of hematite: origin and strategies to reduce the high onset potential for the oxygen evolution reaction. *J. Mater. Chem. A*,2015, 3(33), 16896-16912. doi:10.1039/c5ta03362d.

[3] R. van de Krol and M. Gratzel, *Photoelectrochemical hydrogen production*, Springer US, 2012,1-2-4. doi 10.1007/978-1-4614-1380-6.

[4] L. A. Marusak, R. Messier and W. B. White, Optical absorption spectrum of hematite, αFe2O3 near IR to UV, *J. Phys. Chem. Solids*, 1980, 41(9), 981–984. doi:10.1016/0022-3697(80)90105-5.

[5] A. B. Murphy, P. R. F. Barnes, L. K. Randeniya, I. C. Plumb, I. E. Grey, M. D. Horne and J. A. Glasscock, Efficiency of solar water splitting using semiconductor electrodes, *Int. J. Hydrogen Energy*, 2006, 31(14), 1999–2017. doi:10.1016/j.ijhydene.2006.01.014.

[6] L.S. Ray Yeh and N. Hackerman, Iron Oxide Semiconductor Electrodes in Photoassisted Electrolysis of Water, *J. Electrochem. Soc.*, 1977, 124 (6), 833. doi:10.1149/1.2133421.

[7] N. S. Lewis and D.G. Nocera, Powering the planet: chemical challenges in solar energy utilization, *Proc. Natl. Acad. Sci. U.S.A.*, 2006, 103 (43), 15729–35. doi: 10.1073/pnas.0603395103.

[8] M. J. Katz, S. C. Riha, N. C. Jeong, A. B. F. Martinson, O. K. Farha and J. T. Hupp, Toward solar fuels: Water splitting with sunlight and "rust", *Coord. Chem. Rev.*, 2012, 256 (21-22), 2521–2529. doi:10.1016/j.ccr.2012.06.017.

[9] C. Sanchez and K.D. Sieber and G.A. Somorjai, The photoelectrochemistry of niobium doped α-Fe2O3, *J. Electroanal. Chem. Interf. Electrochem.*, 1988, 252(2), 269–290. doi: 10.1016/0022-0728(88)80216-X.

[10] I. Balberg and H. L. Pinch, The optical absorption of iron oxides, *J. Magn. Magn. Mater.*, 1978, 7(1), 12–15. doi:10.1016/0304-8853(78)90138-5.

[11] P. Liao, M. C. Toroker and E. A. Carter, Electron transport in pure and doped hematite, *Nano Lett.*, 2011, 11(4), 1775–81. doi: 10.1021/nl200356n.

[12] N. J. Cherepy, D. B. Liston, J. A. Lovejoy, H. Deng and J. Z. Zhang, Ultrafast Studies of Photoexcited Electron Dynamics in γ- and α-Fe2O3 Semiconductor Nanoparticles, *J. Phys. Chem. B*, 1998, 102(5), 770–776. doi:10.1021/jp973149e.

[13] A.G. Joly, J. R. Williams, S.A. Chambers, G. Xiong, W.P. Hess and D.M. Laman,Carrier dynamics in α-Fe2O3 (0001) thin films and single crystals probed by femtosecond transient absorption and reflectivity, *J. Appl. Phys.*, 2006, 99(5), 053521. doi:10.1063/1.2177426.

[14] F. le Formal, N. Tétreault, M. Cornuz, T. Moehl, M. Grätzel and K. Sivula, Passivating surface states on water splitting hematite photoanodes with alumina overlayers, *Chem. Sci.*, 2011, 2(4), 737-743. doi:10.1039/C0SC00578A.

[15] B. Klahr, S. Gimenez, F. Fabregat Santiago,T. Hamann, J. Bisquert, Water Oxidation at Hematite Photoelectrodes: The Role of Surface States, *J. Am. Chem. Soc.*, 2012, 134(9), 4294 4302. doi:10.1021/ja210755h.

[16] Klahr, B.; Gimenez, S.; Fabregat Santiago, F.; Bisquert, J.; Hamann, T. W. Photoelectrochemical and Impedance Spectroscopic Investigation of Water Oxidation with "Co–Pi"-Coated Hematite Electrodes. *J. Am. Chem. Soc.*, 2012, 134(40), 16693-16700. doi: 10.1021/ja306427f.

[17] R. Edla, N. Patel, M. Orlandi, N. Bazzanella, V. Bello, C. Maurizio, G. Mattei, P. Mazzoldi, A. Miotello, Highly photo-catalytically active hierarchical 3D porous/urchin nanostructured Co_3O_4 coating synthesized by Pulsed Laser Deposition, *Appl. Catal. B: Env.*, 2015, 166-167, 475-484. doi: 10.1016/j.apcatb.2014.11.060.

[18] M. E. A Warwick, K. Kaunisto, D. Barreca, G. Carraro, A. Gasparotto, C. Maccato, E. Bontempi, C. Sada, T. Ruoko, S. Turner and G. Van Tendeloo, Vapor Phase Processing of α-Fe2O3 Photoelectrodes for Water Splitting: An Insight into the Structure/Property Interplay, *ACS Appl. Mater. Interfaces*, 2015, 7(16), 8667-8676. doi:10.1021/acsami.5b00919.

[19] C. Hu, L. Zhangb and J.Gong, Recent progress made in the mechanism comprehension and design of electrocatalysts for alkaline water splitting, *Energy Environ. Sci.*, 2019, 12(9), 2620 2645. doi:10.1039/C9EE01202H.

[20] P. Ragonese, *Cobalt oxide nanostructures on Silicon for photoelectrocatalysis*, Tesi di Laurea Magistrale, 2020, 2, 6.

[21] B. Bhattacharyya, *Electrochemical Micromachining for Nanofabrication, MEMS and Nanotechnology*, Elsevier Inc., 2015, 1. doi:10.1016/C2014-0-00027-5.

[22] L. Vayssieres, Growth of Arrayed Nanorods and Nanowires of ZnO from Aqueous Solutions, *Advanced Materials*, 2003, 15, 464-69, doi:10.1002/adma.200390108.

[23] S. Swann, Magnetron sputtering, *Phys. in Tech.*, 1988, 19(2), 67–75. doi:10.1088/0305-4624/19/2/304.

[24] M. Braun, *Magnetron sputtering technique. Handbook of Manufacturing Engineering Technology*, Springer: Berlin, Germany, 2015, 2929–2957.

[25] https://www.dentonvacuum.com/products/discovery/

[26] D. M. Mattox, *Handbook of Physical Vapor Deposition (PVD) Processing*, Elsevier, 2010. doi.org/10.1016/C2009-0-18800-1.

[27] https://www.adnano-tek.com/magnetron-sputtering- deposition-msd.html

[28] I. Stabrawa, A. Kubala-Kukuś, D. Banaś, G. Pepponi, J. Braziewicz, M. Pajek and M. Teodorczyk, Characterization of the morphology of titanium and titanium (IV) oxide nanolayers deposited on different substrates by application of grazing incidence X-ray diffraction and X-ray reflectometry techniques, *Thin Solid Films*, 2019, 671, 103-110. doi:10.1016/j.tsf.2018.12.034.

[29] Zeiss. Zeiss sigma field emission scanning electron microscope. URL: www.zeiss.com/microscopy/int/products/scanning-electron- microscopes/sigma.html

[30] J. Goldstein, *Scanning Electron Microscopy and X-ray microanalysis*, Springer, 2018. doi: 10.1007/978-1-4939-6676-9.

[31] G. Binnig, C. F. Quate, and C. Gerber. Atomic force microscope, *Phys. Rev. Lett.*, 1986, 56(9), 930–933. doi: 10.1103/PhysRevLett.56.930.

[32] Feng-I Tai, *Surface characterization and manipulation of polyampholytic hydrogel coatings*, Linkopings Universitet, 2019. doi:10.3384/diss.diva-156496.

[33] M. Linford, Introduction to Surface and Material Analysis and to Various Analytical Techniques, *Vacuum Technology and Coating*, 2014, 27-33.

[34] https://www.parksystems.com/index.php/park-spm-modes/91-standard-imaging-mode/223-basic-contact-afm-dynamic-force-microscope-dfm

[35] P. Eaton and P. West. *Atomic force microscopy*, Oxford university press, 2010. doi:10.1093/acprof:oso/9780199570454.001.0001.

[36] C.F. Quate. The AFM as a tool for surface imaging, *Surface Science*,1994, 299-300, 980–995. doi:10.1016/0039-6028(94)90711-0.

[37] https://wasatchphotonics.com/technologies/

[38] https://www.gamry.com/application-notes/instrumentation/understanding-specs-of-potentiostat

[39] S. Wang et al., Nature Reviews, Methods Primers , 2021, 1-41 J. Zhang, O. Gharbi, V. Vivier, M. Gao, M. E. Orazem, Electrochemical impedance spectroscopy, *Nat Rev Methods Primers*, 2021, 1(1), 41. doi: 10.1038/s43586-021-00039-w.

[40] A. C. Lazanas, M. I. Prodromidis, Electrochemical Impedance Spectroscopy A Tutorial, *ACS Meas. Sci.*, 2023, 3(3), 162-193. doi: 10.1021/acsmeasuresciau.2c00070.

[41] K. Sivula, R. Zboril, F. Le Formal, R. Rosa, A. Weidenkaff, J. Tucek, J. Frydrych, M. Grätzel, Photoelectrochemical water splitting with mesoporous hematite prepared by a solution-based colloidal approach, *J. Am. Chem. Soc.*, 2010, 132(21), 7436-44. doi:10.1021/ja101564f.

[42] T. Dlugosch, A. Chnani, P. Muralidhar, A. Schirmer, J. Biskupek and S. Strehle, Thermal oxidation synthesis of crystalline iron-oxide nanowires on low-cost steel substrates for solar water splitting, *Semicond. Sci. Technol.*, 2017, 32(8), 084001. doi: 10.1088/1361-6641/aa7593.

[43] B. Kalinic, L. Girardi, P. Ragonese, A. Faramawy, G. Mattei, M. Frasconi, R. Baretta, S. Bogialli, M. Roverso, G.A. Rizzi and C. Maurizio, Diffusion-driven formation of Co3O4 nanopetals layers for photoelectrochemical degradation of organophosphate pesticides, *Appl. Surf. Sc.*, 2022, 596, 153552. doi:10.1016/j.apsusc.2022.153552

[44] A. Kay, I. Cesar, M. Grätzel, New Benchmark for Water Photooxidation by Nanostructured α-Fe2O3 Films, *J. Am. Chem. Soc.*, 2006, 128(49), 15714-21. doi: 10.1021/ja064380l.

[45] R. van de Krol, Y. Liang and J. Schoonman, Solar hydrogen production with nanostructured metal oxides, *J. Mater. Chem.*, 2008, 18, 2311–20. doi: 10.1039/b718969a

[46] S. T. Jäger and S. Strehle, Design parameters for enhanced photon absorption in vertically aligned silicon nanowire arrays, *Nanoscale Res. Lett.*, 2014, 9, 511. doi: 10.1186/1556-276X-9-511.

[47] E. N. Maslen, A. Streltsov, N.R. Streltsova, N. Ishizawa, Synchrotron X-ray study of the electron density in α-Fe_2O_3, *Acta Crystall. B*, 1994, 50, 435-441.

[48] W.H. Baur and A.A. Khan, Rutile-Type Compounds VI SiO_2, GeO_2 and a comparison with other Rutile-Type Structures, *Acta Crystall. B*, 1971, 27, 2133-39. doi:10.1107/S0567740871005466.

[49] https://gixa.ati.tuwien.ac.at/tools/penetrationdepth.xhtml

[50] Y. Ling, G. Wang, D. A. Wheeler, J. Z. Zhang, and Y. Li, Sn-Doped Hematite Nanostructures for Photoelectrochemical Water Splitting, *Nano Lett.*, 2011, 11, 2119-25. doi: 10.1021/nl200708y.

[51] S. Piccinini, The band structure and optical absorption of hematite (αFe_2O_3): a first principles GW-BSE study, *Phys. Chem. Chem. Phys.*, 2019, 21, 2957. doi: 10.1039/c8cp07132b.

[52] J. Tauc, Optical properties and electronic structure of amorphous Ge and Si, *Mat. Res. Bull.*, 1967, 46, 3-37.

[53] I.K. Pannan, N. Nolwazi and D. Mmantsae, Influence of coating techniques on the optical and structural properties of hematite thin films, *Surfaces and Interfaces*, 2019, 17, 100384. doi: 10.1016/j.surfin.2019.100384.

[54] D.L.A. de Faria,S. Venaüncio Silva and M.T. de Oliveira, Raman Microspectroscopy of Some Iron Oxides and Oxyhydroxides, *Journal of Raman Spectroscopy*,1997, 28, 873-878.doi:10.1002/(SICI)1097-4555(199711)28:11¡873::AID-RS177¿3.3.CO;2-2

[55] D.L.A. de Faria, F.N. Lopes, Heated goethite and natural hematite: Can Raman spectroscopy be used to differentiate them, *Vibrational Spectroscopy*, 2007, 45(2), 117-121, doi.org/10.1016/j.vibspec.2007.07.003.

[56] J. Li, H. Chen, C. A. Triana, G. R. Patzke, Hematite Photoanodes for Water Oxidation:Electronic Transitions, Carrier Dynamics,and Surface Energetics, *Angew. Chem. Int. Ed.*, 2021, 60(34), 18349-18887. doi: 10.1002/anie.202101783.

[57] M. Fukawa, K. Sato, T. Tsukamoto, K. Adachi, H. Nishimura, Development of tempered-glass substrates with TCO films for a-Si solar cells, *Solar Energy Materials and Solar Cells*, 1997, 49(1-4), 107-112. doi:10.1016/S0927-0248(97)00183-9.

[58] TO FIX J. Phys. Chem. Solids 41 (1980) 981

[59] M. Rioult, D. Stanescu, E. Fonda, A. Barbier and H. Magnan, Oxygen Vacancies Engineering of Iron Oxides Films for Solar Water Splitting, *J. Phys. Chem. C*, 2016, 120(14), 7482-90. doi:10.1021/acs.jpcc.6b00552.

[60] C. Hsu, X. Geng, W. Wu, M. Zhao, X. Zhang, P. Huang, and S. Lien, Air Annealing Effect on Oxygen Vacancy Defects in Al-doped ZnO Films Grown by High-Speed Atmospheric Atomic Layer Deposition, *Molecules*, 2020, 25(21), 5043. doi:10.3390/molecules25215043.

[61] S. Ravishankar, A. Riquelme, S. K. Sarkar, M. Garcia-Batlle, G. Garcia-Belmonte and J. Bisquert, Intensity-Modulated Photocurrent Spectroscopy and Its Application to Perovskite Solar Cells, *J. Phys. Chem. C*, 2019, 123 (41). doi:10.1021/acs.jpcc.9b07434.

[62] C. Bohn, A. Agrawal, E. Walter, M. Vaudin, A. Herzing, P. Haney, A. Talin, V. Szalai, Effect of Tin Doping on α-Fe_2O_3 Photoanodes for Water Splitting, *J. Phys. Chem. C*, 2012, 116(29), 15290-96. doi: 10.1021/jp305221v.

[63] J. Krýsa, A. Němečková, M. Zlámal, T. Kotrla, M. Baudys, Š. Kment, Z. Hubička and M. Neumann-Spallart, α-Fe2O3/TiO2 stratified photoanodes, *J. Photoch. and Photob. A Chem.*, 2018, 366, 12-17. doi: 10.1016/j.jphotochem.2018.03.015.

[64] R. Sinha, R. Lavrijsen, M. Verheijen, E. Zoethout, H. Genuit, M. C. van de Sanden, A. Bieberle-Hütter, Electrochemistry of Sputtered Hematite Photoanodes: A Comparison of Metallic DC versus Reactive RF Sputtering, *ACS Omega*, 2019, 4(5), 9262-9270. doi: 10.1021/acsomega.8b03349.

[65] E. Barsoukov, *Impedance spectroscopy: Theory, experiment and applications*, Wiley-Interscience Ed., 2005.

[66] Equivalent circuit of electrons and holes in thin semiconductor films for photoelectrochemical water splitting applications, L. Bertoluzzi and J. Bisquert, *J. Phys. Chem. Lett.*, 2012, 3, 2517-22. doi: 10.1021/jz3010909.

[67] M. D. Murbach, B. Gerwe, N. Dawson-Elli and L. Tsui, A Python package for electrochemical impedance analysis, *Journal of Open Source Software*, 2020, 5(52), 2349. doi: 10.21105/joss.02349.

[68] G. Brug, A.L.G. van den Eeden, M. Sluyters-Rehbach and J.H. Sluyters, The analysis of electrode impedance complicated by the presence of a constant phase element, *J. Electroanal. Chem. Interfacial Electrochem.*, 1984, 176(1), 275-295. doi: 10.1016/S0022-0728(84)80324-1.

[69] R. Morrish, M. Rahman, J.M. Don MacElroy and C.A. Wolden, Activation of Hematite Nanorod Arrays for Photoelectrochemical Water Splitting, *Chem. Sus. Chem.*, 2011, 4(4), 474-479. doi: 10.1002/cssc.201100066.

[70] K. Sivula, F. Le Formal, and M. Grätzel, Solar water splitting: progress using hematite α-Fe_2O_3 photoelectrodes. *Chem.Sus.Chem.*, 2011, 4(4), 432–449. doi: 10.1002/cssc.201000416.

[71] M. Warwick, G. Carraro, A. Gasparotto, C. Maccato, D. Barreca, C. Sada, E. Bontempi, Y. Gönüllü and S. Mathur, Interplay of thickness and photoelectrochemical properties in nanostructured α-Fe_2O_3 thin films, *physica status solidi (a)*, 2015, 212(7), 1501-1507. doi: 10.1002/pssa.201532366.

[72] M. Rioult, H. Magnan, D. Stanescu, and A. Barbier, Single Crystalline Hematite Films for Solar Water Splitting: Ti-Doping and Thickness Effects, *J. Phys. Chem. C*, 2014, 118, 3007. doi: 10.1021/jp500290j.

[73] F. Le Formal, M. Greatzel, and K. Sivula, *Adv. Funct. Mater.*, 2010, 20, 1099.

[74] E. Ponomarev, L. Peter, A Generalized Theory of Intensity Modulated Photocurrent Spectroscopy (IMPS), *J. Electroanal. Chem.*, 1995, 396, 219.